DESIGN OF A TORPEDO: STUDY OF DRAG REDUCTION USING COMPUTATIONAL FLUID DYNAMICS

by

Selim Sancı

B.S., in M.E., Boğaziçi University, 2003

Submitted to the Institute for Graduate Studies in
Science and Engineering in partial fulfillment of
the requirements for the degree of
Master of Science

Graduate Program in Mechanical Engineering
Boğaziçi University
2006

ACKNOWLEDGEMENTS

I would like to express my gratitude to Prof. Haluk Örs for accepting to supervise my thesis and his helpful guidance. His support throughout the development of this thesis is gratefully acknowledged.

I would like to express my thanks to my friends in Mechanical Engineering Department, especially to Hatice Mercan, Yalın Kaptan and Gökhan Tekeli.

I finally would like to thank to my family for their continuous support and encouragement.

ABSTRACT

DESIGN OF A TORPEDO: STUDY OF DRAG REDUCTION USING COMPUTATIONAL FLUID DYNAMICS

Drag is a big problem for objects moving at high speeds. The reduction of drag should be the primary consideration of the engineers since it provides high speeds with limited engine power. Drag reduction also provides energy saving which makes it an ever-lasting engineering study.

Reduction of drag is achieved using different methods. Body shaping is the most conventional method which is still used today. The aim of the study was to find the optimum geometry for an acoustic torpedo. In order to achieve this, different geometries that are based on a real model were generated and optimum geometry was determined using computational fluid dynamics (CFD) tools.

The examination of the optimum geometry also showed that frictional forces have an important role in total drag force and elimination of friction drag can yield higher speeds. This study may be a good source material for those who want to study technologies of friction drag reduction on torpedoes.

ÖZET

TORPİL TASARIMI VE DİRENÇ KUVVETİNİN HESAPLAMALI AKIŞKANLAR DİNAMİĞİ KULLANILARAK İNCELENMESİ

Direnç, yüksek hızlarda seyreden vasıtalar için büyük bir sorundur. Direnç kuvvetini yok etmek veya azaltmak motor gücünü sınırlı tutarak daha yüksek hızlara ulaşmaya olanak tanıdığından mühendislerin başlıca uğraşlarından biri olmalıdır. Direnç kuvvetini azaltmak aynı zamanda enerji tasarrufu sağladıgından sürtünme kuvvetinin azaltılması devamlılığını hiçbir zaman kaybetmeyecek mühendislik konularından biridir.

Direnç kuvvetini azaltmanın belli başlı yöntemleri vardır. Bunların en bilineni cismin geometrisiyle oynamak ve en uygun geometriyi bulmaktır. Bu çalışmada akustik bir torpil için en uygun geometri bulunmuştur. Bu amaca ulaşmak için varolan bir torpil modeli örnek alınarak farklı geometriler türetilmiş ve içlerinden en uygun olanı Hesaplamalı Akışkanlar Dinamiği'nden faydalanılarak tesbit edilmiştir.

Bulunan geometrinin üstünde yapılan incelemeler, sürtünme kuvvetlerinin torpil üzerinde büyük etkisinin olduğunu göstermektedir. Bu kuvvetlerin azaltılması ise torpilin hızını büyük ölçüde artıracaktır.

TABLE OF CONTENTS

LIST OF FIGURES

LIST OF TABLES

LIST OF SYMBOLS/ABBREVIATIONS

A	Area
C	Length of the chord
C_D	Drag coefficient
C_{Df}	Friction drag coefficient
C_{Dp}	Pressure drag coefficient
C_f	Local friction coefficient or surface (skin) friction coefficient
C_L	Lift coefficient
C_p	Pressure coefficient
c	Concentration
D_p	Pressure drag force
E	Energy
F	Force
f	Fanning friction factor
G_b	Generation of turbulence
g_i	Gravitational vector in ith direction
I	Turbulence intensity
J_f	Mass flux through face f
J'_f	Flux correction
k	Turbulence kinetic energy
L	Length of the body
M	Molecular weight
P	Pressure
Pr_t	Prandtl number
p’	Cell pressure correction
Re	Reynolds number
Re_y	Wall distance based Reynolds number
U	Local velocity
u	x component of velocity
u^+	Dimensionless velocity

$\bar{u}_i$	Mean part of velocity
u'_i	Fluctuating part of velocity
u_τ	Friction velocity
v	y component of velocity
w	z component of velocity
y^+	Dimensionless distance from the wall
α_p	Under-relaxation factor for pressure
β	Thermal expansion coefficient
Γ	Diffusion coefficient
γ	Kinematic viscosity
δ	Boundary layer thickness
ϵ	Turbulence dissipation rate
η	Body fixed coordinate normal to the body
θ	Momentum thickness
μ	Dynamic viscosity
μ_t	Turbulent viscosity
ξ	Body fixed coordinate along the body
ρ	Density
$-\rho\overline{u'_i u'_j}$	Reynolds stresses
ϕ	Any fluid property
τ_w	Wall shear stress
τ_{ij}	Viscous stresses
$\overline{\Omega_{ij}}$	Mean rate of rotation tensor
∇	Gradient operator
CFD	Computational fluid dynamics
DNS	Direct numerical simulation
GUI	Graphical user interface
LDA	Laser doppler anemometry
MDR	Maximum drag reduction

ppm	Part per million
rpm	Revolutions per minute

1. INTRODUCTION

Speed has always been the passion of human since the wheel was invented. Today human can travel at supersonic speeds but still not satisfied. Up to now many studies have been performed related with the improvement of speed in vehicles. The studies were in a wide variety including lowering resistances and were concentrated on lubrication and drag reduction. Since the reduction of drag does not only improve the speed but also provides energy savings the studies have never been stopped and gained greater importance during the oil crisis in 1970s. Following those years the researches in finding new energy resources have been executed together with the reduction of drag which is still studied with the same interest in the enlightenment of the discoveries and new inventions.

The drag mainly consists of two parts, pressure and friction drag. Pressure drag was probably considered the main cause for drag on vehicles in the past but after the invention of boundary layer theory it was seen that frictional forces also contribute to the drag and in some occasions they have more share in total drag force. The observations also led to the fact, separation, which changed the design considerations in transports. Basically, the vehicles had been started to design in a fashion that the flowfield surrounds the body. As called streamlined bodies, the effect of pressure drag was reduced. Shaping the body in order to reduce the drag is the most conventional method for drag reduction which can provide pressure and friction drag reduction.

The influence of surface friction on total resistance on vehicles is large since most of the vehicles are streamlined bodies. The rate of surface friction to the total resistance is usually 50% for ordinary civil airplane and ships, 70% for submarine and nearly 100% for long-distance pipe transportation [1]. In most regions of these vehicles the flow is turbulent and therefore the shear is high and turbulent drag reduction which is the delaying of the onset of turbulent flows, has always been considered on these systems.

1.1. Torpedoes

Torpedoes are underwater self-propelled projectiles. They are launched above or below the water and they detonate on contact or in proximity to a target. Torpedoes may be launched from submarines, surface ships and even helicopters [2]. Torpedoes were also called underwater mines. The term ”torpedo” was first used by Robert Fulton who used it for the towed gunpowder charge used by his submarine Nautilus. In 1800-1805 he performed some demonstrations that it could sink warships. However, the first prototype of a self-propelled torpedo was created by Ivan Lupis-Vukić. He was a retired Croatian naval engineer and he served in the Austro-Hungarian Navy. He presented his design to the Emperor Franz Joseph in the port city of Rijeka in 1860. Robert Whitehead, who was an English engineer and entrepreneur, was working in the Trieste port on navy projects. They came together in 1864 and Lupis made a contract with him in order to improve the invention. This cooperation yielded the the first self-propelling torpedo in history [2].

Figure 1.1. A torpedo launched from a battleship [3]

However, the invention is usually attributed to Whitehead, since he made all the improvements. The first weapon was fired from underwater tubes. There was a pendulum-hydrostat gear to maintain the constant depth. The horizontal direction was provided with the use of azimuth. The engine was driven by compressed air. The range of the weapon was around 400 meters and the maximum speed was 6 - 6.5 knots ($\simeq 3 - 3.25$ m/s) with a propeller speed of 100 rpm [4].

In time, Whitehead torpedoes gained fame in the world. The countries made contracts with Whitehead for his weapon. While some countries chose to examine and improve the weapon like Germans did. Later, the nose of the geometry was changed. At first there was a pointed nose which was considered to cleave the water best. However, later studies showed that the blunt nose has no disadvantage in speed.

In 1895, the control mechanism was improved with the introduction of the gyroscope. Whitehead adapted the gyroscope invented by Ludwig Obry to his torpedoes. Soon, the ranges and the accuracy were improved with the adaption. Passing the two World wars torpedo completed most of its development. Today, there are different types of torpedoes classified according to their weight, control mechanism, power supply and their functions [4].

A torpedo consists of mainly four parts named as nose, body, afterbody and tail. The weight of the torpedoes change with the addition of a warhead and they are usually categorized as lightweight and heavyweight torpedoes. The range of a torpedo can exceed 25 km depending on its weight and power supply system. The power is supplied from combustion or chemically or electrically driven engines. The control of the torpedo can be done with remote control or acoustic homing devices which can track the underwater vehicles through the use of sound.

1.1.1. Supercavitating Torpedoes

Supercavitation is the use of cavitation[1] to create a large bubble of gas inside a liquid in order to separate the surface of the object from the liquid and making the object to travel at a great speed through the liquid by being wholly surrounded by the bubble. The cavitation reduces the drag on the object and since the drag is normally about 1,000 times greater in water than in air this makes supercavitation a very attractive technology [2].

In 1977, Russian engineers developed the VA-111 Shkval torpedo (the first projectile to use supercavitation) which can travel at 100 m/s underwater. A comparison with the conventional aquatic craft (the top speed of 35 m/s) identifies the importance of the situation. Although it was invented in 1977, it was noticed in West from a malfunctioning Shkval torpedo in 1990s. A weakness of Shkval (as reported) is that it is not steerable [2]. Since it flows in a cavity of water vapor initialized at the forward mounted cavitator, the torpedo body is only in contact with the water at the cavitator and rear control fins. This minimal contact results in stability issues that are not present in conventional, fully wetted torpedoes [5].

---

[1] Cavitation occurs when water is forced to move at extremely high speed (e.g. inside a rapidly spinning propeller). Due to the high speed, the pressure of the fluid drops according to Bernoulli's principle. When the pressure drops below the vapor pressure of the water, the fluid vaporizes or in other words forms small bubbles of water vapour [2].

1.2. Drag Reduction

All transports travel in a medium and that medium applies resistance forces on the transport like the drag force. Drag reduction is important since it provides high speed with limited engine power, besides decreases the energy consumption. Since the drag force is an addition of different effects, mainly friction drag and pressure drag, reducing one of them will make the total drag force decreased.

Body shaping is the most known method in drag reduction and the term drag reduction evokes in peoples minds the body shaping. Body shaping studies do not end for a certain model since the minimum drag for the body can not be estimated especially if the model involves several boundary conditions and design considerations.

One alternative of body shaping method is reduction of friction drag[2] . It attracts the attentions because the reduction can climb up to a percentage of 80%.

Friction drag which is also called skin or surface friction can be minimized by extending the laminar boundary layer. Surface friction is related to the velocity gradient across the boundary layer. Since the lowest velocity gradient is in laminar boundary layer, the surface friction is also lower compared to the surface friction in turbulent boundary layer [6].

---

[2] Friction drag can also be reduced by body shaping but here reduction of friction is referred to more specific methods.

1.2.1. Body Shaping

Body shaping is the generation of new shapes in order to find the optimum geometry for a vehicle or an object. In a vehicle, the geometry depends on the structure, the use, the volume and the artistic design. In addition, a hydrodynamic or aerodynamic design of the body is necessary when drag reduction is desired. However, the generation of new shapes does not mean to disregard the other design criteria. There must be a strong relationship among them and only small deviations from each is acceptable.

The relationship between the geometry and the structure is critical for any engineering design. In vehicles, the geometry has a strong relation with the structure and safety characteristics. Another limitation of the geometry is the use of the object, usually emanates from the aim and need of it. In an acoustic torpedo the nose should be flat. The volume of the geometry depends on the inside volume which is maximized to keep certain equipments. Again for the torpedo example, the inside volume should cover the electronic equipments, the engine and the warhead. The artistic design has also a role in geometry but it is performed in end consumer products. The initial geometry is defined using the most critical dependance of the geometry. For an automobile it is the artistic view, for a combat vehicle it is the structure and for a missile or a torpedo it is the hydrodynamic or aerodynamic behavior.

The relation between the geometry and the hydrodynamic or aerodynamic forces is an obvious fact. In CFD, body shaping means altering the geometry in order to achieve the desired force components. For a torpedo, a long and thin geometry is the best choice since it provides lower drag forces so basically the geometries are chosen as long and thin. Considering the other design criteria, reasonable geometries are generated and each geometry is evaluated using computational tools. Finally, the optimum geometry is chosen.

1.2.2. Shape Generation in Axisymmetric Bodies

In any type of body the smoothness of the geometry affects the behavior of the boundary layer so the drag components. The smoothness of the geometry is strongly related to the continuity of the geometry. Besides, it is a well known fact that sharp corners and turns are avoided when the drag reduction is desired and this sharpness can be avoided using continuous geometries.

In a body of revolution the generation of new geometries can be achieved using basic shapes. By using ellipses and parabolas different geometries can be constructed. The study of Kanikdale is a good study for axisymmetric body shaping.

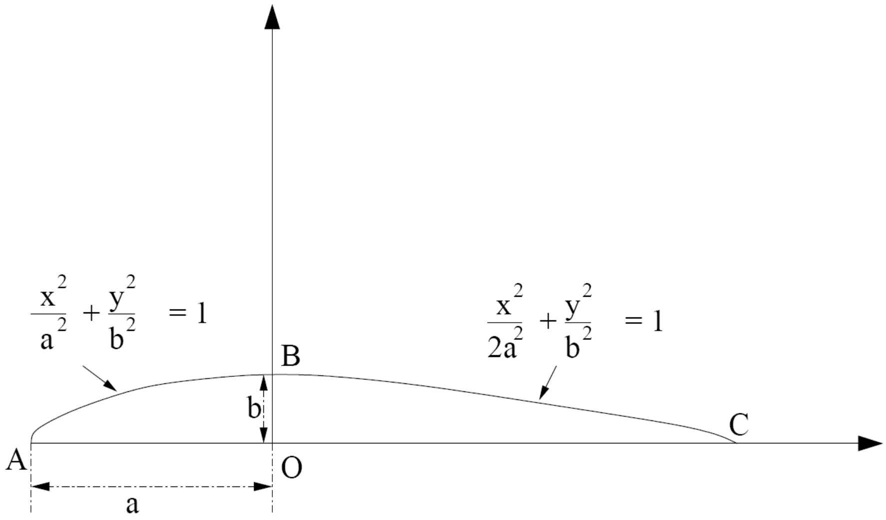

Figure 1.2. The geometry of two ellipse [7]

In study of Kanikdale, two different ellipses (one for forebody and one for afterbody Figure 1.2) are joined to find the best geometry in an airship design. To provide a smoother geometry a parabola is added to the end of the afterbody (Figure 1.3). However, at point C the slopes of the ellipse and parabola should be equal to achieve continuity. This way, several geometries can be generated [7].

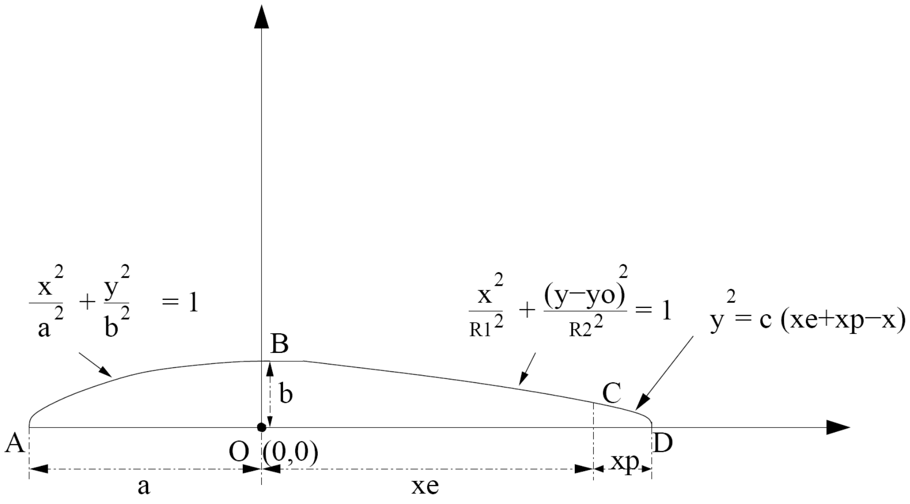

Figure 1.3. The geometry of two ellipse and a parabola [7]

The generated geometries (Figure 1.4) are compared using computational tools. With the help of the CFD, the drag force is estimated for each shape and the most efficient shape is determined. This method can be applied in generation of new shapes for torpedoes.

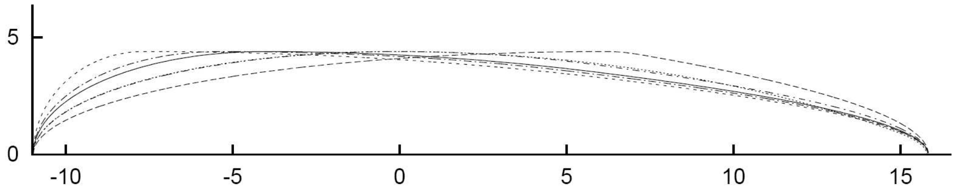

Figure 1.4. The generated geometries [7]

1.2.3. Polymer Induced Drag Reduction

Polymer injection is one of the techniques used to reduce surface friction since 1950s. During the second world war while scientists were trying to experiment with gelled gasoline they observed an extraordinary event, polymer-induced drag reduction. It was observed approximately at the same time in both US and UK. The phenomenon says that addition of even a minute amount[3] of high molecular weight polymer to a low molecular weight solvent yields drag reduction in fully turbulent flow. However, this phenomenon could not be publicly announced because of the war secrecy and it was rediscovered by British chemist Toms [8]. He observed it accidentally in the summer of 1946 when he was investigating the mechanical degradation of some polymers in pipe flow. According to his words "polymer solution clearly offered less resistance to flow, under constant pressure, than the solvent itself". Although the phenomenon is known as Toms effect there are conflicts in ownership of the theory since one year earlier Mysels [9] discovered that addition of an aluminium soap to gasoline lowered the friction in turbulent pipe flow. Because of wartime restrictions publication could be done in 1949.

Polymer injection can provide great levels of drag reduction. The technique involves injecting a dilute polymer solution into the boundary layer of a flow. It should be mentioned that the reduction occurs at very low concentrations in the ppm region. According to an experimental study, reduction of drag at a percentage of 22% was achieved on a hydrofoil section operating at a Reynolds number of 1.6×10^6 using distributed injection of a Polyox polymer at 5, 10 and 30% of overall chord length. The water injection also showed a small drag reduction of about 2% [10].

Experiments show that the polymers with higher molecular weight are more effective drag reducers (Figure 1.5). The drag reduction also depends on the level of concentration. The raising of the concentration up to a certain level yields in reduction of drag (Figure 1.6). Furthermore, the longer polymer chain provides more possibility

---

[3] These solutions are usually in order of ppms, part per million, which means 1 molecule of solute in 1 million molecules of solvent.

Table 1.1. Drag reducing polymer solutions [11]

Water-soluble polymers	Solvent-soluble polymers
Poly(ethylene oxide)	Polyisobutylene
Polyacrylamide	Polystyrene
Guar gum	Poly(methyl methacrylate)
Xanthan gum	Polydimethylsiloxane
Carboxymethyl cellulose	Poly(cis-isoprene)
Hydroxyethyl cellulose	

of interaction with the flow. It has been confirmed that the extension of the polymer chain is critical for drag reduction. The most effective drag reducing polymers are generally in linear structure with maximum extensivity for a given molecular weight. Poly(ethyleneoxide), polyisobutylene and polyacrylamide are the best examples of this type [11].

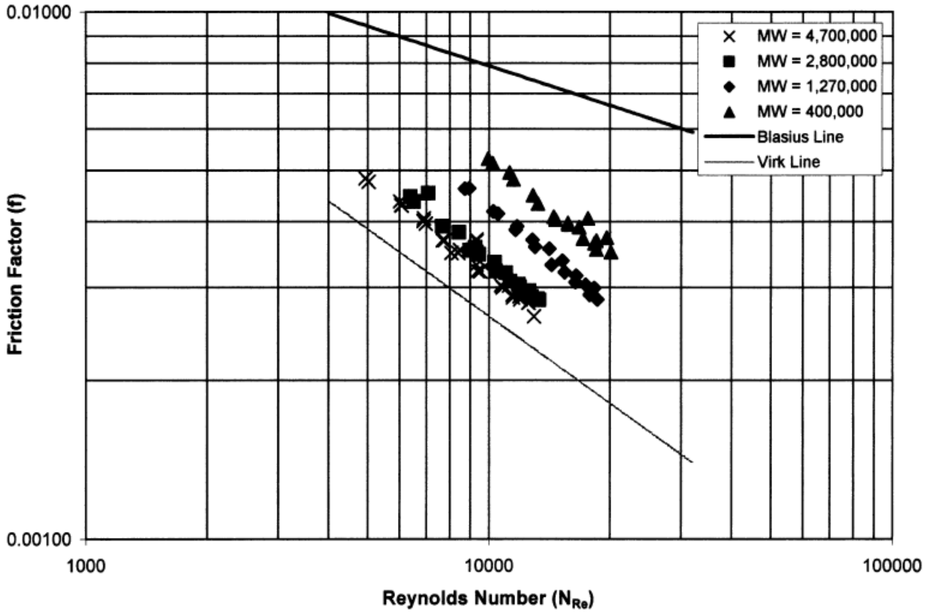

Figure 1.5. The effect of polyisobutylene molecular weight on turbulent flow friction factor for solutions of polyisobutylene in cyclohexane (0.001 g/ml) [12]

1.2.4. Drag Reduction with Microbubbles

Microbubble-modified boundary layer and skin friction reduction have been an active area of research for ship hull in recent years because of its energy saving potential.

Like the polymer induced drag reduction the injection of gas into a liquid turbulent boundary layer with forming bubbles reduces surface friction drag as much as 80%. Although it had been known that a layer of air next to a surface in water reduces turbulent surface friction, the concept of the microbubble-modified boundary layer came into existence in its present form with the contributions of McCormick and Bhattacharyya [11].

They used a copper wire coiled around a body of revolution to produce hydrogen bubbles by electrolysis. As a result of their experiments it was accepted that microbubbles could increase the drag with increasing gas generation rate and reduce total drag with decreasing gas generation rate. The results were limited to Reynolds numbers between 0.3 and 1.8 million.

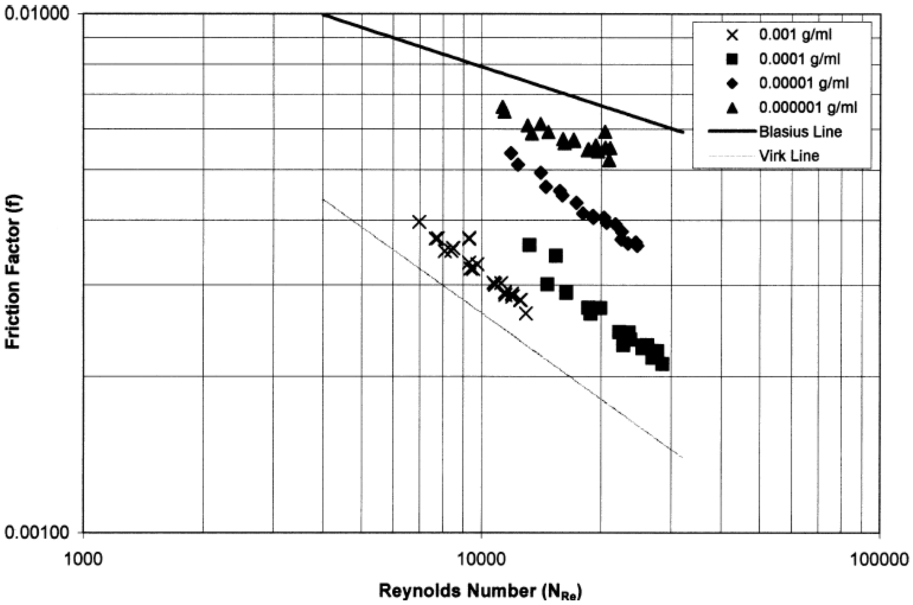

Figure 1.6. The effect of polyisobutylene concentration on turbulent flow friction factor for solutions of polyisobutylene in cyclohexane (0.001 g/ml) [12]

In microbubble drag reduction the size of the bubbles is a determinative parameter. Merkle and Deutsch studied the effects of the size of bubbles. The diameters of the bubbles affect their trajectories and thus their concentration and location in the boundary layer. Measurements of bubble sizes indicate that the bubble size decreases when free stream speed is increased and increases when airflow rate is increased. However bubbles show little dependence on the injection procedure [11].

1.2.5. Riblets

Beginning with the 1970s NASA Langley Center pioneered a drag reduction research which yielded an unexpected result. The micro-grooves called riblets (Figure 1.8) reduced the surface friction efficiently when placed on the surface parallel to the streamwise direction [1]. The same event is found also in sharks and they have a method to counteract friction, using tiny riblets along their skins. All fast swimming sharks have sharp-edged riblets [13].

During the experimental investigations on turbulent boundary layer flow it is found that the optimum design of the drag reduction surface is a symmetrical V-shaped

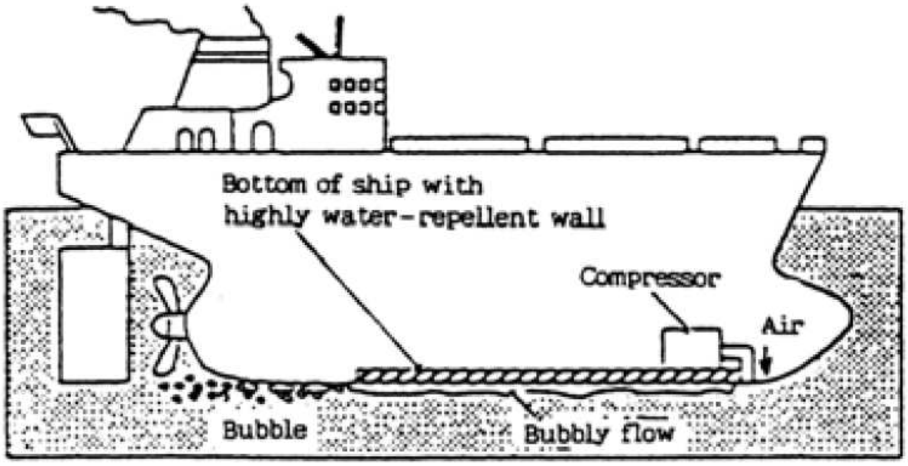

Figure 1.7. Model of drag reduction systems for a ship [11]

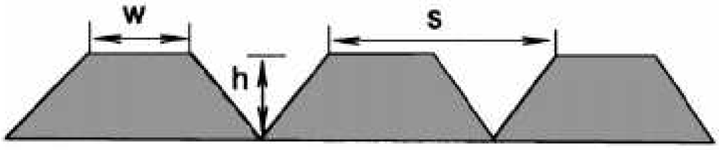

Figure 1.8. Cross-section of the riblet plate [1]

riblet surface with its non-dimensional width and height of 15. It has a maximum value of drag reduction of 8%. Coustols defined the effect of riblet width, height and the yaw angle on drag reduction. He claimed that drag reduction is 7-8% for airfoil and body of revolutions. In another experiment of a revolution body, a drag reduction of 9% was obtained. However, the design of the riblet surface has not reached the theoretical level. Moreover, it is not clear that whether the drag reduction of 8-9% is the upper bound [1].

In the experimental work conducted by Bechert who focused on reproducing the condition of shark skin in a laboratory, attempts to optimize the drag reducing effects of riblets could not show large (>8%) improvement over smooth surfaces. No riblet geometry has shown better drag reduction than the skin of fast-swimming sharks [13].

2. THEORY

In fluid mechanics when a body is immersed in a fluid and fluid has a relative or absolute motion around the body, the flow is identified as external flow. Dynamics of external fluid flow mostly deal with vehicles and moving objects. In addition, the flow passed a stationary body is also examined. In both conditions the flow equations are solved using the assumption that the body is stationary even it is not. If the body has a motion the coordinate system is transformed into vehicle-body fixed coordinate system using the Galilean transformation. This yields a stationary body and a uniform flow field far from the body. The flow field is steady relative to the axes fixed to the body, so the equations are usually solved easier in body fixed coordinate system than in the ground fixed coordinate system.

The fluid is assumed to move toward the body with the upstream velocity U_∞ which is actually the velocity of the body. The particles in free stream far from the body have no relative motion since they have the same velocity and there are no shearing stresses in the flow. If there is no relative motion between fluid particles, the fluid is called a static medium in which the static fluid properties are the same for either coordinate system [14].

The flow near the body may be steady even though the uniform upstream flow is steady. The problems usually arouse in the vicinity of the body for which the boundary layer theory was invented. In the enlightenment of this theory the flow field and its effects are examined by engineers and scientists.

2.1. Drag

The movement of an object in space is not usually easy since the object is exposed to external forces resisting to its motion. This is friction force on a moving box on a plate and drag force on a flying plane or an advancing torpedo onto its target. The drag force depends on the medium, shape, velocity and orientation of the object. It is composed of two components, the wall shear stresses due to viscous effects and normal stresses due to pressure. The resultant force in the direction of the upstream velocity is termed the drag and the resultant force normal to the upstream velocity is termed the lift. These forces are calculated by integrating the pressure and shear stress along the surface of the object [15]. In order to carry out these integrations the shape of the body and the distributions of pressure and shear stresses must be known. This is usually achieved with the aid of CFD tools or experiments.

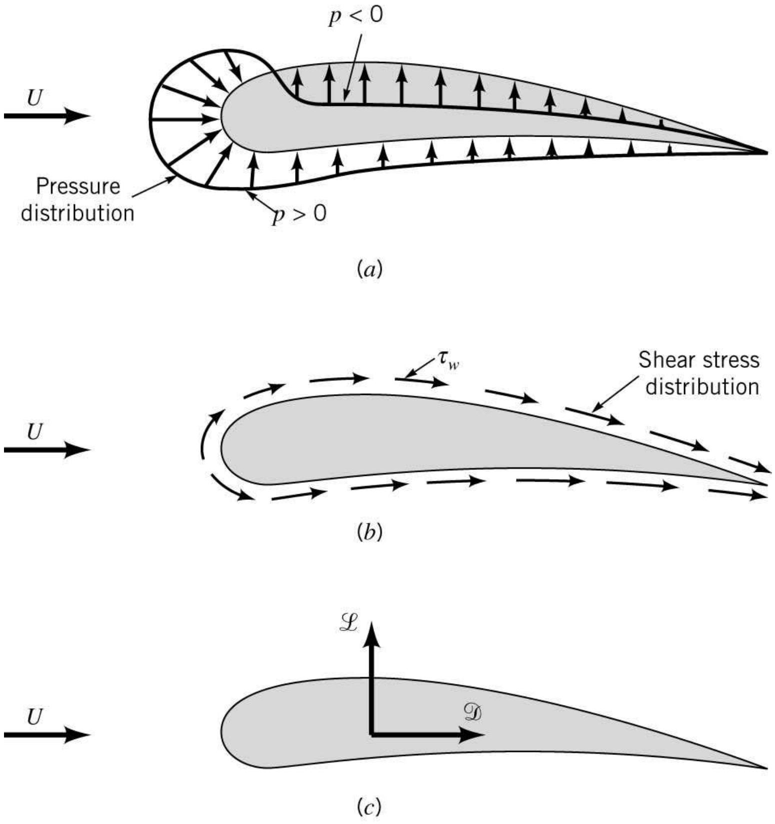

Figure 2.1. The fluid flow forces on a body: a)Pressure force, b)Viscous force, c)Resultant forces [15]

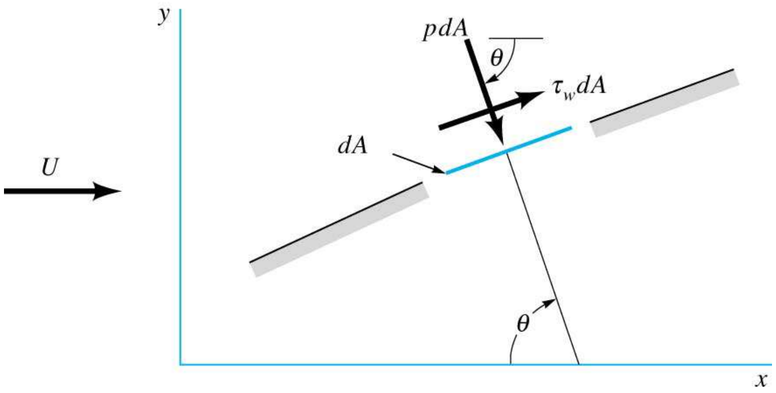

Figure 2.2. Pressure and shear forces on a small element of the surface of a body [15]

In Figure 2.2 the shear and pressure forces are shown on a small surface element. The x and y components of the fluid force on the small element dA are

$$dF_x = (pdA)\cos\theta + (\tau_w dA)\sin\theta \tag{2.1}$$

and

$$dF_y = -(pdA)\sin\theta + (\tau_w dA)\cos\theta \tag{2.2}$$

and the net force components on the object are

$$D = \int dF_x = \int p\cos\theta dA + \int \tau_w \sin\theta dA \tag{2.3}$$

and

$$L = \int dF_y = -\int p\sin\theta dA + \int \tau_w \cos\theta dA \tag{2.4}$$

The drag coefficient and lift coefficient are defined as:

$$C_L = \frac{L}{\frac{1}{2}\rho U^2 A} \tag{2.5}$$

and

$$C_D = \frac{D}{\frac{1}{2}\rho U^2 A} \tag{2.6}$$

where A is the characteristic area of the object.

2.1.1. Pressure Drag

The component of the drag that emanates from the the pressure effects on a body is called the pressure drag. It is also named as form drag because there is a significant dependence between the pressure drag and the form of the body. Pressure drag is related to the pressure distribution on the object. However, the drag force on an object for the same flow may not be equal at all times. There is also a dependence of drag on the orientation of the object. The pressure drag force on a vertical plate will be larger than the same plate if it is set horizontal [15].

The design parameters include mostly the shape of the object for pressure drag force. The limitations that come from the mechanical design and use of the object are taken into consideration and a design is performed using generally tools of CFD.

Since the pressure drag depends on the pressure distribution around the object it must be altered somehow in the favor of the aimed. In order to decrease the pressure drag, the pressure distribution upstream must be lowered while the pressure downstream must be increased to ensure uniform pressure around the object.

Simply, the ratio of height to length is a point that gives a notion about the magnitude of the drag force. The pressure drag can be obtained using Equation 2.3 with a detailed information on distribution of pressure and the body shape.

$$D_p = \int \cos\theta dA \tag{2.7}$$

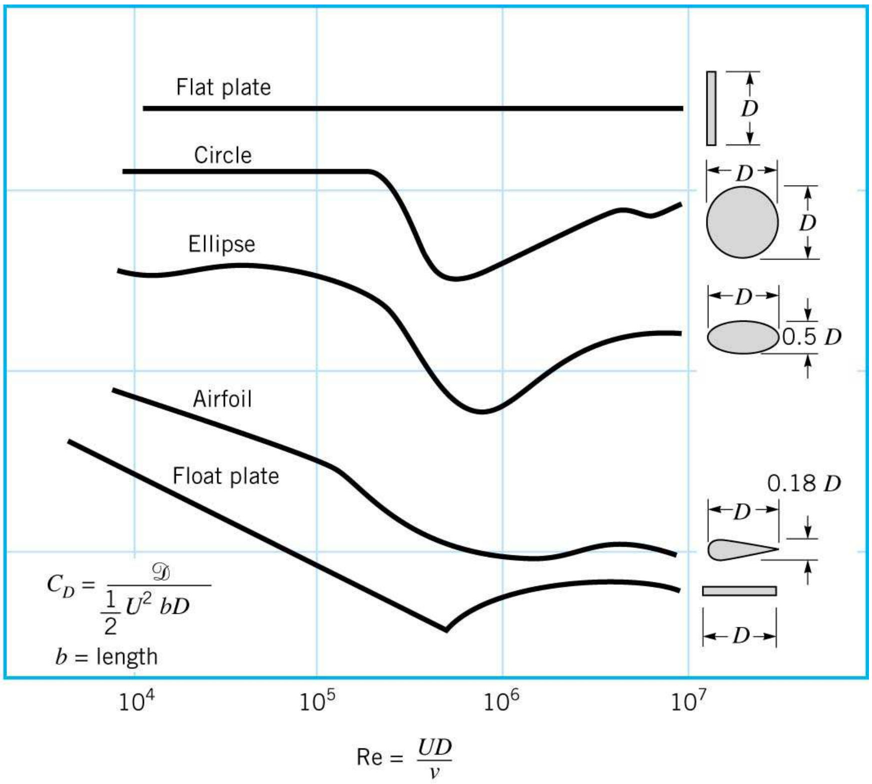

Figure 2.3. Pressure and shear forces on a small element of the surface of a body [15]

Introducing Equation 2.7 into the pressure drag coefficient gives,

$$C_{Dp} = \frac{D_p}{\frac{1}{2}\rho U^2 A} = \frac{\int \cos\theta dA}{\frac{1}{2}\rho U^2 A} = \frac{\int C_p \cos\theta dA}{A} \tag{2.8}$$

where C_p is the pressure coefficient.

$$C_p = \frac{(p - p_0)}{\frac{1}{2}\rho U^2} \tag{2.9}$$

2.1.2. Friction Drag

Friction drag, which is also known as viscous drag is the part of the drag that is due to shear stresses on the surface of an object. In real life since there is not an inviscid case, there is always a friction drag acting on objects. Only in some situations this type of drag is so small compared with other types of drag and may be neglected. However, friction drag has great importance that boundary layer theory was invented to explain the viscous drag. It depends not only on the magnitude of the wall shear stress but also the orientation of the surface on which it acts. If the surface lays parallel to streamlines in a uniform flow the whole shear stress contributes to the drag but if it lays perpendicular the shear stress it will contribute to lift rather than drag [15].

The friction drag can be obtained from the wall shear stress distribution. The friction drag coefficient and local friction coefficient are as follows:

$$C_{Df} = \frac{D_f}{\frac{1}{2}\rho U^2 A} \tag{2.10}$$

and local friction coefficient is

$$C_f = \frac{\tau_w}{\frac{1}{2}\rho U^2} \tag{2.11}$$

2.1.3. Vortex Shedding

At Reynolds number larger than a certain value ($Re > 40$ for cylinder) the boundary layer over the surface of a body separates due to the adverse pressure gradient, affected from the divergent behavior of the flow at the rear side of the body. As a result a shear layer is formed. Since the boundary layer along the body has a significant amount of vorticity, this results in a shear layer downstream of the separation point and causes the shear layer to roll up into a vortex. A vortex rotating in the opposite direction will be formed at the other side of the body. This is called vortex shedding [16].

The larger vortex becomes strong enough to draw the opposite vertex across the wake, as seen in Figure 2.4. The vorticity in vortex A is in clockwise, while that in vortex B is in anti-clockwise direction. The approach of vorticity of the opposite sign cuts off supply of vorticity to vortex A from its boundary layer. It can be said that vortex A is shed. Being a free vortex, vortex A is then convected downstream by the flow. Following the shedding of vortex A a new vortex is formed at the same side of the cylinder (vortex C). Vortex C plays the same role as A it grows and draws C across the wake. This is the shedding of vortex B. This continues each time a vortex is shed at one side of the cylinder and the result is a vortex street at the wake of the cylinder [16].

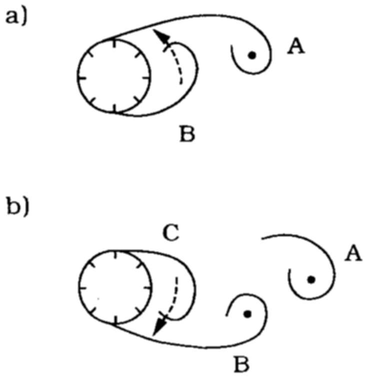

Figure 2.4. Shedding process of vortices [16]

Vortex shedding frequency is related with Strouhal number St. $St = F_v D/U$ where F_v is the vortex shedding frequency. Vortex shedding causes oscillations on the body. These oscillations affect the drag forces and oscillations occur in drag forces [16].

2.1.4. Separation

In an external flow, the body is surrounded with a moving fluid and the passage or the pathway of the fluid is determined by the body. If the body is a complex geometry, a complex flow field is expected. However, there may be complicated flow fields around simple objects like a cylinder. The streamlines, which are the pathways of the flow and an expression of the flow field, can not attach to the surface of the object around which they align. This means that the streamlines do not completely surround the object and follow a different pathway. The fact that separates the flow field from the boundary of the object is separation [15].

Separation does not depend on only the shape since on the same geometry there are cases surely no separation exists. It depends also on the properties of the fluid such as density, viscosity and velocity. Separation can be simply explained with Reynolds number, which is a ratio of inertial effects to viscous effects.

Figure 2.5 best depicts the occurrence of separation. At low Reynolds numbers viscous effects are important even far away from the body. Streamlines seem more likely cover the body and the streamline pattern is nearly same at the back of the body with the one ahead of the body.

As the Reynolds number is increased, viscous effects retreat in the front region of the cylinder. The flow loses its symmetry since the viscous effects are convected downstream. Separation arises at this point since the fluids inertia is high and it can not follow the curved path after the body. The separation of the boundary layer initiates the creation of a wake and a wake region with low pressure magnitudes causes the form drag to increase [15].

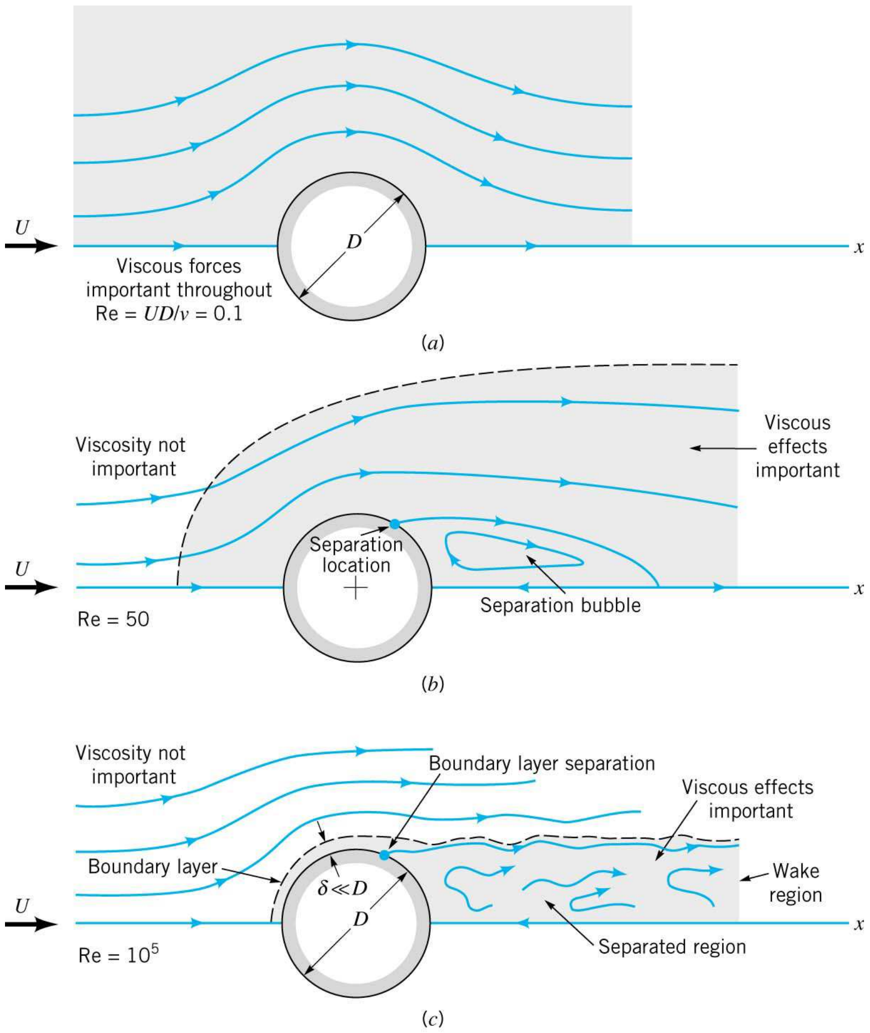

Figure 2.5. Character of the steady, viscous flow past a circular cylinder: a)Low Reynolds number flow, b)Moderate Reynolds number flow c)Large Reynolds number flow [15]

2.2. Basics of the Boundary Layer Theory

In turbulent thin shear layer flows, a Reynolds number based on a length scale is very large (for a case $U = 1\ m/s, L = 0.1\, m$ and $\nu = 10^{-6}\, m^2/s,\ Re_L = 10^5$). Since the definition of the Reynolds number is the ratio of inertial forces to viscous effects at this value of Reynolds number the inertia forces will be dominant. If another Reynolds number based on a distance y away from the wall is formed ($Re_y = Uy/\nu$) then at a value near L the above argument will be valid such that far away from the wall, inertia forces dominate the flow. However, if y is chosen close to the wall Re_y will be small and viscous forces will dominate the flow. If the y is chosen so that $Re_y = 1$ viscous forces will be equal to inertia forces. Briefly, the region far away from the wall is inertia dominated while in the region close to wall viscous effects are dominant [17].

In the near wall region, the flow is affected by viscous effects and free stream relations are not valid. Dimensional analysis for mean flow velocity where $U = f(y, \rho, \mu, \tau_w)$ expresses the following relation

$$u^+ = \frac{U}{u_\tau} = f\left(\frac{\rho u_\tau y}{\mu}\right) = f(y^+) \tag{2.12}$$

This is called law of the wall and contains two new dimensionless groups u^+ and y^+

$$u_\tau = \sqrt{\tau_w/\rho} \tag{2.13}$$

$$y^+ = \frac{u_\tau y}{\nu} \tag{2.14}$$

where u_τ is called friction velocity.

Making a dimensional analysis yields

$$u^+ = \frac{U}{u_\tau} = g\left(\frac{y}{\delta}\right) \tag{2.15}$$

Relating the velocity deficit $U_{max} - U$ to the wall shear stress gives

$$\frac{U_{max} - U}{u_\tau} = g\left(\frac{y}{\delta}\right) \tag{2.16}$$

the so called velocity-defect law [17].

2.2.1. Linear Sublayer

At the wall, the fluid has no motion even that the turbulent eddying motions stop when they reach very close to the wall. Viscous shear is the only dominant parameter when there is no turbulent shear stress. In practice this layer is so thin that the shear stress is assumed almost constant and equal to the wall shear stress τ_w among the layer. Therefore

$$\tau(y) = \mu \frac{\partial U}{\partial y} \cong \tau_w \tag{2.17}$$

Integrating with respect to y with a boundary condition $U = 0 \ \ at \ \ y = 0$ gives a relationship between the mean velocity and the distance from the wall

$$U = \frac{\tau_w y}{\mu} \tag{2.18}$$

which leads to $u^+ = y^+$. The linear relationship between velocity and distance from the wall makes this layer named as linear sub-layer [17].

2.2.2. Log-law Layer

The region in $30 < y^+ < 500$ is exposed to both viscous and turbulent effects. The shear stress τ changes slowly as moving away from the wall and within this region it is assumed to be equal to the wall shear stress. One more assumption about the length scale of turbulence (mixing length $l_m = \kappa\, y$) leads to a relationship between u^+

and y^+

$$u^+ = \frac{1}{\kappa}\ln y^+ + B = \frac{1}{\kappa}\ln(Ey^+) \tag{2.19}$$

The relation is called the log-law and the region between $y^+ = 30$ and $y^+ = 500$ is called the log-law layer. For smooth walls $\kappa = 0.4$, B= 5.5 (or E = 9.8) and wall roughness makes B decreased.

2.2.3. Outer Layer

It is seen from experiments that log-law is valid in the region $0.02 < y/\delta < 0.2$. For larger values of y Equation 2.16 (velocity-defect law) provides appropriate form. In the overlap region, the log-law and the velocity-defect law becomes equal. A matched overlap is obtained by assuming the following logarithmic form

$$\frac{U_{\max} - U}{u_\tau} = \frac{1}{\kappa}\ln\left(\frac{y}{\delta}\right) + A \tag{2.20}$$

where A is constant. This law is called law of the wake.

The mean velocity is at its maximum value far away from the wall and due to no slip condition, it sharply decreases in the region $y/\delta \leq 0.2$. High values of $\overline{u'^2}, \overline{\nu'^2}, \overline{w'^2}$ and $\overline{u'\nu'}$ are found adjacent to the wall where the high turbulence production is ensured by large mean velocity gradients. Eddies and velocity fluctuations are affected from the no-slip condition at the wall. Since the production process mainly creates component $\overline{u'^2}$ the turbulence is anisotropic near the wall. The turbulence properties asymptotically vanishes as y/δ increases above a value of 0.8 . The rms values of all fluctuating velocities become nearly equal which means the turbulence structure becomes more isotropic far away from the wall [17].

2.3. Maximum Drag Reduction Theory

Virk discovered the relationship between the friction factor and the Reynolds number for the maximum drag (friction drag) reduction (MDR) case of polymer solutions [18]. He investigated the turbulent effects on dilute polymer solutions in pipe flow. During his studies he showed that no polymer solution can exceed the MDR line. Although there are some rare studies in literature for cases exceeding the MDR, the theory is accepted among the scientists.

In laminar pipe flow, the dilute polymer solutions show nothing unusual. The most of all obey Poiseuille's law which is

$$f^{-1/2} = Ref^{1/2}16 \tag{2.21}$$

where f is the Fanning friction factor and Re is the Reynolds number. The viscosities of solution are generally close to solvent that shear thinning has little effect. In fully turbulent pipe flows, three different regimes exist which are;

- A regime without drag reduction in which the relationship for the friction factor is same with the solvent. It is the Prandtl-Karman (or Blasius) law for Newtonian turbulent flow which is

$$f^{-1/2} = 4.0 \log Ref^{1/2} - 0.4 \tag{2.22}$$

- A drag reduction regime in which friction factor depends upon the nature of the polymer solution

$$f^{-1/2} = (4.0 + \Delta) \log(Ref^{1/2}) - 0.4 - \Delta \log \sqrt{2}W^{*} \tag{2.23}$$

where Δ and W^{*} are polymer solution parameters.

- An asymptotic regime of maximum possible drag reduction in which the friction factor has no relation with the polymer solution

$$f^{-1/2} = 19 \log Ref^{1/2} - 32.4 \tag{2.24}$$

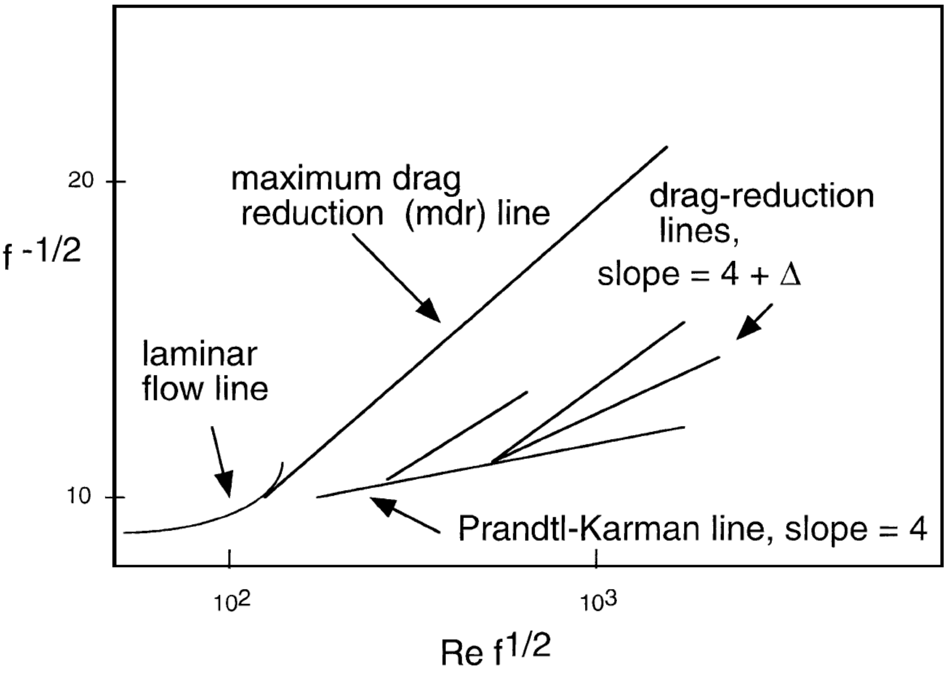

Figure 2.6. Schematic drawing of Prandtl-Karman plot of $f^{-1/2}$ vs. $Ref^{1/2}$ with and without polymer drag reduction [19]

2.3.1. Law of the Wall

In the absence of drag reduction and polymers, Newtonian fluids obey the following velocity profile which is called law of the wall.

$$U^+ = y^+, \qquad y^+ < 11.6 \tag{2.25}$$

$$U^+ = 2.5 \ln y^+ + 5.5, \qquad y^+ > 11.6 \tag{2.26}$$

However, if drag reducer agents are added the figure changes. Polymer solutions adhere to the Newtonian wall at zero drag reduction. At low drag reductions the polymer solutions have profiles which are shifted upward from the Newtonian law of the wall. The shift is called the effective slip S^+ and increases with increasing drag reduction. At maximum drag reduction conditions the whole profile is approximately semi-logarithmic with a slope of 11.7 [18].

Introducing the shift amount S^+ to the Equation 2.26 yields

$$U^+ = 2.5 \ln y^+ + 5.5 + S^+ \tag{2.27}$$

Furthermore, an intermediate polymer buffer layer is introduced which obeys

$$U^+ = 11.7 \ln y^+ - 17.0 \tag{2.28}$$

S^+ can be identified as follows:

$$S^+ = \sqrt{2} \log \left(\frac{u_\tau}{u_\tau^*} \right) \Delta \tag{2.29}$$

$$\Delta = \kappa N^{3/2} (\frac{c}{M})^{1/2} \tag{2.30}$$

where u_τ^* is the turbulent velocity scale at the critical shear stress for drag reduction. Δ is the amount of shift, seen in Figure 2.6. N is the number of backbone bonds in the polymer, M is the molecular weight of the polymer (g/mol) and c is the concentration in ppm [19].

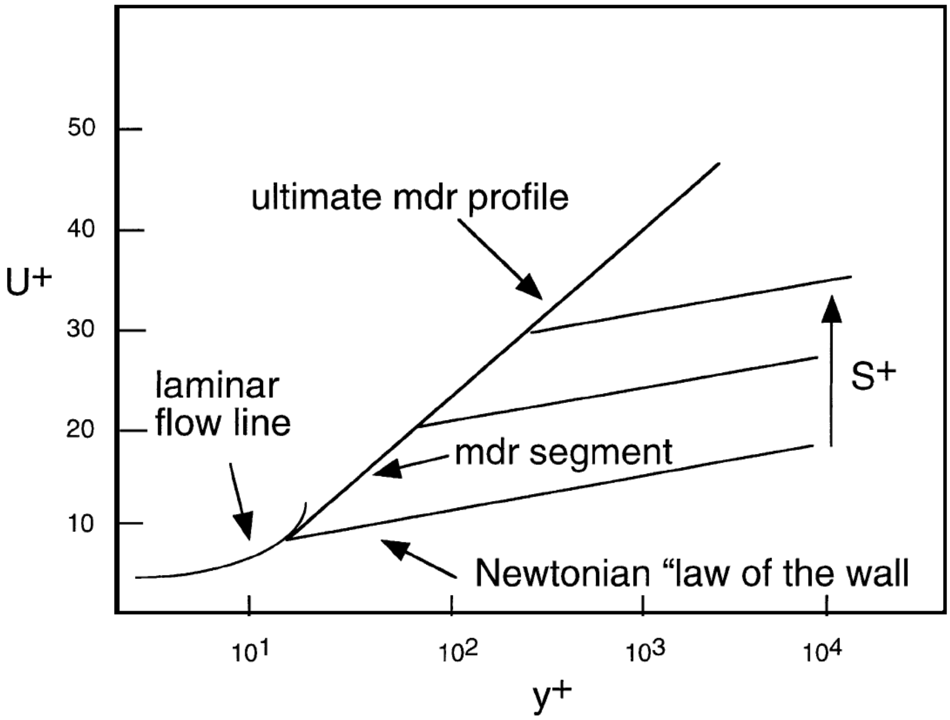

Figure 2.7. Velocity profiles with and without drag reduction [19]

2.3.2. Flat Plate Solution for Polymer Induced Flows

Using the well established phenomology for flow in a tube, Larson [19] developed a model for flat plates in presence of polymeric drag reduction. He derived his model assuming that the flat plates are in a polymer ocean rather than studying the injection or changing of concentration. Since the Virk's findings are not enough to make a relation with an external flow he proposed to derive the relations of a flat plate based on Virk's study.

According to his study, a velocity profile is found which is a generalization of Equations 2.7, 2.27 and 2.28.

$$U=\frac{u_\tau}{K}\left[\ln\frac{u_\tau y}{\nu}+A\right]+\frac{\sqrt{2}u_\tau\Delta}{2.303}\ln\frac{u_\tau}{u_\tau^*} \tag{2.31}$$

In the Equation 2.31 if 0.4 is assigned to K and 2.2 to A then Equation 2.27 is found and assigning other values yields the other wall equations.

From the requirement of $U(\delta)=U_1$ it is found that

$$\delta=\frac{\nu}{KU_1}\frac{1}{\nu}\left[\frac{1}{\delta}-A-DK\ln\left(\frac{\gamma}{\gamma^*}\right)\right] \tag{2.32}$$

where

$$\gamma\equiv\frac{u_\tau}{KU_1} \tag{2.33}$$

$$\gamma^*=\frac{u_\tau}{KU_1} \tag{2.34}$$

$$D\equiv\frac{\sqrt{2}\Delta}{2.303} \tag{2.35}$$

Dependence of γ on position x (distance from the edge of the plate) is found using the momentum balance equation for boundary layer. Reynolds number is defined as

$$Re_x\equiv\frac{U_1x}{\nu} \tag{2.36}$$

and carrying out some differentiation gives

$$-\frac{\gamma}{\Re_x}\frac{1}{\gamma^2}\exp\left[\frac{1}{\gamma}-A-DK\ln\left(\frac{\gamma}{\gamma^*}\right)\right][I_1-(I_2-DKI_1)\gamma+(I_2-DKI_2)]=K^3\gamma^2 \tag{2.37}$$

where I_1 and I_2 are

$$I_1 = 1 - \exp\left(-\frac{1}{\gamma}\right)(\gamma^{-1}+1) \tag{2.38}$$

$$I_2 = 2 - \exp\left(-\frac{1}{\gamma}\right)(\gamma^{-2}+2\gamma_{-1}+2) \tag{2.39}$$

Momentum thickness is found as

$$\theta = e^{-A}\frac{\nu}{KU_1}\int_0^z e^{z'}(z'\gamma^*)^{DK}\left[I_1 - \frac{I_2 - DKI_1}{z'} + \frac{I_2 - DKI_2}{(z')^2}\right]dz' \tag{2.40}$$

The momentum thickness found is related to the coefficient of surface friction.

$$C_f(x) = \frac{2\theta(x)}{x} \tag{2.41}$$

Detailed work can be found in literature [19].

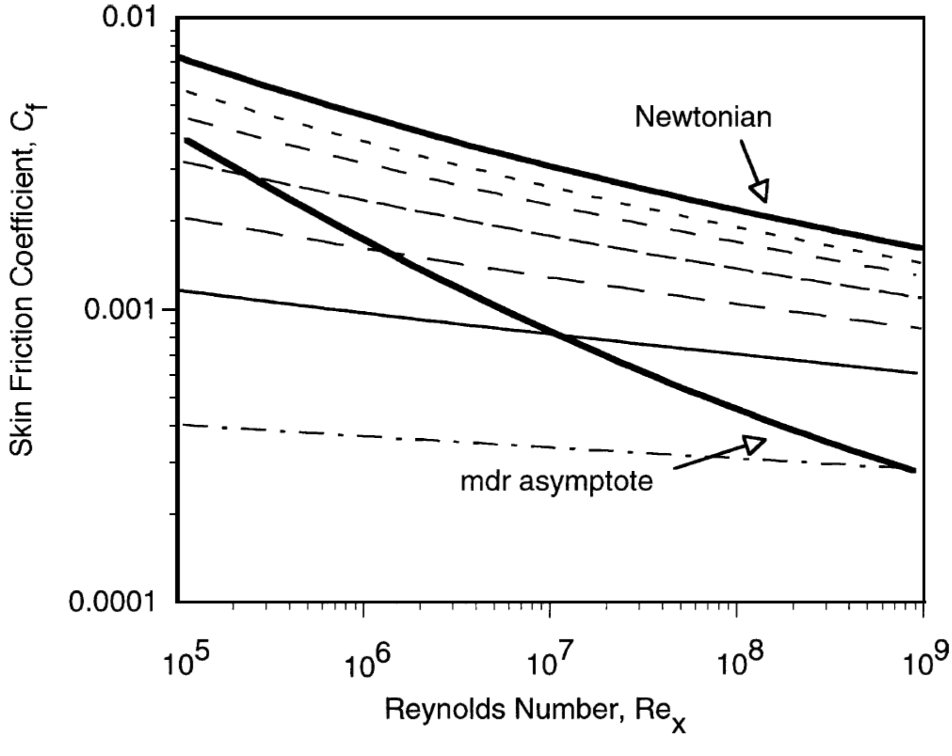

Figure 2.8. Skin friction coefficient vs. Reynolds number for MDR, Newtonian and Non-newtonian cases [19]

3. COMPUTATIONAL TOOLS

Computational Fluid Dynamics (CFD) is a computational tool that makes possible to simulate real environments involving fluid mechanics and heat transfer. The abilities of CFD are very complicated and it spans a wide area of application. It also predicts mass transfer (such as dissolution), phase change(such as boiling), chemical reaction (such as combustion) and mechanical movement(such as impellers).

CFD spans a wide range of industrial and non-industrial application areas.Some examples are

- aerodynamics of aircraft and vehicles: lift and drag
- hydrodynamics of ships
- power plant: combustion in internal combustion engines and gas turbines
- turbomachinery: flows inside rotating passages, diffusers etc.
- electrical and electronic engineering: cooling of equipment including microcircuits
- chemical process engineering: mixing and separation, polymer moulding
- external and internal environment of buildings: wind loading and heating
- marine engineering: loads on off-shore structures
- environmental engineering: distribution of pollutants and effluents
- hydrology and oceanography: flows in rivers, estuaries, oceans
- meteorology: weather prediction
- biomedical engineering: blood flows through arteries and veins

The advantage of the CFD is mostly its cost. Compared with an experimental facility CFD tools provide approximately equivalent accuracy for a much lower cost. Besides, it enables to study systems that can not be easily modeled where it is very hard to perform controlled experiments or measure physical quantities. In addition, it is preferable in studying safety assessment or hazardous conditions. It also provides practically unlimited level of detail of results [17].

3.1. Governing Equations of Fluid Dynamics

CFD uses the fluid dynamics equations and the governing equations of fluid motion are derived from the conservation laws of physics. The mass of a fluid obeys the law of conservation of mass. The rate of change of momentum is equal to the sum of forces on a fluid element which is Newton's second law. The first law of thermodynamics is applied by setting the rate of change of energy equal to the sum of the rate of heat addition to and the rate of work done on a fluid element [17].

According to the conservation of mass, the rate of increase of mass in fluid element is set equal to the net rate of flow of mass into fluid element. This can be expressed in differential form with the Equation 3.1 or in more compact vector notation with Equation 3.2.

$$\frac{\partial \rho}{\partial t} + \frac{\partial(\rho u)}{\partial x} + \frac{\partial(\rho v)}{\partial y} + \frac{\partial(\rho w)}{\partial z} = 0 \tag{3.1}$$

$$\frac{\partial \rho}{\partial t} + div(\rho \mathbf{u}) = 0 \tag{3.2}$$

Assuming the rates of increase of x, y and z momentum per unit volume of a fluid particle are $\rho\frac{Du}{Dt}$, $\rho\frac{Dv}{Dt}$ and $\rho\frac{Dw}{Dt}$ respectively, the x-component of momentum equation is derived by setting the rate of change of x-momentum equal to the addition of the net force in in x-direction on the element due to stresses with the rate of increases of x-momentum due to sources (S_{Mx} represents body forces, in literature it is also used as ρg_x). The y and z components of the momentum are shown in Equations 3.3b and 3.3c respectively.

$$\rho\frac{Du}{Dt} = \frac{\partial(-p+\tau_{xx})}{\partial x} + \frac{\partial \tau_{yx}}{\partial y} + \frac{\partial \tau_{zx}}{\partial z} + S_{Mx} \tag{3.3a}$$

$$\rho\frac{Dv}{Dt} = \frac{\partial \tau_{xy}}{\partial x} + \frac{\partial(-p+\tau_{yy})}{\partial y} + \frac{\partial \tau_{zy}}{\partial z} + S_{My} \tag{3.3b}$$

$$\rho\frac{Dw}{Dt} = \frac{\partial \tau_{xz}}{\partial x} + \frac{\partial \tau_{yz}}{\partial y} + \frac{\partial(-p+\tau_{zz})}{\partial z} + S_{Mz} \tag{3.3c}$$

From the first law of thermodynamics the energy equation is derived. The energy equation (Equation 3.4) states that the rate of change of energy of a fluid particle ($\rho\frac{DE}{Dt}$ per unit volume) is equal to the net rate of heat addition , $div(k\ grad\ T)$, plus the net rate of work done on the particle and the rate of change of energy due to sources (S_E).

$$\begin{aligned}\rho\frac{DE}{Dt} &= -div(\rho\mathbf{u}) + [\frac{\partial(u\tau_{xx})}{\partial x} + \frac{\partial(u\tau_{yx})}{\partial y} + \frac{\partial(u\tau_{zx})}{\partial z} + \frac{\partial(v\tau_{xy})}{\partial x} + \frac{\partial(v\tau_{yy})}{\partial y} + \\ &\quad \frac{\partial(u\tau_{zy})}{\partial z} + \frac{\partial(w\tau_{xz})}{\partial z} + \frac{\partial(w\tau_{yz})}{\partial z} + \frac{\partial(w\tau_{zz})}{\partial z}] + div(k\ grad\ T) + S_E \qquad (3.4)\end{aligned}$$

3.1.1. Navier-Stokes Equations

Since the governing equations contain viscous stress components (τ_{ij}) a useful form is obtained by modeling viscous stresses. In most flows the viscous stresses can be expressed as functions of the local deformation rate or strain rate. In a newtonian flow the viscous stresses are proportional to the rates of deformation. The Newton's law of viscosity which is three dimensional involves two constants of proportionality. In order to relate stresses to deformations, the dynamic viscosity (μ) and to relate stresses to the volumetric deformation ($div\ \mathbf{u}$), the second dynamic viscosity (λ) is used. Among the nine viscous stress components (Equation 3.5) only six of them are independent since the opposite shear stresses in the same plane are equal to each other. The volumetric deformation is equal to the mass conservation equation and is equal to zero in liquids since they are incompressible [17].

$$\tau_{xx} = 2\mu\frac{\partial u}{\partial x} + \lambda\ div\ \mathbf{u} \quad \tau_{yy} = 2\mu\frac{\partial v}{\partial y} + \lambda\ div\ \mathbf{u} \quad \tau_{zz} = 2\mu\frac{\partial w}{\partial z} + \lambda\ div\ \mathbf{u}$$

$$\tau_{xy} = \tau_{yx} = \mu\left(\frac{\partial u}{\partial y} + \frac{\partial v}{\partial x}\right), \tau_{xz} = \tau_{zx} = \mu\left(\frac{\partial u}{\partial z} + \frac{\partial w}{\partial x}\right), \tau_{yz} = \tau_{zy} = \mu\left(\frac{\partial v}{\partial z} + \frac{\partial w}{\partial y}\right) \quad (3.5)$$

Substitution of the shear stresses in Equation 3.5 into Equations 3.3a, 3.3b and 3.3c gives the Navier-Stokes equations. It is maybe just a coincidence that two scientists derived the equations independently so their names are given for the equations.

$$\begin{aligned}\rho\frac{Du}{Dt} &= -\frac{\partial p}{\partial x} + \frac{\partial}{\partial x}\left[2\mu\frac{\partial u}{\partial x} + \lambda\, div\, \mathbf{u}\right] + \frac{\partial}{\partial y}\left[\mu\left(\frac{\partial u}{\partial y} + \frac{\partial v}{\partial x}\right)\right] \\ &\quad + \frac{\partial}{\partial z}\left[\mu\left(\frac{\partial u}{\partial z} + \frac{\partial w}{\partial x}\right)\right] + S_{Mx} \end{aligned} \tag{3.6a}$$

$$\begin{aligned}\rho\frac{Dv}{Dt} &= -\frac{\partial p}{\partial y} + \frac{\partial}{\partial x}\left[\mu\left(\frac{\partial u}{\partial y} + \frac{\partial v}{\partial x}\right)\right] + \frac{\partial}{\partial y}\left[2\mu\frac{\partial v}{\partial y} + \lambda\, div\, \mathbf{u}\right] \\ &\quad + \frac{\partial}{\partial z}\left[\mu\left(\frac{\partial v}{\partial z} + \frac{\partial w}{\partial y}\right)\right] + S_{My} \end{aligned} \tag{3.6b}$$

$$\begin{aligned}\rho\frac{Dw}{Dt} &= -\frac{\partial p}{\partial z} + \frac{\partial}{\partial x}\left[\mu\left(\frac{\partial u}{\partial z} + \frac{\partial w}{\partial x}\right)\right] + \frac{\partial}{\partial y}\left[\mu\left(\frac{\partial v}{\partial z} + \frac{\partial w}{\partial y}\right)\right] \\ &\quad + \frac{\partial}{\partial x}\left[2\mu\frac{\partial w}{\partial z} + \lambda\, div\, \mathbf{u}\right] + S_{Mz} \end{aligned} \tag{3.6c}$$

3.1.2. General Transport Equations

The behavior of a general fluid property ϕ in a fluid element can be expressed by setting the rate of increase of ϕ plus the net rate of flow of ϕ out of fluid element equal to the rate of increase of ϕ due to diffusion plus rate of increase of ϕ due to sources. It is shown in below for a control volume.

$$\begin{pmatrix}\text{Rate of}\\ \text{increase}\\ \text{of } \phi\\ \ \end{pmatrix} + \begin{pmatrix}\text{Net rate of}\\ \text{decrease of } \phi \text{ due}\\ \text{to convection across}\\ \text{the boundaries}\end{pmatrix} = \begin{pmatrix}\text{Rate of increase}\\ \text{of } \phi \text{ due to}\\ \text{diffusion across}\\ \text{the boundaries}\end{pmatrix} + \begin{pmatrix}\text{Net rate}\\ \text{of creation}\\ \text{of } \phi\\ \ \end{pmatrix}$$

The most general form of the transport equation is Equation 3.7. Since it is a time dependent derivation all the terms include an integration over a small time period of δt. For the steady state, Equation 3.8, time integrations and the rate of change term drop from the Equation 3.7 [17].

$$\begin{aligned}&\int_{\Delta t}\int_{A}\mathbf{n}.(\rho\phi\mathbf{u})dA\,dt+\int_{\Delta t}\frac{\partial}{\partial t}\left(\int_{CV}(\rho\phi)dV\right)\\ =&\int_{\Delta t}\int_{CV}S_{\phi}dV\,dt+\int_{\Delta t}\int_{A}\mathbf{n}.(\Gamma_{\phi}\ grad\ \phi)dA\,dt\end{aligned}\tag{3.7}$$

$$\int_{A}\mathbf{n}.(\rho\phi\mathbf{u})dA=\int_{A}\mathbf{n}.(\Gamma\ grad\ \phi)dA+\int_{CV}S_{\phi}dV\tag{3.8}$$

3.2. Fluent

Fluent is a computer program that is designed for modeling fluid flow and heat transfer in complex geometries. It is written in C computer language.

The programs basic operation chart is shown in Figure 3.1. Fluent is capable of importing different mesh (grid) file types but it generally uses the mesh files generated with Gambit. The post-processing module is embedded in Fluent and it can show the results both on grid and as plots. The results can also be exported to other post-processor programs. Basically, Fluent has the following modeling capabilities [20]: 2D planar, 2D axisymmetric, 2D axisymmetric with swirl (rotationally symmetric), and 3D flows ; quadrilateral, triangular, hexahedral (brick), tetrahedral, prism (wedge), pyramid, and mixed element meshes; inviscid, laminar, and turbulent flows; steady-state or transient flows; heat transfer, including forced, natural, and mixed convection, conjugate (solid/fluid) heat transfer and radiation. When a problem is being solved

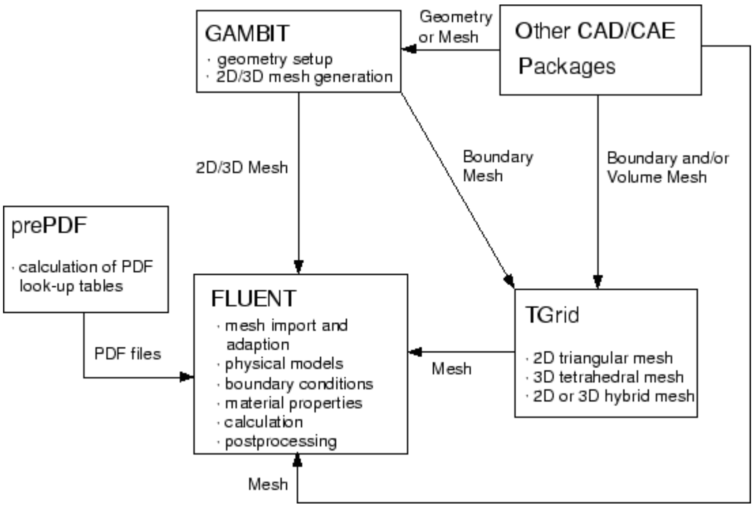

Figure 3.1. Basic program structure [20]

Table 3.1. The procedures of problem solving in Fluent

1.	Create the model geometry and grid
2.	Start the appropriate solver for 2D or 3D modeling
3.	Import the grid
4.	Check the grid
5.	Select the solver formulation
6.	Choose the basic equations to be solved
7.	Specify material properties
8.	Specify the boundary conditions
9.	Adjust the solution control parameters
10.	Initialize the flow field
11.	Calculate a solution
12.	Examine the results
13.	Save the results
14.	If necessary, refine the grid or consider revisions to the model

in Fluent, after the model geometry and the grid is created, the appropriate solver for 2D or 3D modeling is started. Grid is imported and checked. The appropriate solver formulation is selected (segregated, coupled etc.). The basic equations to be solved are chosen, laminar or turbulent (or inviscid), chemical species or reaction, heat transfer models, etc. Material properties and the boundary conditions are specified. Then the solution control parameters are adjusted. After the flow field is initialized for a given number of iterations looking at the residual values and related with the determined convergence criteria a solution is calculated. The results are examined through the program's post processing capabilities.

For all flows, Fluent solves conservation equations for mass 3.1 and momentum 3.3a, 3.3b, 3.3c. For flows involving heat transfer or compressibility, an additional equation for energy conservation is solved. For flows involving species mixing or reactions, a species conservation-equation is solved or, if the non-premixed combustion model is used, conservation equations for the mixture fraction and its variance are solved. Additional transport equations are also solved when the flow is turbulent [20].

3.3. Gambit

Gambit is a software package designed for building geometries and grids to use in computational fluid dynamics. The generated grids can also be used in other engineering applications. The user inputs the commands through its graphical user interface (GUI). The Gambit GUI makes the basic steps of building, meshing, and assigning zone types to a model [20].

In order to mesh a geometry, first the geometry is created. Then the edges of the geometry are meshed. This is not necessary for the rest of the mesh process but meshing edges yields closer results to the mesh desired. There are some considerations in edge meshing. The desired mesh can be uniform or concentrated on one side or in the middle of the edge. In uniform meshes the edge is divided into intervals with equal sizes but in non-uniform meshes the succeeding intervals are smaller or larger. In order to do this gambit uses grading schemes [20] which are successive ratio, first length, last length, first last ratio, last first ratio, exponent, bi-exponent and bell shaped.

For each of the non-symmetric grading schemes, gambit positions mesh nodes along the edge such that the ratio of any two succeeding interval lengths is constant.

$$\frac{l_{i+1}}{l_i} = R \tag{3.9}$$

where l_{i+1} and l_i are the lengths of intervals i and $i+1$, respectively, and R is a fixed value (Figure 3.2). For any number of intervals on the edge, the grading schemes differ from each other only with respect to the manner in which gambit determines the value of the interval length ratio, R.

After meshing the edges the faces can be meshed with an appropriate meshing technique. To build structured grids quad-map meshing scheme is used. However, meshing scheme has some restrictions. For the face to be mappable (Figure 3.3), the number of mesh intervals on edge 2 must be equal to that on edge 4 and also same is required for edge 1 and edge 3. There should be only four main edges to use

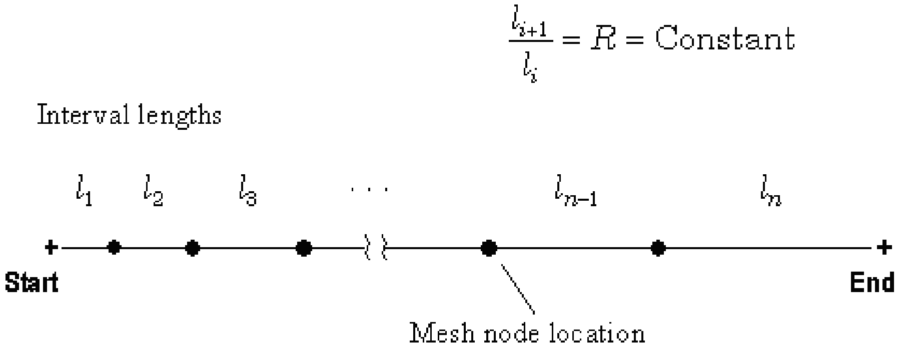

Figure 3.2. Edge mesh grading parameters [20]

map meshing scheme otherwise the grid can not be generated. However, in complex geometries there are more than four sometimes even more number of edges. This makes mapping scheme unpossible but the edges are introduced to Fluent in such a way that Fluent recognizes only four edges. This is done by setting the points on the geometry as side, reversal or ending point.

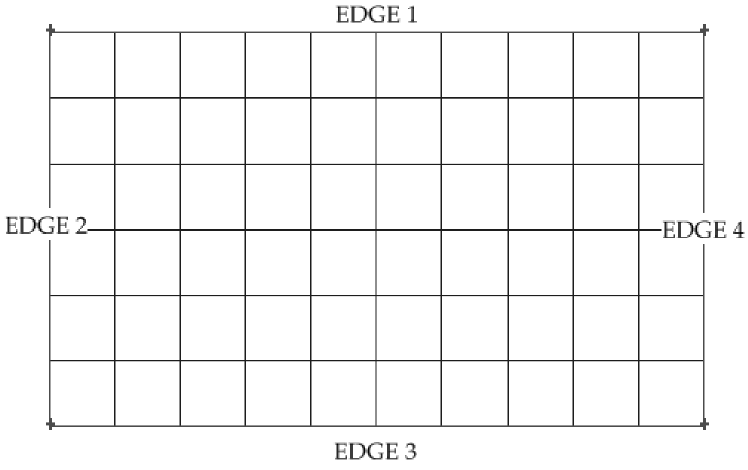

Figure 3.3. Illustration of quad-map meshing scheme

3.3.1. Near-Wall Grid Considerations

In order to obtain successful computations grid generation needs some consideration. In addition, half of the time is spent on grid generation in numerical simulations. If the simulation of a turbulent flow is the case, then turbulence quantities should be properly resolved to achieve high accuracy, since the results for the turbulent flow are susceptible to grid dependency. Therefore, it is recommended to resolve the regions with fine meshes, where the mean flow changes rapidly.

The near wall region has critical importance in turbulent flows since the boundary layer theory is applicable on that region. Furthermore, depending on the Reynolds number the boundary layer is usually very thin. Therefore, the distance from the wall at the wall-adjacent cells must be determined by considering the range over which the log-law is valid. The distance is usually measured in the wall unit, y^+ $(= \rho u_\tau y/\mu)$ or y^*. As the Reynolds number increases, the upper bound of the log-layer tends to increase so y^+values that are too large are not desirable [20].

It is important to have at least a few cells inside the boundary layer. If the enhanced wall treatment will be used the the y^+ value at the wall adjacent cell should be equal to at least 1. However, $y^+ < 4$ or 5 is also acceptable as long as it is well inside the viscous layer. Besides, at least 10 cells should be placed within the viscosity affected near wall region.

4. NUMERICAL STUDIES OF VALIDATION

4.1. Numerical Simulation of a Flow Around a Hydrofoil

In order to validate the correct use of Fluent, the numerical simulation of an experimental research conducted by Bourgoyne et. al. [21] was performed. The experiments were conducted at US Navy's W. B. Morgan Large Cavitation Channel with a two-dimensional hydrofoil spanning the test section ($13m$ x $0.5m$) at flow speeds of 0.5 to 18.3 m/s.

The foil has a cross section of a generic naval propeller of thickness (t) and camber (f). The shape is a NACA-16 ($t/C = 0.08, f/C = 0.032$) with two modifications (Figure 4.1). First, the bottom (pressure side) of the foil is flat after 28% of chord. Second, the foil terminates with an anti-singing trailing edge which is typical in naval propellers. Compared to the NACA-16, the trailing edge tapers more slowly at first then near 97% chord turns down and terminate at an angle of 44^0. The trailing edge is ground to 0.397 mm. The hydrofoil was CNC machined from a solid Ni-Al Bronze casting and polished to a surface roughness of 0.25 μm or less [21].

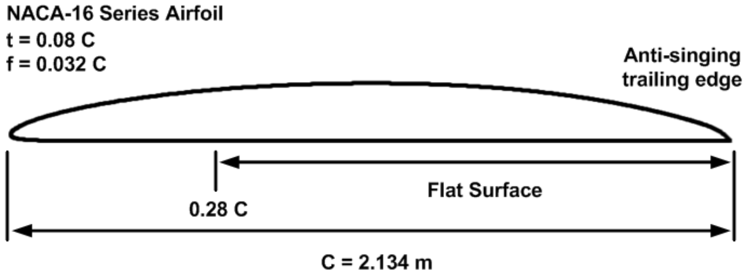

Figure 4.1. The two-dimensional hydrofoil geometry used by Bourgoyne et. al. (Adapted from [21])

For the numerical simulations two types of grids were used, structured mesh and hybrid mesh [4] . The boundary conditions and the geometry (C-type, Figure 4.2) were the same for both of them. In the upstream of the flow and above and below of the hydrofoil, velocity inlet boundary conditions were applied. For the downstream of flow, the flow was assumed fully developed, therefore an outflow boundary condition was applied. The suction and pressure surfaces of the hydrofoil were defined as no-slip wall boundaries.

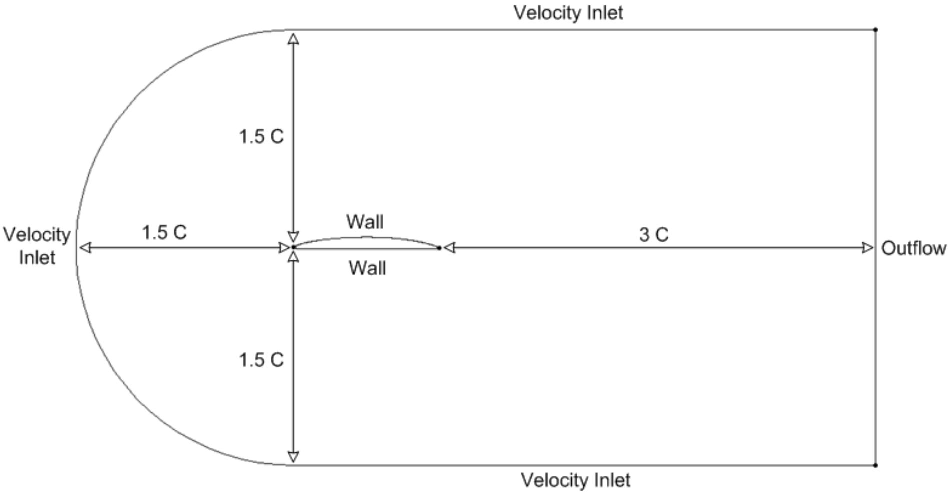

Figure 4.2. The dimensions and boundary conditions of the computational domain

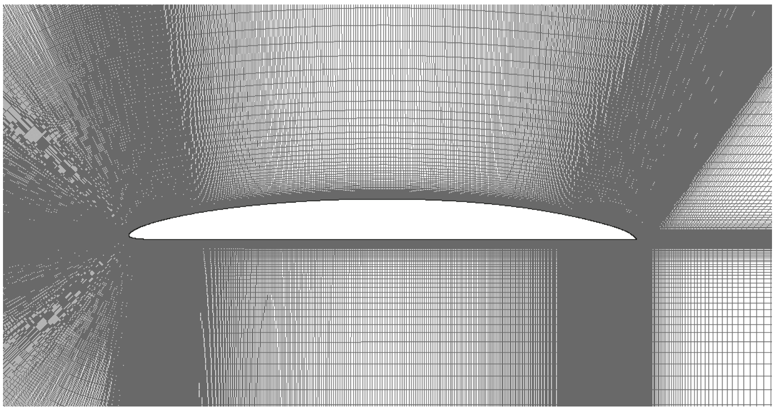

Figure 4.3. Detailed view for structured mesh

The hybrid mesh (Figure 4.4) consists of a boundary layer[5] mesh with an initial size of 2.134×10^{-6} m. There are 2000 nodes on each side of the hydrofoil. Since the

---

[4] Hybrid mesh is a combination of structured and unstructured meshes.

[5] Boundary layer is a structured mesh in Gambit that resembles the body fixed grids. It is attached to the boundary and expands outwards up to 20 cells.

enhanced wall treatment was used the mesh should be fine. After the boundary layer, a quadrilateral structured mesh paves the inside of a O-type geometry surrounding the hydrofoil. The gross geometry is a C-type and the transition from O-type to C-type was achieved with structured grid elements. It consists of 331145 cells and 333827 nodes. The grid has an average y^+ value of 0.1614 for 3 m/s and 0.3055 for 6 m/s.

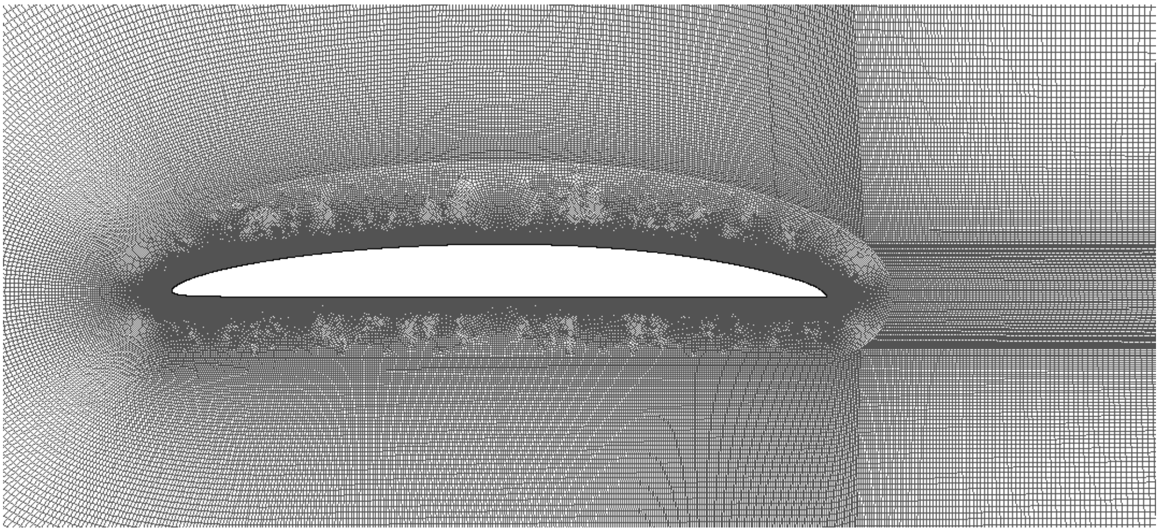

Figure 4.4. Detailed view for hybrid mesh

The structured C-type mesh (Figure 4.6)consists of $100 \times 3600 = 360000$ cells and 363500 nodes. The y^+ values are 1.02 and 3.41 for $3m/s$ and $6m/s$ respectively.

4.1.1. The Numerical Simulations

In order to solve the spatially averaged Navier-Stokes equations, finite volume method was used. The pressure velocity coupling was accomplished with SIMPLE technique. The second order-upwind scheme was used for convection and diffusion terms.

The turbulent models used were realizable and standard k-ϵ models. The turbulence intensity of the water tunnel was found as 0.1% from the literature. The length scale of the model was determined from the chord length (l=0.01C). However, during computations it is seen that the turbulent parameters are just initial conditions that any value of the initial parameters of the turbulence yields the same result. The only difference is the computing time. Therefore, again it is seen that guessing the initial conditions is an important part of the CFD.

The gravitational effects were also considered together with the buoyancy effects. The computation time did not change sensibly. In addition, it was seen that nothing changed with the contribution of gravity. This could be since the depth is not so high.

The local surface friction coefficient (C_f) expresses the behavior of the shear stresses on the surface. The point where the C_f is zero, is an indication for the full separation. In the experiments, boundary layer separation was determined to occur between 95.75%C and 97.50%C on the suction surface of the hydrofoil [21]. However, in Figures 1 and 2 it is seen that the separation points are not between this interval. Different from the solutions in [22] there are fluctuations in 97%C in current study. This can be possibly explained by a discontinuity in the geometry at that location since the geometry is not precisely defined in the report of the experiment. However, according to Mulvany et. al. [22] the separation point can be determined as a point where a sharp decrease follows some fluctuations ending at zero. Therefore, the separation point for the numerical simulations are in the interval determined with the experiment which is 96%. Moreover, both of the turbulence models predict the same value for the separation. Besides, it is nearly same for the two test speeds.

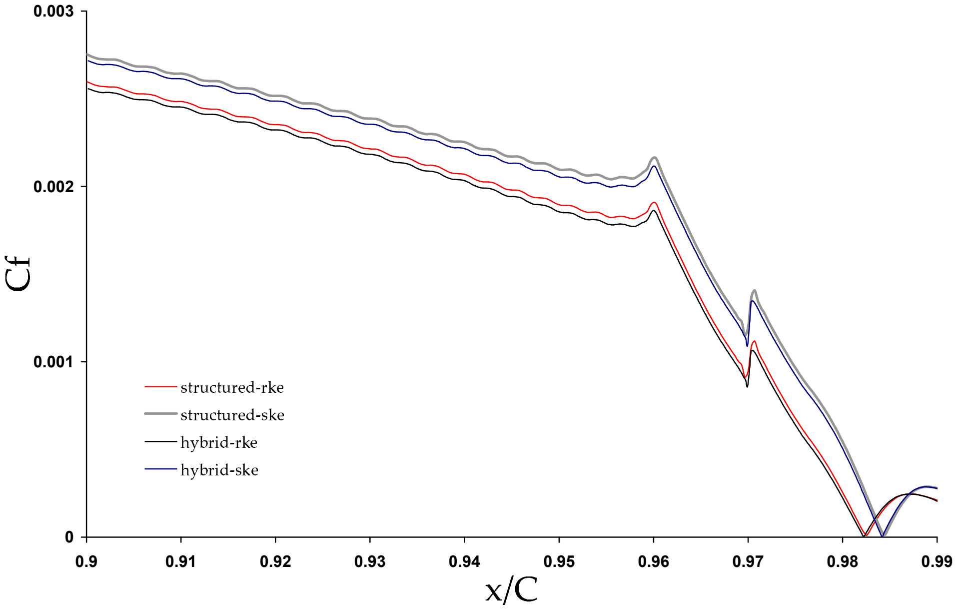

Figure 4.5. Distribution of skin-friction coefficient on the suction surface at the trailing edge ($U_\infty = 3m/s$)

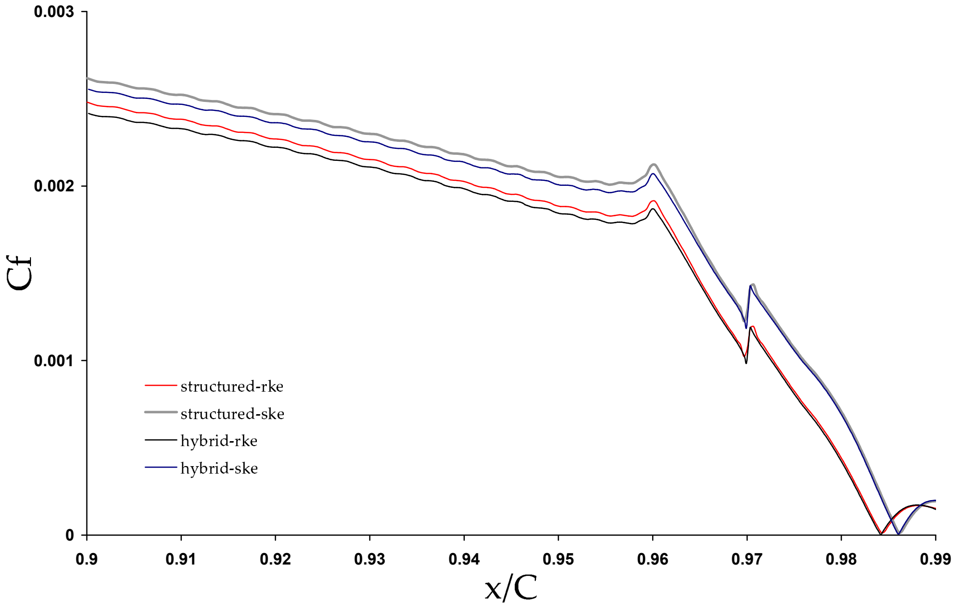

Figure 4.6. Distribution of skin-friction coefficient on the suction surface at the trailing edge ($U_\infty = 6m/s$)

The local pressure coefficients provide an approximate view of pressure distribution on surfaces. Therefore, they are useful in prediction of the drag and lift on a body. In the current simulation, the C_p values are close to experimental ones (Figures 4.7 and 4.8). The realizable k-ϵ model predicts the results better. The standard k-ϵ model has also close values and a similar profile but a little shifted down. The profile of the C_p diagram resembles the shape of the body shape. Therefore, it can be concluded that geometry has an influence on pressure distribution.

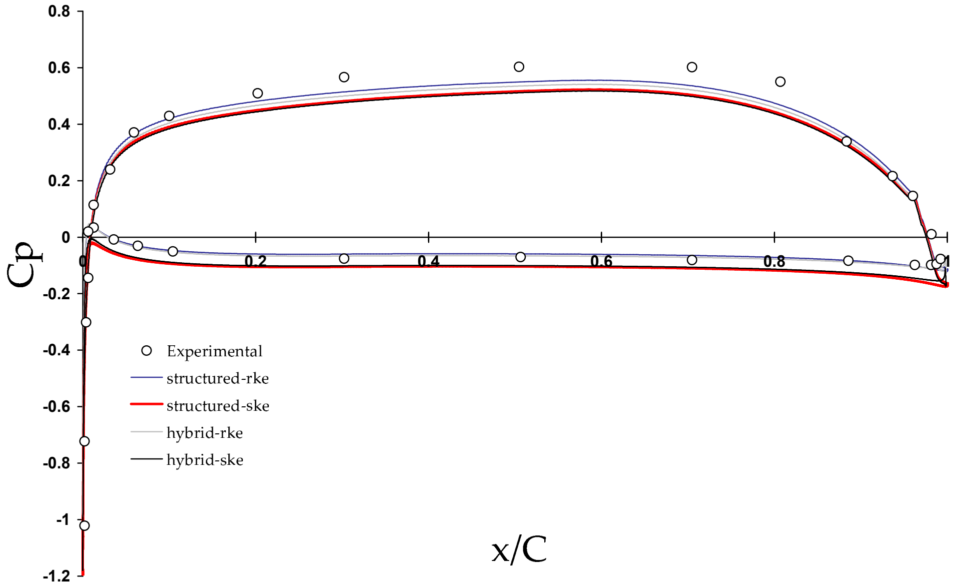

Figure 4.7. Distribution of pressure coefficient at the surface(U_∞ = 3m/s)

The predicted lift and drag coefficients are in Tables 4.1 and 4.2. Taking a look at the experimental values for 3 m/s and 6 m/s, it is seen that velocity has an effect on drag coefficients although the drag coefficient is usually seen as a dimensionless parameter that describes the behavior of resistance in a flow. It can be an indirect effect of velocity caused probably by turbulence. Therefore, at high turbulence or at high Reynolds numbers it is better to estimate the drag force rather than trusting on an estimation of drag using drag coefficient value.

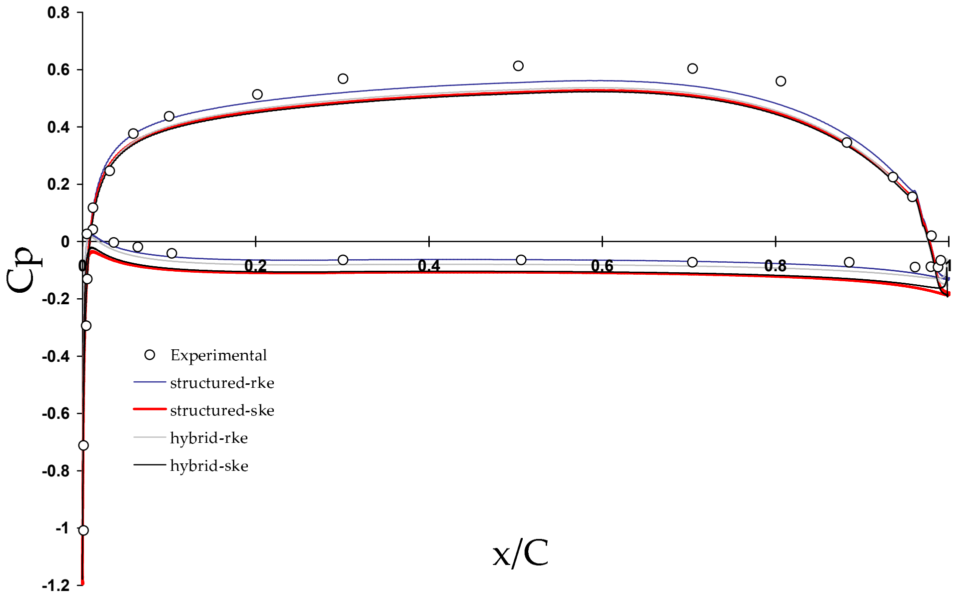

Figure 4.8. Distribution of pressure coefficient at the surface of the hydrofoil (U_∞ = 6m/s)

Table 4.1. Numerical solutions at 3 m/s for pressure derived lift and drag coefficients

	Drag Force	Lift force	C_D	C_L	% Error C_D	% Error C_L
Experimental	-	-	0.0027	0.552	-	-
Structured RKE	25.66 N	4863 N	0.00268	0.5086	0.74%	7.86%
Structured SKE	34.57 N	5021 N	0.00362	0.5252	34%	4.86%
Hybrid RKE	25.53 N	4770 N	0.00267	0.4989	1.1%	9.61%
Hybrid SKE	33.47 N	4914 N	0.0035	0.5139	29.6%	6.9%

Table 4.2. Numerical solutions at 6 m/s for pressure derived lift and drag coefficients

	Drag Force	Lift force	C_D	C_L	% Error C_D	% Error C_L
Experimental	-	-	0.00258	0.5486	-	-
Structured RKE	98.76 N	19947 N	0.00258	0.5216	0%	4.92%
Structured SKE	134.8 N	20509 N	0.00353	0.5363	36.8%	2.24%
Hybrid RKE	96.33 N	19553 N	0.00252	0.5113	2.38%	6.8%
Hybrid SKE	127.69 N	20089 N	0.00334	0.5253	29.46%	4.25%

The pressure derived drag coefficients are in close agreement with the experimental values for realizable k-ϵ model. The standard k-ϵ model predicts the lift coefficient better than the realizable model. This is possibly since the wall effects of the water tunnel were neglected. The realizable k-ϵ model is better in prediction of the drag than the standard model. Therefore, for the rest of the work only realizable k-ϵ model with enhanced wall treatment was used.

Table 4.3. Drag and lift coefficients at 3 m/s for RKE using different wall functions

	C_D	C_L	% Error C_D	% Error C_L
Standard Wall Functions	0.003096	0.4622	14.66%	16.27%
Non-Equilibrium Wall Functions	0.003567	0.4335	32.11%	21.47%
Enhanced Wall Treatment	0.00267	0.4989	1.1%	9.61%

As a conclusion realizable k-ϵ model predicted closer results to the experimental observations. Another conclusion is about hybrid mesh which gives almost same results with the structured mesh. Besides, the hybrid mesh converged very fast in an order of 5000 iterations while the structured mesh reached the same residual values in approximately 50000 iterations. This is since the hybrid mesh resolves the critical regions better.

Another use of the hybrid mesh is the grid generation time. Structured meshes are hard to generate if the resolution is too fine. The skewness of the cells can cause troubles and highly skewed elements are not desired. In order to overcome these difficulties excessive amount of time must be spent. The unstructured meshes however, demand less time to build but they are computationally less efficient. The hybrid mesh, created from an unstructured mesh and a structured mesh using less amount of cells, best suits to applications where shapes are complicated. For the rest of the work hybrid mesh was used since it provides better efficiency in both grid generation and computation.

4.2. Study of the Axisymmetric Solver

In order to study the axisymmetric solver of Fluent, an experimental study conducted by Patel et. al was simulated. Axisymmetric bodies or bodies of revolution are geometries which are 360^0 symmetric around an axis. It was observed that 2D numerical simulation gives accurate results for a hydrofoil although it is in 3D space, likewise, for a solid body of revolution the 2D axisymmetric simulation should give realizable results.

The experiments were conducted in the largest closed-circuit wind tunnel of the Iowa institute of Hydraulic Research. Although the maximum speed affordable in the tunnel was in the order of 90 ft/sec, the experiments were conducted at a nominal speed of 40 ft/sec to minimize the influence of the vibration of the tunnel [23].

The test model (Figure 4.9) was a six to one prolate spheroid, 5 feet long and 10 inches in maximum diameter, which is a popular model used in axisymmetric model experiments. The complete geometry is given by:

$$\frac{r}{L} = \frac{1}{6}\left[\frac{x}{L}(0.9655 - \frac{x}{L}\right], \quad 0 < \frac{x}{L} < 0.9333$$

$$\frac{r}{L} = 0.4333\left(1 - \frac{x}{L}\right), \quad 0.9333 < \frac{x}{L} < 1.000$$

Since there was no LDA (Laser Doppler Anemometry) developed at the time the conventional methods (Hot-wire anemometry, pitot tube, single and cross wire) were used for the measurements.

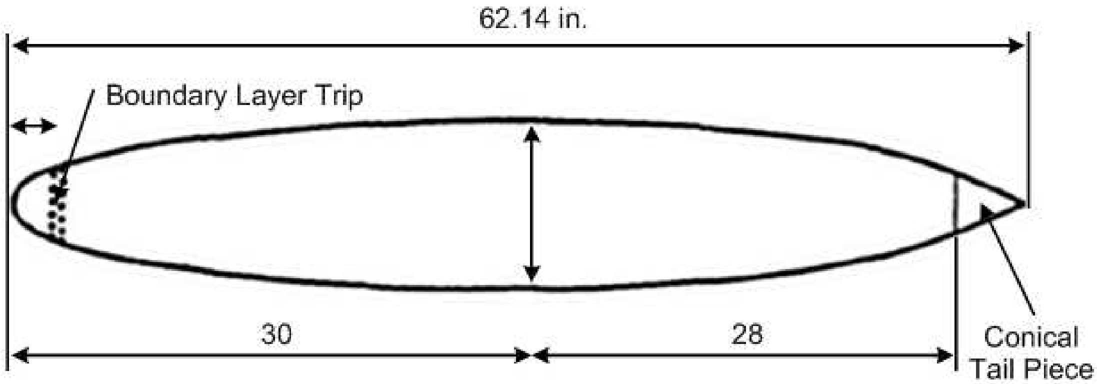

Figure 4.9. The prolate spheroid used in the experiment [23]

4.2.1. Numerical Simulation

The solution of the problem was achieved using axisymmetric equations. A half C-type structured grid (Figure 4.10) was generated using Gambit. It is in an order of 1900 × 100, 190000 cells and 192001 nodes. It has a y^+ value of 0.016. It was aimed to build the best grid that resembles a body fixed grid (Figures 4.11 and 4.12) and to reach this the grid lines was proposed to intersect at 90^0 or at a close angle with the surface of the body.

Finite volume method was used to solve the problem. The axisymmetric 2D model was chosen. In order to achieve better predictions termal effects were also included. The dependence of density on temperature was defined with ideal gas law. Second-order upwind scheme was used for convection and diffusion terms.

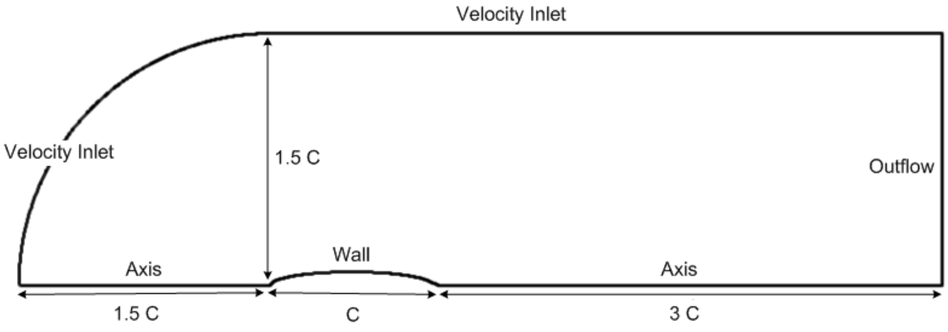

Figure 4.10. The geometry and the boundary conditions for the C-type (half) grid

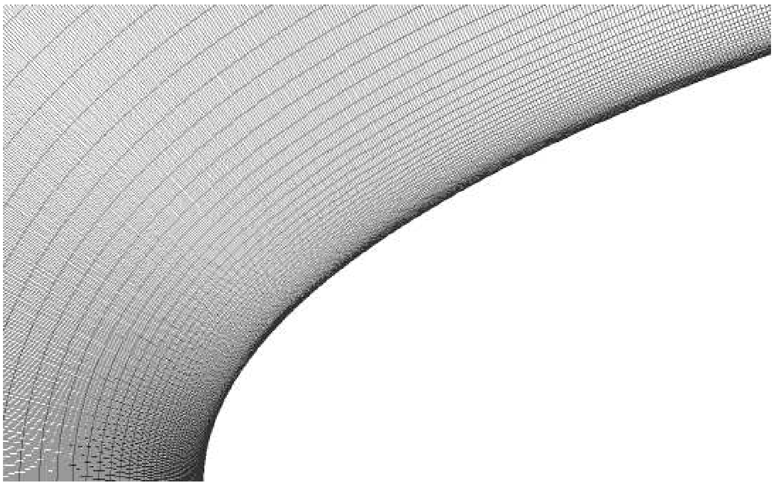

Figure 4.11. The geometry and the boundary conditions for the C-type (half) grid

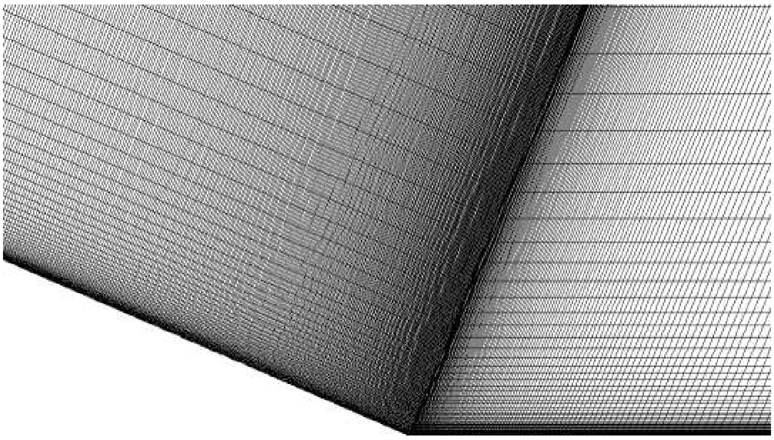

Figure 4.12. The geometry and the boundary conditions for the C-type (half) grid

In comparisons of the numerical values with the experimentally estimated values (Figures 4.13 and 4.14) it is clear that axisymmetric model can simulate a body of revolution. However, there is not a one to one correspondence between the numerical values and experimental values . This can emerge from the deficiency of measurement tools used in the experiment.

Although the computations were done in 2D space the iteration times are larger compared to the 2D plane geometry. This is is since axisymmetric model includes extra terms including conversions and these yield a larger computation time.

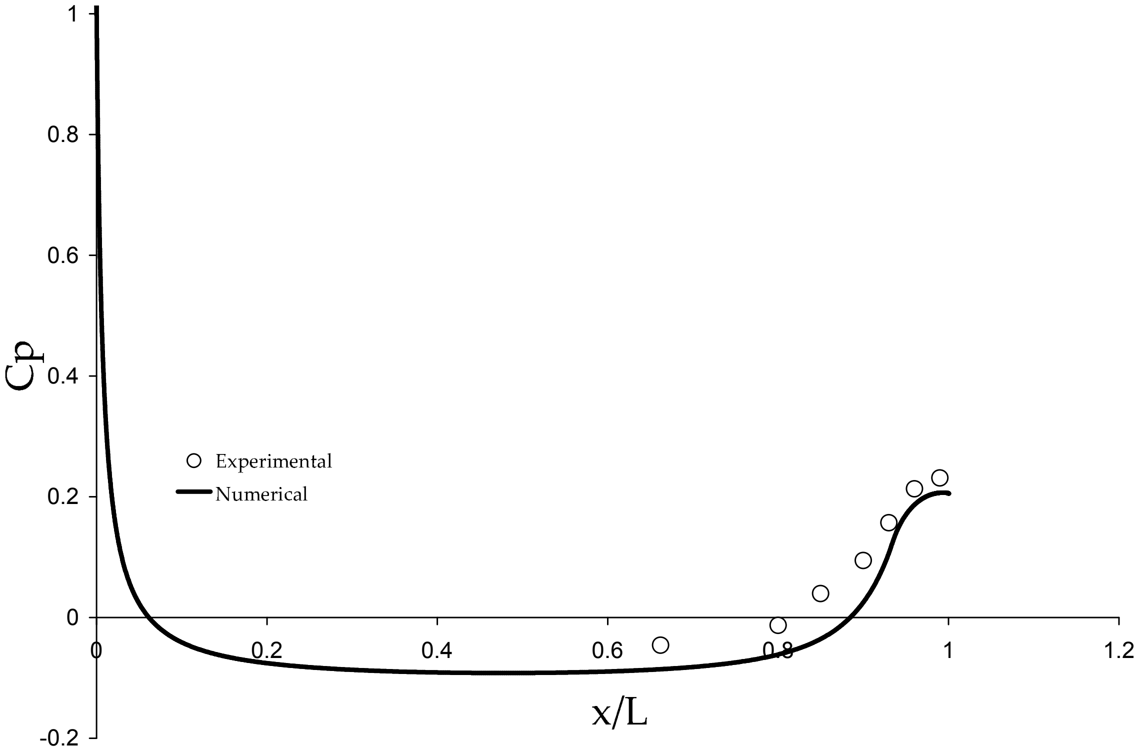

Figure 4.13. The comparison of the pressure coefficient values estimated numerically and experimentally

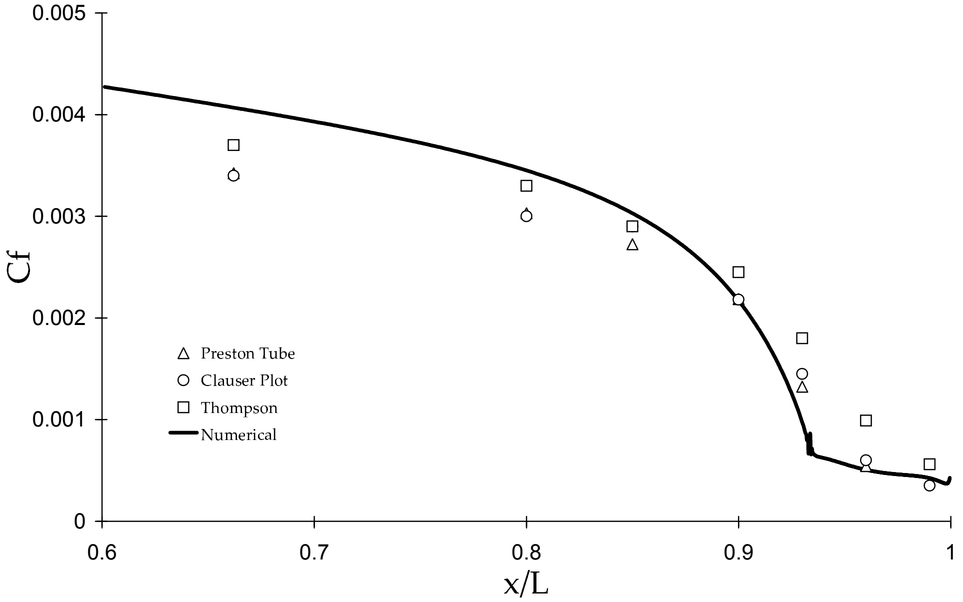

Figure 4.14. The comparison of the friction coefficient values estimated numerically and experimentally

5. DESIGN OF A TORPEDO

After the invention of the first torpedo (1866) the studies concentrated on raising the engine power. In external appearances all the torpedoes were almost same. The middle and tail sections were standard but the only difference was the nose shape of torpedoes. In 1883 a committee set up to examine various aspects of torpedo design. Tests were carried in order to understand the effect of nose shape on speed [4].

Up to that time the pointed nose was assumed the cleave the water best. However, Froude[6] claimed before (at the time he was not alive) that blunt head should show no disadvantage in speed performance and would allow much larger carriage. The trials were conducted using the Woolwich and Fiume models each fitted with blunt and pointed noses. The results of the tests opened a new page in the history of torpedo design, since the blunt nosed torpedoes had a full knot advantage over the pointed nosed version.

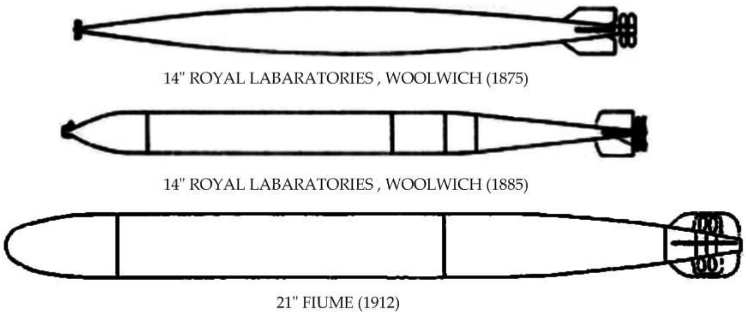

Figure 5.1. Evolution of the blunt nose torpedo [4]

From the viewpoint of body geometry, today's torpedoes are not much more distinct from the early torpedoes in history. Differently, the flat-nosed torpedo models were designed. Flat-nosed design has some advantages in some specific areas. Their stability characteristics are better since they have a flat nose and they can not maneuver so easily. When they are dropped from a plane or a helicopter the flat nose makes the diving of the torpedo easy since the torpedo does not change its direction much.

---

[6] Froude can be named as the greatest hydrodynamicist. He was a British civil engineer, mathematician and a naval architect. He pioneered the use of towing tanks for the study of ship design. He discovered a dimensionless group which made him still famous [15].

Moreover, acoustic devices are placed for homing systems if the front area is flat and large and all the acoustic torpedoes are flat-nosed. There may be more detailed explanations but they are not known publicly because of the secret nature of the military applications.

5.1. How to Design?

In the present study US Navy's Mark-50 [3] torpedo is taken as a reference. Mark-50 has a length of 112 inches (285 cm) and diameter of 12.74 inches (32.385 cm). Its top speed is around 40 knots (20.576 m/s) and its weight is 340 kg. It uses stored chemical energy propulsion system for the powering, it has an acoustic homing guidance and it can be launched from air vehicles and ships.

Using the dimensions of the real model initial criteria were set for the study. The width of the propeller was assumed 10 cm and a projectile geometry was drawn (Figure 5.2) which has a circular nose and a hybrid (ellipse-parabola) afterbody. This geometry was altered considering the basic steps of the hydrodynamic design.

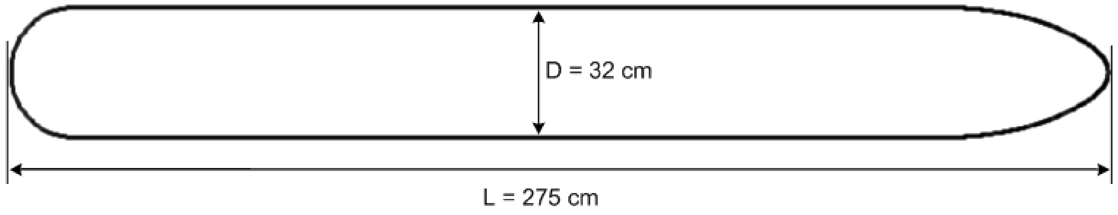

Figure 5.2. The geometrical details of the design

In order to yield the proposed effect of the solid-fluid interaction (lift, drag) for a certain object, there are some certain principles in designing the shape of the object. If the reduction of the drag is the case, then the shape should be streamlined. This can be done by predicting the flow field around the body which requires some experience of the external flow over the bodies.

Simply, if the geometry is a vertical flat plate, the drag force will be high because the streamlines do not cover the body. If the flat plate is connected to a cone from the back side, it will be easier for the streamlines to follow the surface of the body. Decreasing the slope of the cone will yield a better attachment of the streamlines to the surface but the increase of the length of the cone will raise frictional forces.

Unfortunately, comparisons do not yield explicit results, themselves. For the comparison of drag on a sphere and an ellipsoid, it can be said that the sphere is thicker and separation is unavoidable downstream of the flow. The separation probably occurs at a further location for the ellipsoid. However, at the stagnation point of the both geometries the pressure is the highest and the contribution of the pressure to the drag force is larger for an ellipsoid at that region. Moreover, the total surface area of the ellipsoid is greater which can possibly yield more frictional drag. To overcome these difficulties theoretical and experimental studies are used but CFD is the most popular and costly efficient solution.

5.1.1. The Grid and the Geometry

The initial geometry was determined throughout the considerations explained before. Since it is a body of revolution the drafts were drawn on 2D. The nose is chosen to be round with a circular diameter equal to the diameter of the axisymmetric body (16 cm). The circular geometry is appropriate since the slope of a circle is zero at the attachment points with axisymmetric body (Figure 5.2 may be illuminating). The afterbody was defined as a combination of an ellipse and a parabola (Figure 5.3).

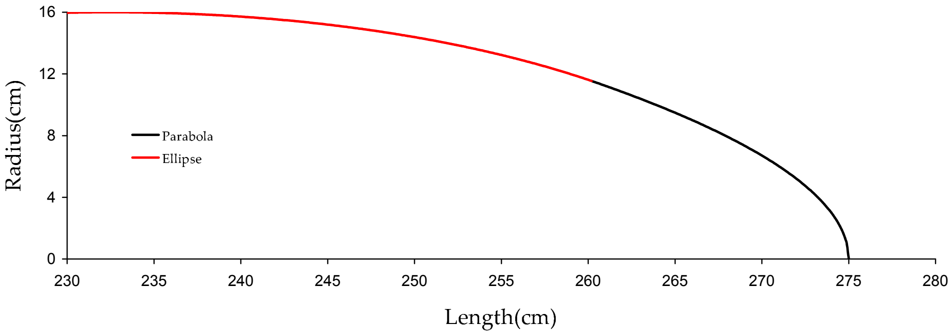

Figure 5.3. The geometrical detail of the afterbody of the torpedo

The grid dimensions were determined as seen in Figure 5.5. Likewise the previous numerical validations in the study, the inlet boundary condition was set 1.5 L away from the nose of the torpedo where L is the length of the torpedo. The upper bound was defined as symmetry boundary condition which is also used for far field conditions. There is no flow inlet or exit at the symmetry boundary condition so no initial conditions are given. The bottom line of the geometry was set to axis in order to solve axisymmetric flow equations. A hybrid grid was generated in order to resolve the near wall regions with high precision. The grid has 128212 cells and 129507 node points. The average wall y^+ was in the order of 0.1957. There were 1200 centrally symmetrical nodes on the wall boundary with a first-last ratio of 50 meaning that the last interval on the nose section is 50 times smaller than the interval in the middle of the wall boundary. This is done in order to resolve the critical regions at nose and wake with fine meshes.

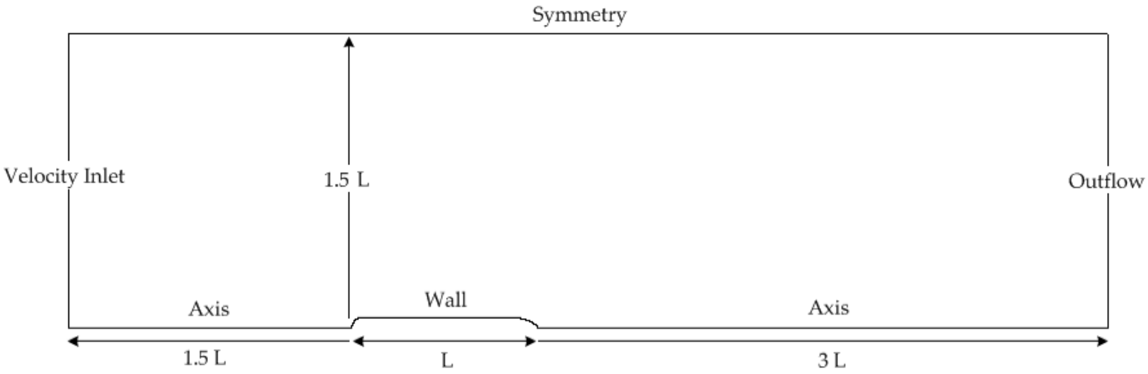

Figure 5.4. The geometry and the boundary conditions for the problem

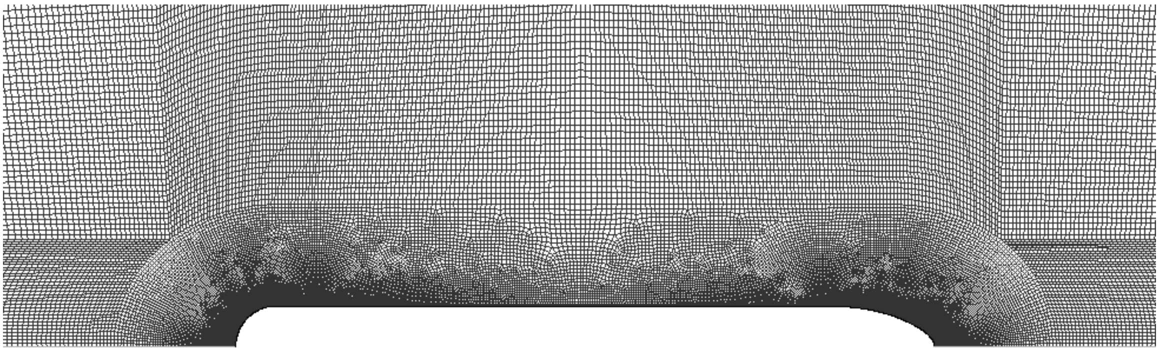

Figure 5.5. Magnified view of the hybrid grid around torpedo geometry

5.1.2. The Numerical Simulation

The segregated solution method was used to solve the steady state axisymmetric equations. The second-order upwind scheme was used for the turbulent diffusion and convection terms. The SIMPLE technique was applied in order to couple the pressure and the velocity. The turbulence model used was the realizable k-ϵ model. Near wall treatment was provided with enhanced wall treatment.

The initial conditions for the inlet boundary condition was 10 m/s inlet velocity. Since higher velocities demand finer meshes the comparisons of drag for different geometries can be accomplished at a reasonable speed. The turbulent parameters were estimated from turbulence intensity and the length scale as 0.1% for turbulence intensity and $l = 0.01 \times L$ for the length scale. As previously mentioned the initial parameters of turbulence affect only the convergence not the results. Besides, these gravitation and buoyancy effects were not taken into account and the properties of the water was defined at 20^0C. In addition, an angle of attack was not defined so it was assigned as 0.

The results were found to be 41.81 N for pressure drag force and 327.39 N for the friction drag force. The total drag was 369.2 N for the body of revolution (In axisymmetric models the results are multiplied with 2π within the solver). From the results it is clear that friction drag is dominant on axisymmetric and streamlined bodies. The ratio of friction drag to pressure drag is 7.83 which is very high.

5.2. Altering the Geometry

The results show how the friction drag is dominant on a torpedo body. However, this model is deficient to simulate a real torpedo but it gives a rough estimation of the drag forces. In order to find more realizable results a hydrodynamically efficient torpedo was designed through different steps.

First, an appropriate geometry for the nose section should be determined. The nose section is flat therefore it is connection with the wall of the torpedo can be made with basic geometries like ellipsoid and sphere which connect to the wall without disrupting the continuity.

However, the trouble of meshing is faced again and the use of hybrid mesh appears. Since hybrid mesh consists of an unstructured and a structured mesh it seems hard to build it. However, the grid generation was hard at the beginning. Once a grid was generated it was used for all geometries. The unstructured region of the hybrid mesh was divided into subregions and only the relavant subregion was remeshed (Figure 5.6). This provided great time saving and lead to the chance of simulating lots of models.

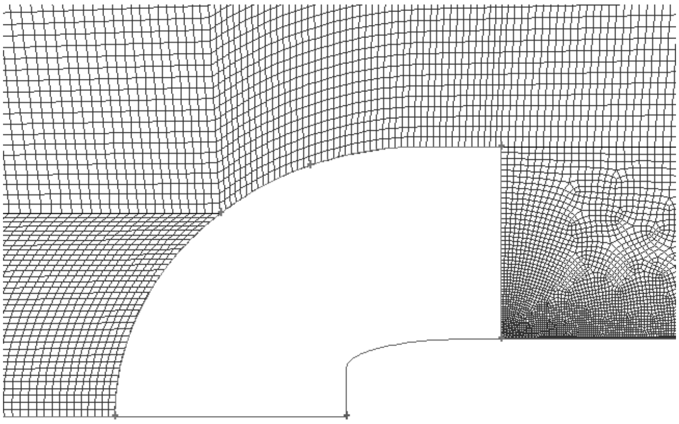

Figure 5.6. The empty region can be modified and meshed independent of the outside mesh

5.2.1. Spherical Nose Models

First, the spherical geometries were tested to find out the affect of flatness on the drag force. Five different geometries with different radii were constructed as seen in Figure 5.7. The radii of the circles were ascending from 16 cm to 4 cm with intervals of 2 cm. This was done in order to obtain a comparison of different flat areas and a result for the affect of flat area on the drag force. However, the flat area is not the only decisive parameter in drag force. The type of connection made with the upper wall is also critical. The results of the circular geometry study can only give a clue and a rough estimation for the next part of the study.

Testing the geometries with the same conditions in section 5.1.2, yielded the results in Table 5.1. As one can predict, with the decrease of the radius the drag force increased since the stagnation point was altered into an area rather than a point. The contribution of the pressure forces raised and it was reflected to the raise of coefficients of pressure drag. However, the share of pressure drag was low in total drag so total drag did not change significantly. Besides, the attitude of the friction drag was interesting. It raised at first then lowered. This was probably the cause of velocity profile which changed with the alteration of the geometry. Boundary layer was also affected from the changes and the change of the friction forces that are related with the boundary layer changed the friction drag.

Table 5.1. The results of spherical nose models

Model	Pressure Force	Friction Force	Total Force	C_{Dp}	C_{Df}	C_D
Circular-16	41.814 N	327.396 N	369.210 N	0.01042	0.08158	0.09200
Circular-12	46.176 N	328.107 N	374.283 N	0.01151	0.08176	0.09326
Circular-10	49.292 N	328.051 N	377.343 N	0.01228	0.08174	0.09403
Circular-8	53.717 N	327.462 N	381.179 N	0.01339	0.08160	0.09498
Circular-6	59.963 N	326.326 N	386.289 N	0.01494	0.08131	0.09625
Circular-4	72.860 N	325.377 N	398.237 N	0.01816	0.08108	0.09923

Circular-8 and Circular-6 are reasonable models. They have large flat areas and reasonable drag coefficients. Since there is not an exact data about the area of the flat part, by examining the results the flat area was decided to be as large as possible. The pressure drag forces raised at an increasing rate with the raise of radii. Therefore, Circular-4 was not considered which has a rather high drag.

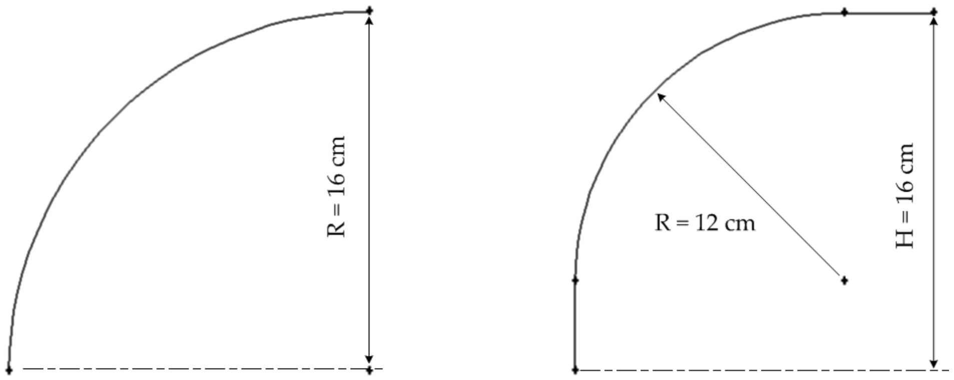

(a) Circular-16 (b) Circular-12

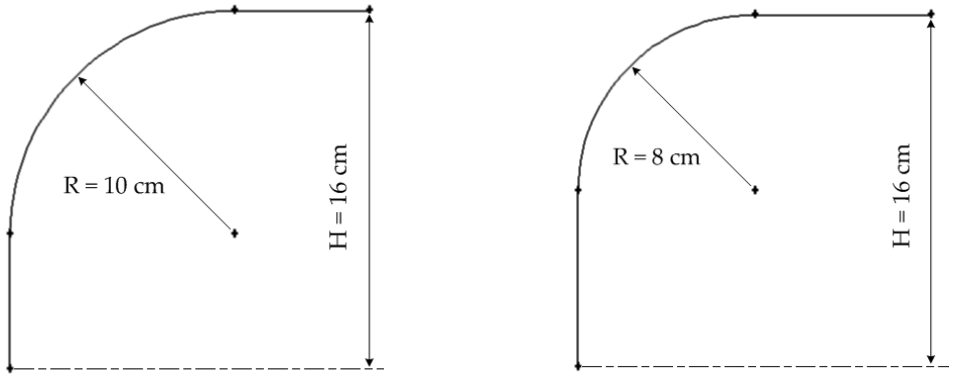

(c) Circular-10 (d) Circular-8

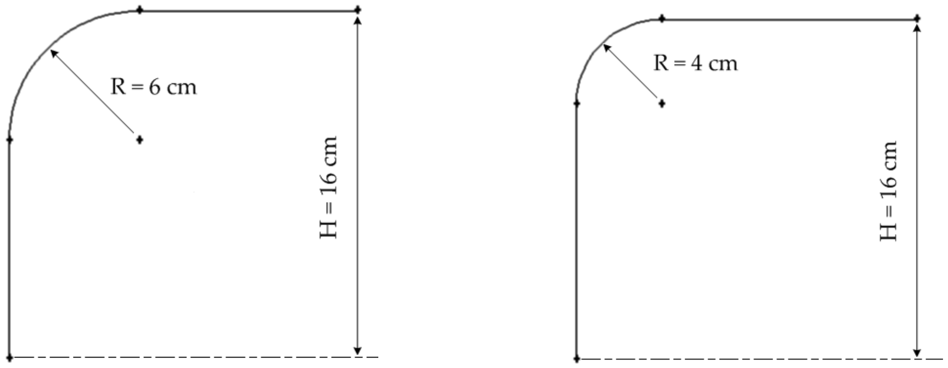

(e) Circular-6 (f) Circular-4

Figure 5.7. The tested flat-circular nose geometries

The contour plots of pressure coefficient for spherical nose models are as follows:

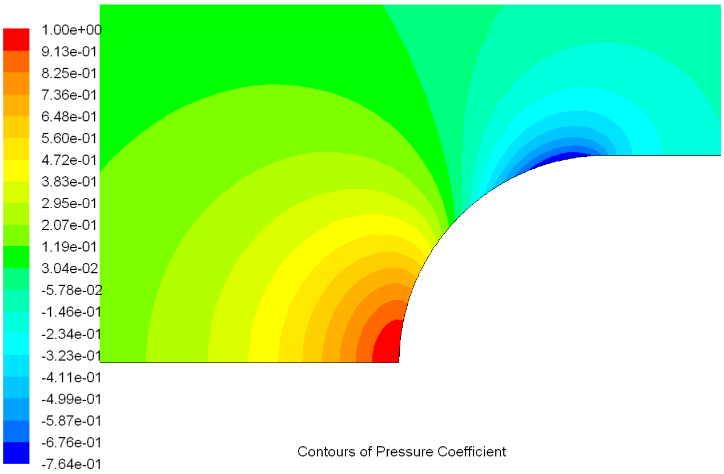

Figure 5.8. The contours of coefficient of pressure for Circular-16

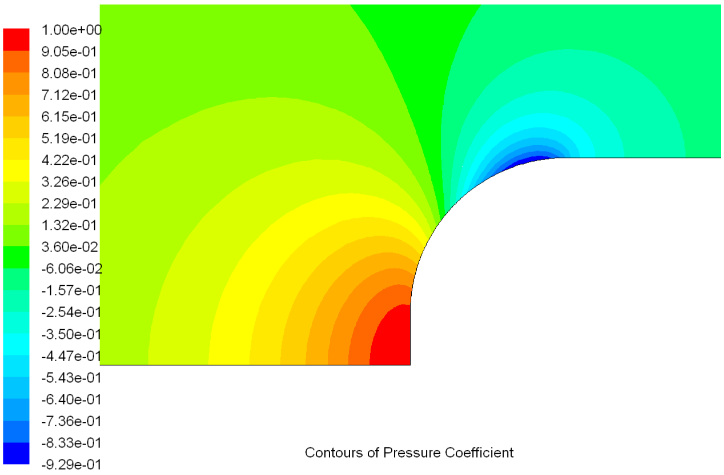

Figure 5.9. The contours of coefficient of pressure for Circular-12

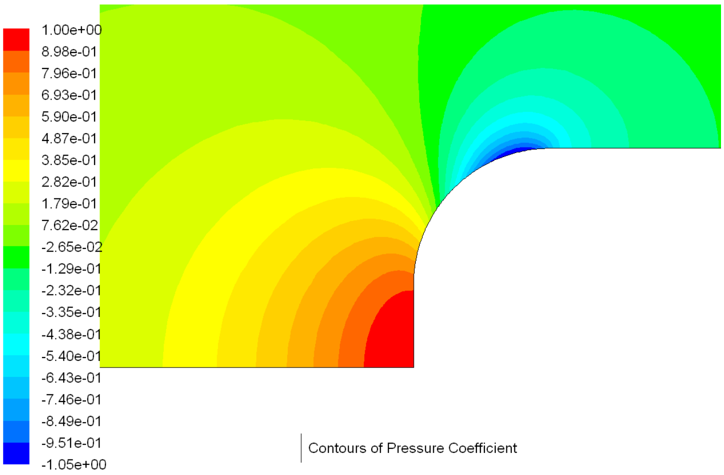

Figure 5.10. The contours of coefficient of pressure for Circular-10

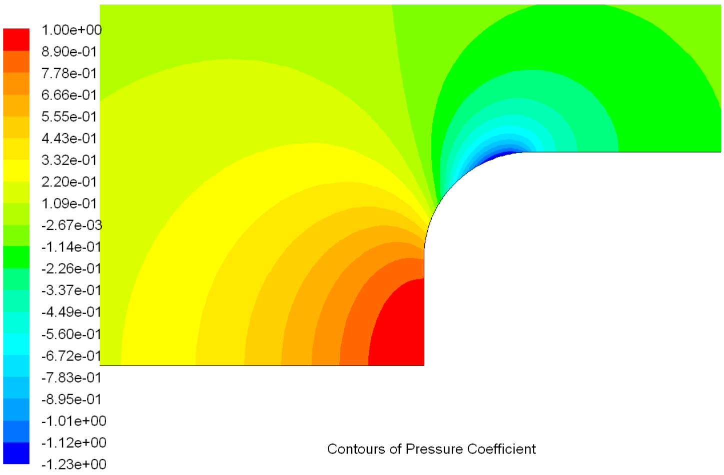

Figure 5.11. The contours of coefficient of pressure for Circular-8

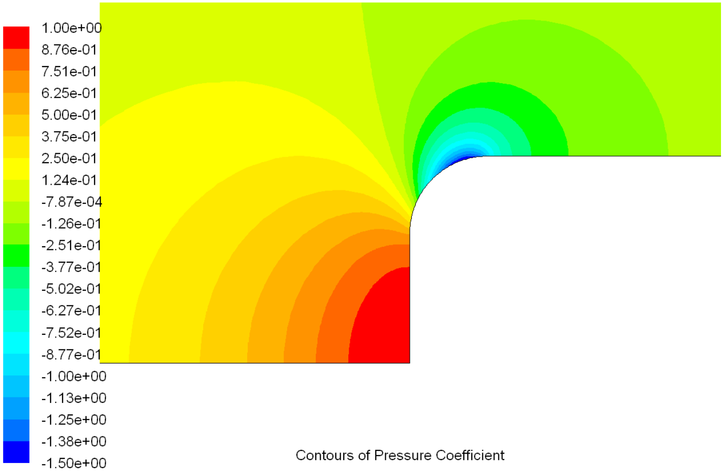

Figure 5.12. The contours of coefficient of pressure for Circular-6

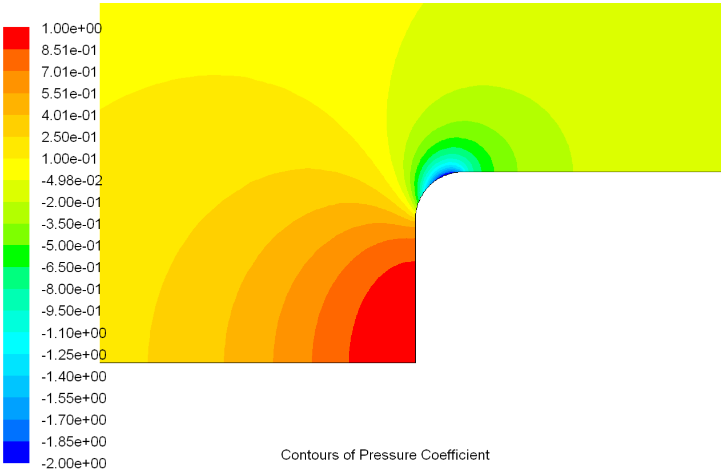

Figure 5.13. The contours of coefficient of pressure for Circular-4

5.2.2. Ellipsoid Nose Models

The ellipsoid models were created from the results of the previous section. Two flat areas were built with radii of 8 cm and 6 cm. In 2D drafts of the ellipsoid models, the flat vertical line was connected to the upper wall with ellipses. Different ellipses which were varying in radii-1 (The radius on x-axis) were constructed. The models built can be seen in Figures 5.14, 5.15.

Table 5.2. The results of ellipsoid with $R_2 = 6$ nose models

Model	Pressure Force	Friction Force	Total Force	C_{Dp}	C_{Df}	C_D
Ellipse-628	42.857 N	327.01 N	369.867 N	0.01068	0.08148	0.09216
Ellipse-624	43.245 N	327.604 N	370.849 N	0.01078	0.08163	0.09241
Ellipse-620	44.064 N	328.098 N	372.162 N	0.01098	0.08175	0.09273
Ellipse-616	45.561 N	328.464 N	374.025 N	0.01135	0.08185	0.09320
Ellipse-612	48.329 N	328.415 N	376.744 N	0.01204	0.08183	0.09388

Table 5.3. The results of ellipsoid with $R_2 = 8$ nose models

Model	Pressure Force	Friction Force	Total Force	C_{Dp}	C_{Df}	C_D
Ellipse-828	37.785 N	327.97 N	365.755 N	0.00942	0.08172	0.09114
Ellipse-824	38.884 N	328.416 N	367.3 N	0.00969	0.08183	0.09152
Ellipse-820	40.338 N	328.747 N	369.085 N	0.01005	0.08192	0.09197
Ellipse-816	42.609 N	328.912 N	371.521 N	0.01062	0.08196	0.09257
Ellipse-812	46.376 N	328.77 N	375.146 N	0.01156	0.08192	0.09348

The results of the ellipsoid geometry study was demonstrated in Tables 5.2, 5.3. The most efficient geometry is an ellipse with a large horizontal radius. However, the critical point is the difference in drag reduction with the change of the geometry. Model Ellipse-628 best suits the desired case since it has a large flat area and it has a lower drag which is approximately equal to the Circular-16 model and has a few higher drag force from the three ellipse models which have a lower flat area.

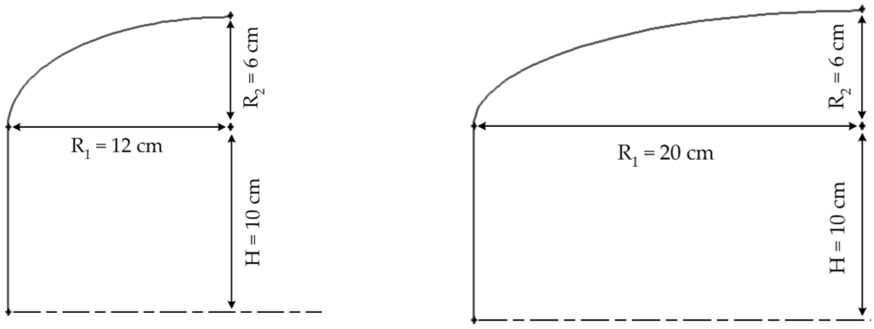

(a) ellipse-612 (c) ellipse-620

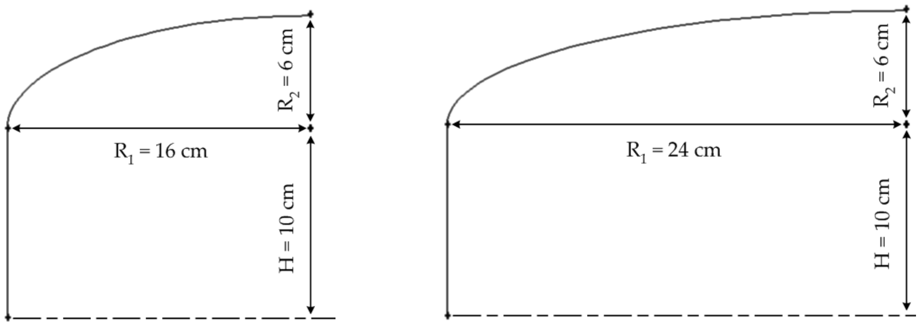

(b) ellipse-616 (d) ellipse-624

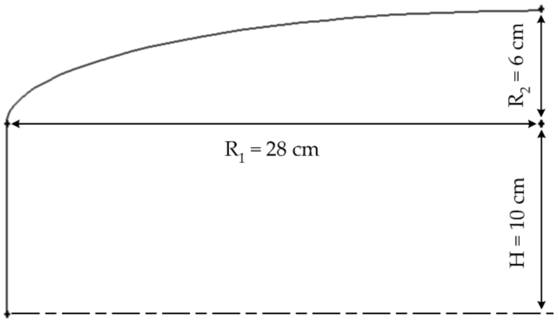

(e) ellipse-628

Figure 5.14. The flat-ellipse nose models with $R_2 = 6$ cm

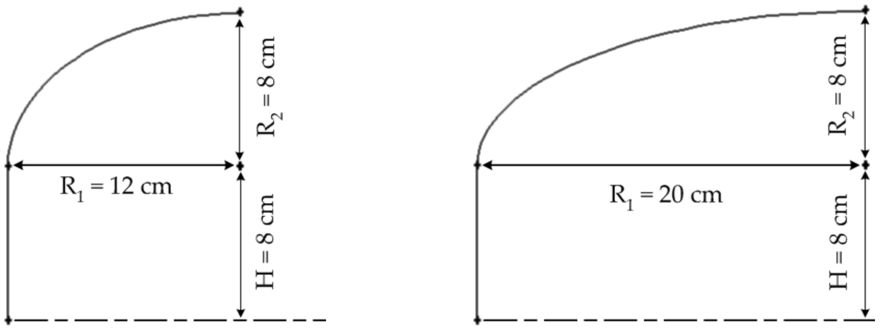

(a) ellipse-812 (c) ellipse-820

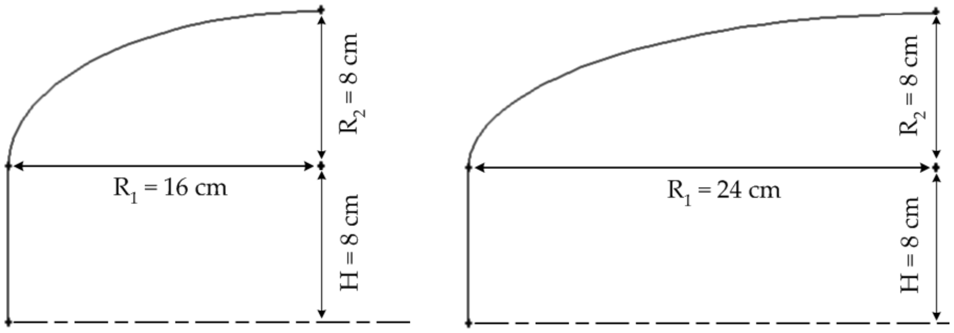

(b) ellipse-816 (d) ellipse-824

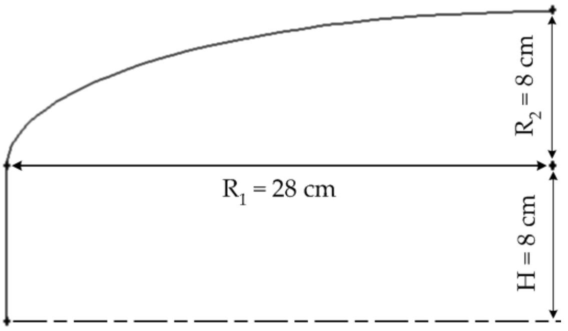

(e) ellipse-828

Figure 5.15. The flat-ellipse nose models with $R_2 = 8$ cm

The contour plots of pressure coefficient for ellipsoid nose models with R_2=6 cm are as follows:

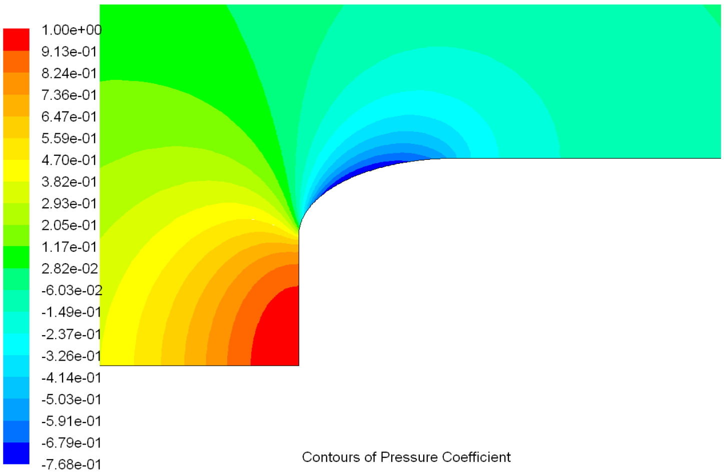

Figure 5.16. The contours of coefficient of pressure for Ellipse-612

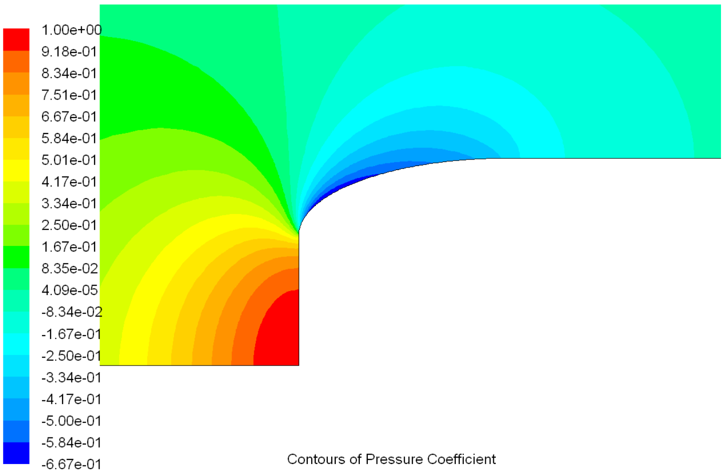

Figure 5.17. The contours of coefficient of pressure for Ellipse-616

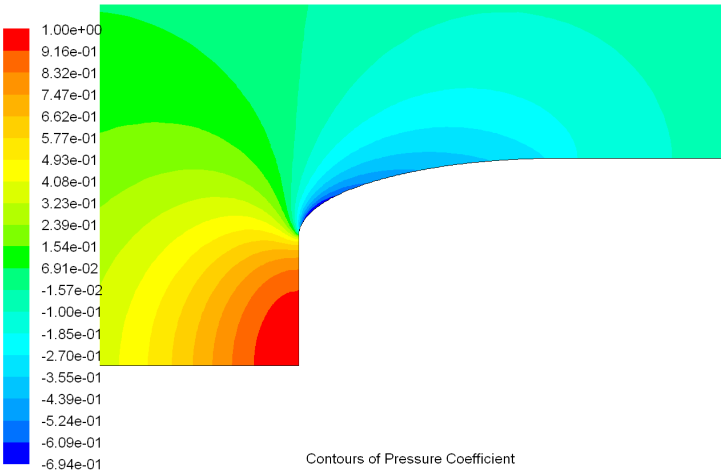

Figure 5.18. The contours of coefficient of pressure for Ellipse-620

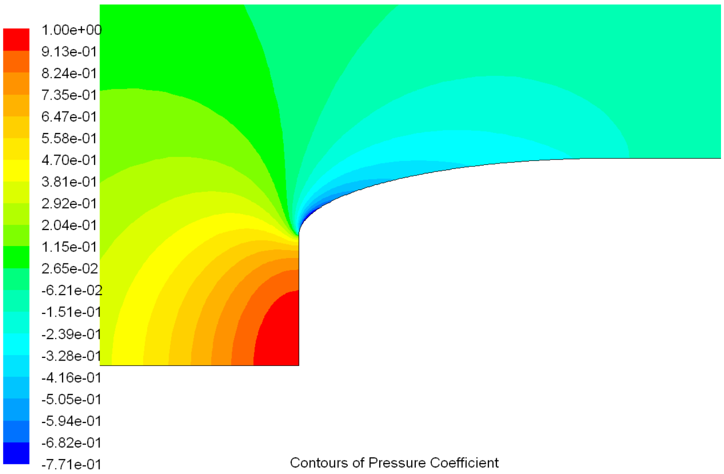

Figure 5.19. The contours of coefficient of pressure for Ellipse-624

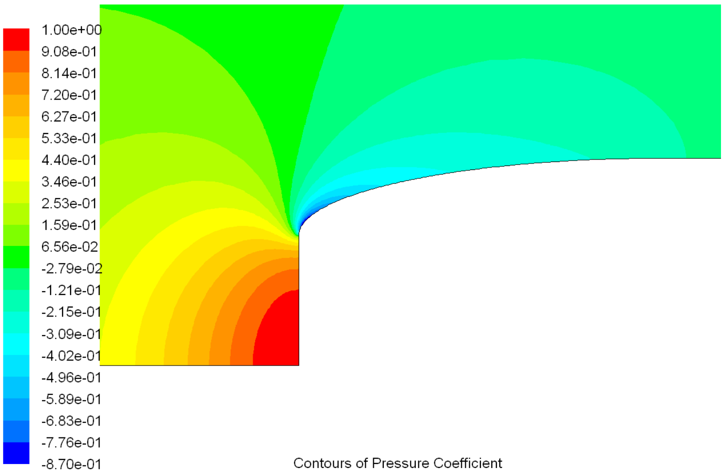

Figure 5.20. The contours of coefficient of pressure for Ellipse-628

The contour plots of pressure coefficient for ellipsoid nose models with R_2=8 cm are as follows:

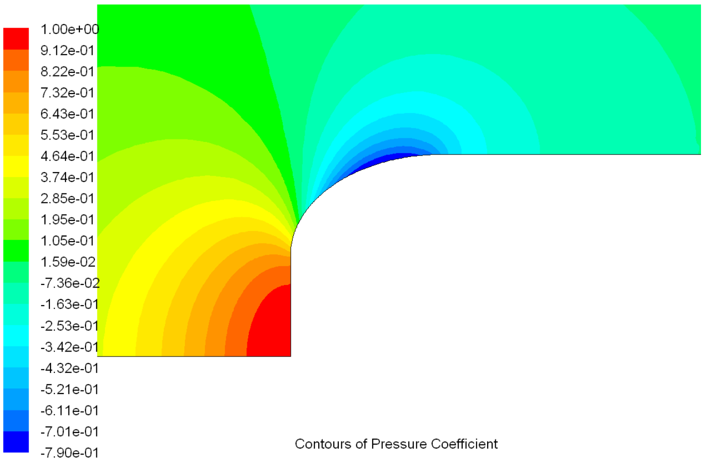

Figure 5.21. The contours of coefficient of pressure for Ellipse-812

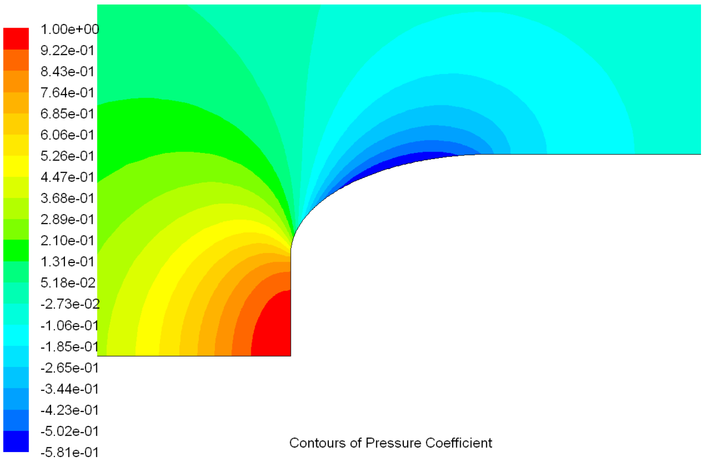

Figure 5.22. The contours of coefficient of pressure for Ellipse-816

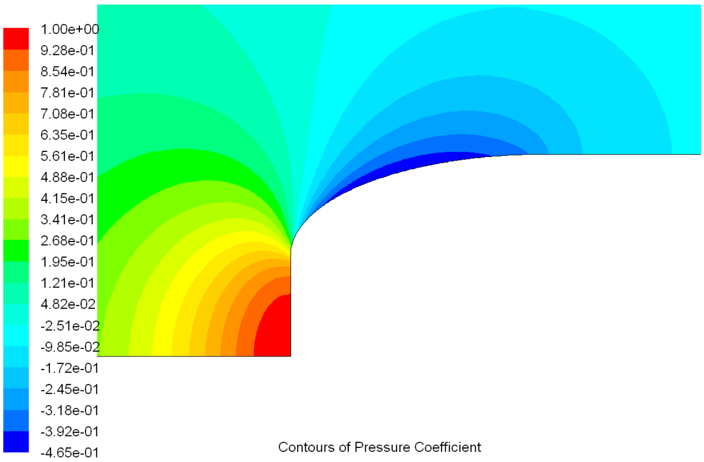

Figure 5.23. The contours of coefficient of pressure for Ellipse-820

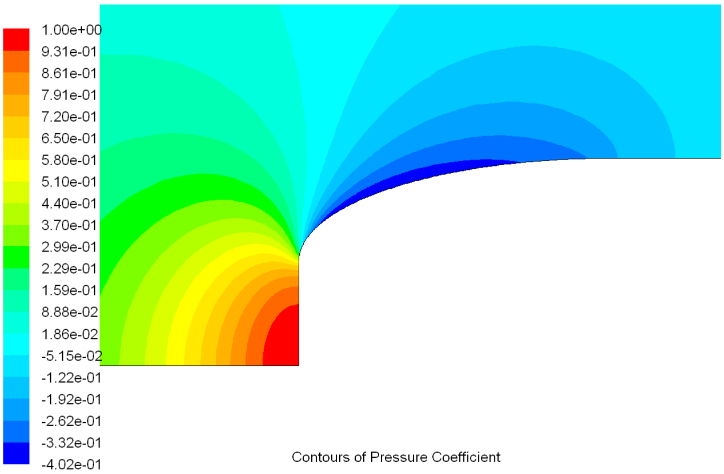

Figure 5.24. The contours of coefficient of pressure for Ellipse-824

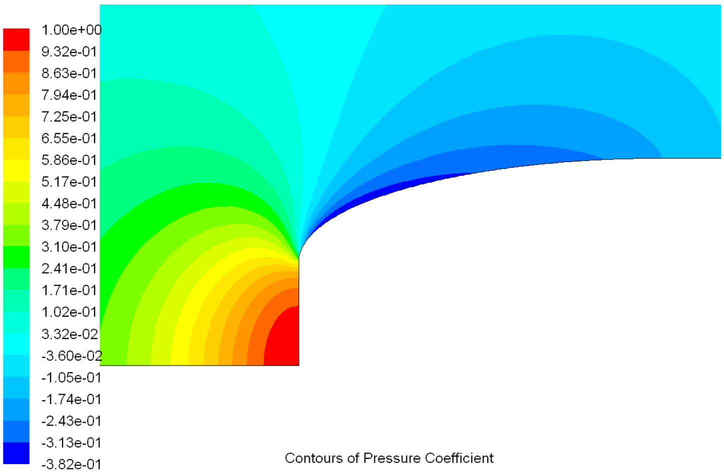

Figure 5.25. The contours of coefficient of pressure for Ellipse-828

5.2.3. Design of Afterbody

The points that were considered to obtain the appropriate geometry were related to the boundary layer theory. The discontinuity of the surface disturbs the steady nature of the boundary layer. Therefore, at any point on the surface the right side and left side slopes for the point should be equal or in other words the right and left derivatives should be equal at any point for the geometry. However, like in any other engineering case these are not the only points that will be considered in designing of a tool or a system and are restricted with mechanical or other design considerations.

The afterbody of an object should be designed with care since the separation is expected to occur at that region. If the afterbody ends steeply there is no chance for a viscous flow to follow the body. Being realistic the separation will occur in each case but the problem is where it occurs. If it occurs closer to the stagnation point the drag is large but if it occurs at a point further from the previous location the drag force decreases. Therefore, pushing the location of separation to the afterbody of the object is considered and this is done by modification of the geometry. However, this is not the only criterion since the changes in boundary layer profile will affect the shear forces and shear forces will be different for each different geometry so again it is seen that CFD is the best choice since different reasonable models can be compared efficiently.

For the study of the afterbody geometry four different models were constructed. The models were built by combining a parabola and an ellipse where their slopes or in other words their derivatives are equal. In order to do these an algorithm was developed to predict the appropriate equations of the ellipses and the parabolas. The geometries created are demonstrated in Figure 5.26.

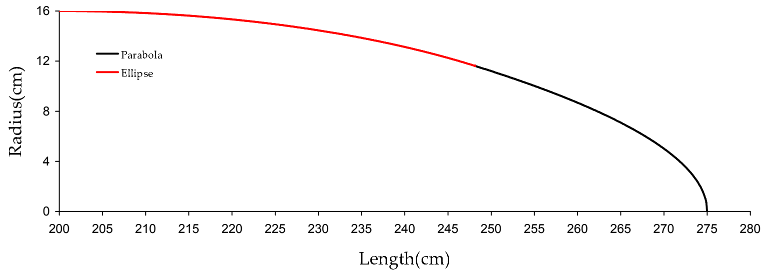

(a) Model Afterbody-70 ($R_1 = 70$ for the ellipse)

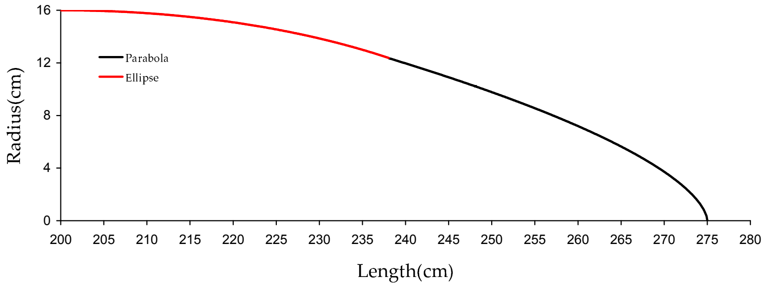

(b) Model Afterbody-60 ($R_1 = 60$ for the ellipse)

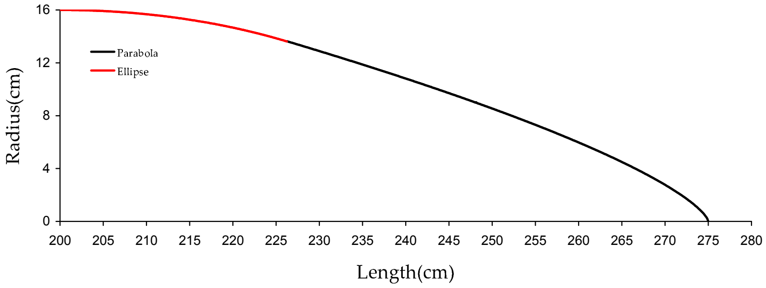

(c) Model Afterbody-50 ($R_1 = 50$ for the ellipse)

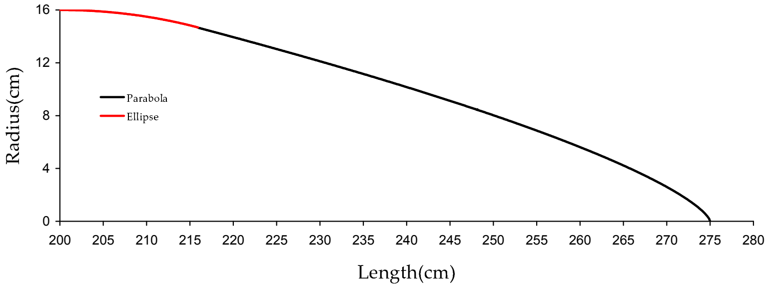

(d) Model Afterbody-40 ($R_1 = 40$ for the ellipse)

Figure 5.26. The afterbody geometries constructed

The results were listed in Table 5.4. As expected, model Afterbody-40 has the lowest drag since it has a rather lower camber. The pressure distribution is not varying much between models as it can be seen from the coefficient of pressure drag values. The friction drag is lower for the Afterbody-40 model. It is seen that reduction of drag is achieved by body shaping but through reduction of friction drag. In literature there are AUV (Autonomous underwater vehicle) studies which use this technique. However, in a torpedo, design is limited with other considerations and a dolphin like body shape does not seem possible which is one of the best shape for low friction and pressure drag.

Table 5.4. The results of different afterbody geometries

Model	Pressure Force	Friction Force	Total Force	C_{Dp}	C_{Df}	C_D
Afterbody-40	33.034 N	302.74 N	335.774 N	0.00823	0.07544	0.08367
Afterbody-50	33.278 N	305.507 N	338.785 N	0.00829	0.07613	0.08442
Afterbody-60	33.306 N	310.129 N	343.435 N	0.00830	0.07728	0.08558
Afterbody-70	34.057 N	314.926 N	348.983 N	0.00849	0.07847	0.08696

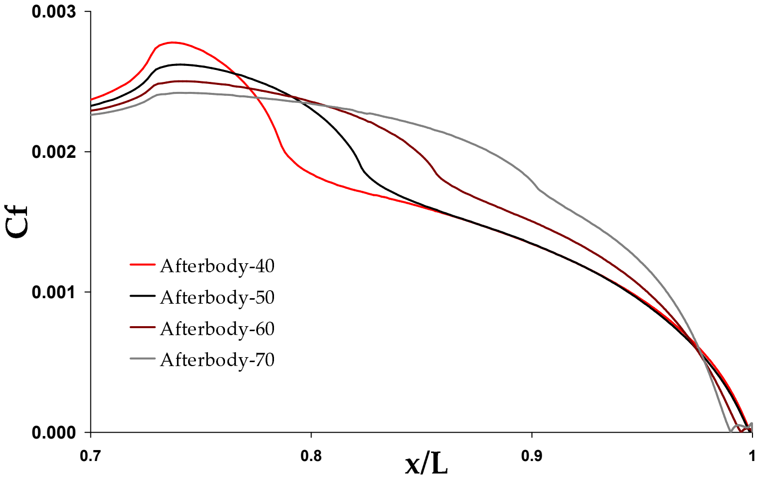

Figure 5.27. The skin friction coefficient values for the tail geometries

The contour plots of velocity for the four different afterbodies are as follows:

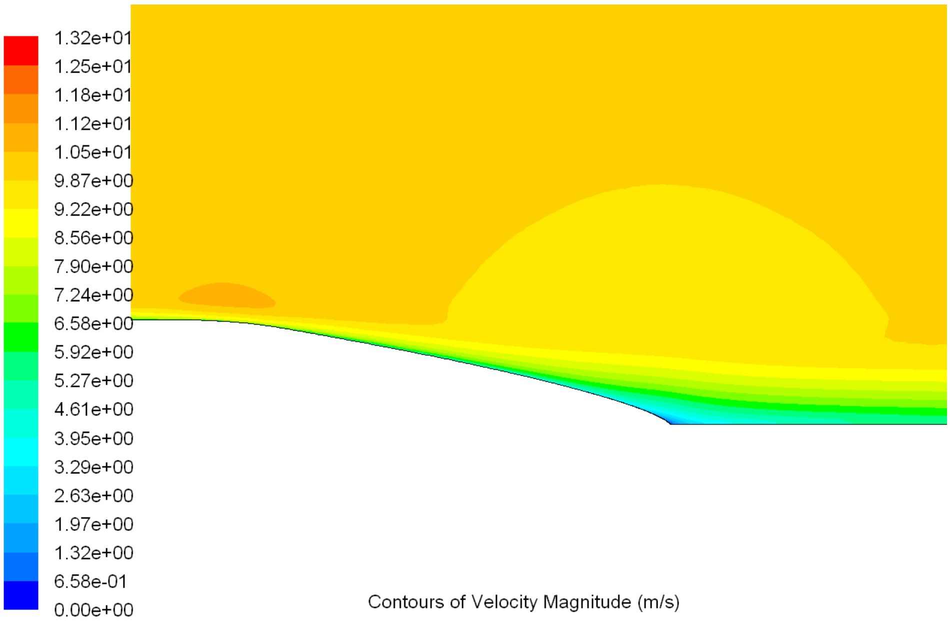

Figure 5.28. The contours of velocity magnitude for Afterbody-40

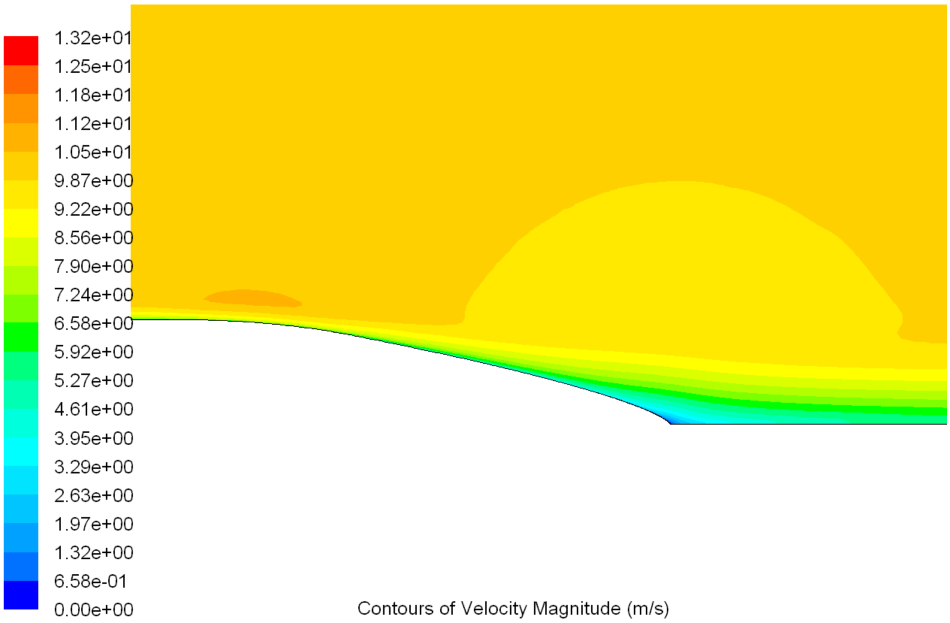

Figure 5.29. The contours of velocity magnitude for Afterbody-50

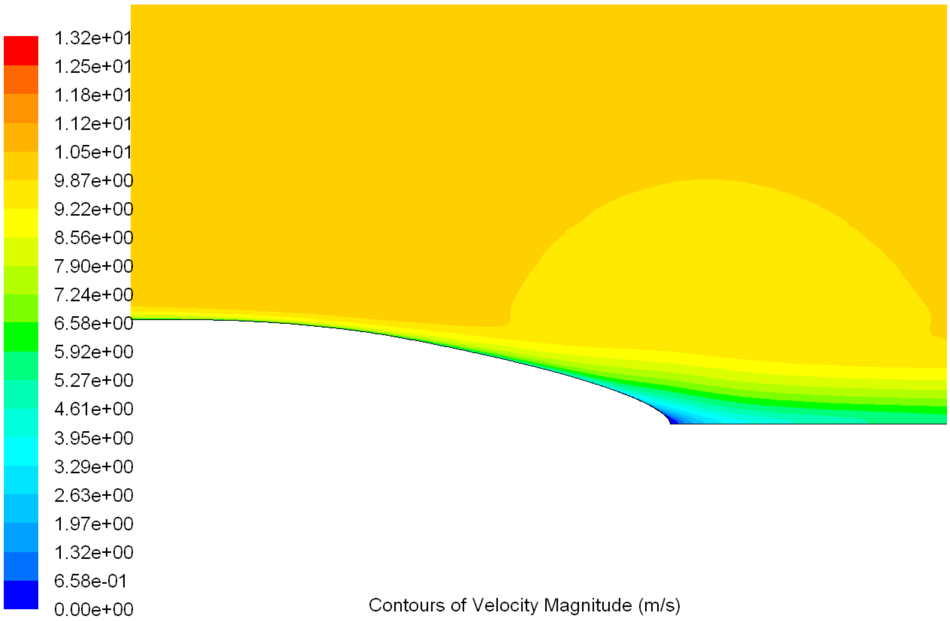

Figure 5.30. The contours of velocity magnitude for Afterbody-60

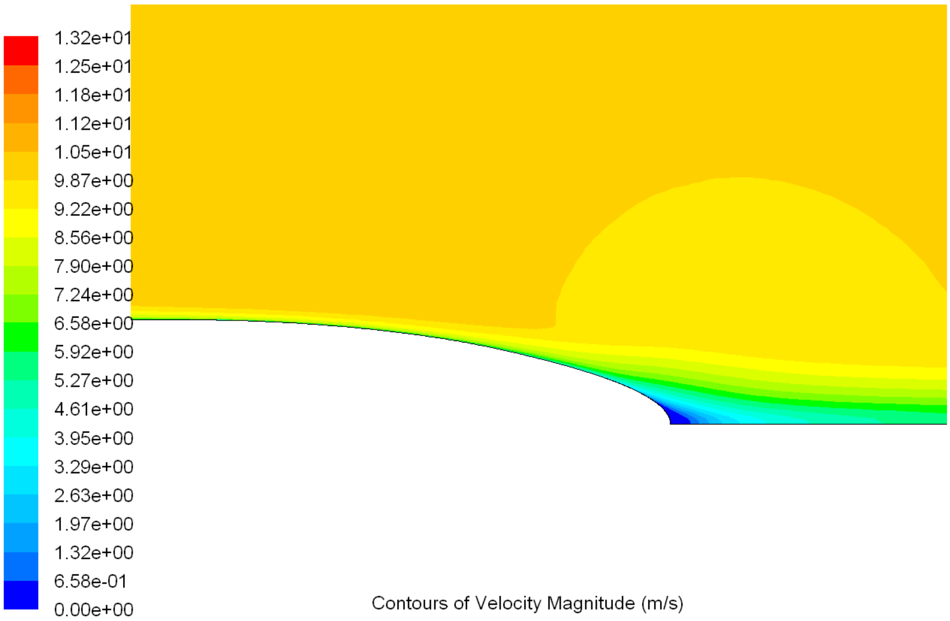

Figure 5.31. The contours of velocity magnitude for Afterbody-70

5.3. Addition of the Fan Boundary

At this stage of the study there is an approximate shape at hand. However, this resembles a projectile rather than a torpedo since it does not have a propeller and fins. Propeller can not be modeled in 2D axisymmetric space since it is not a body of revolution. Therefore, in order to simulate the effects of a propeller a fan boundary condition was used at the back of the geometry (Figure 5.32).

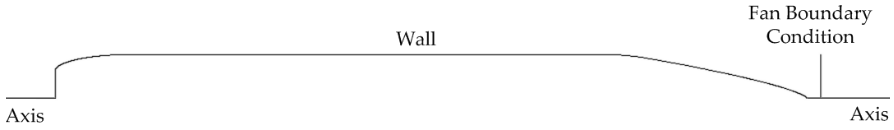

Figure 5.32. The rebuilt geometry with the fan boundary condition

Fan boundary condition requires the characteristic properties of a propeller. There is also a constant pressure jump option available. The pressure jump means that there is a negative pressure difference equal to the pressure upstream of the fan minus the pressure downstream of the fan (Equation 5.1). In order to create a thrust force there should be a pressure drop upstream of the fan and a pressure increase downstream of the fan.

$$F_{\text{thrust}} = (P_2 - P_1)A \tag{5.1}$$

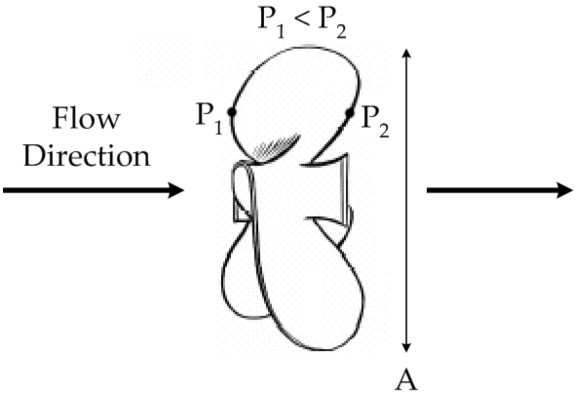

Figure 5.33. Demonstration of a simple propeller

The thrust force should be equal to drag force at the top speed of the torpedo (Net force must be equal to zero according to Newton's first principle). At 20 m/s the drag force is found to be 1218.7 N. Using the Equation 5.1 the pressure drop was calculated as 15153 Pa. This was the pressure drop initial condition for the fan boundary. The computation with the fan downstream yielded the results in Table 5.5.

Table 5.5. The effect of fan boundary in quantities

Model	Pressure Force	Friction Force	Total Force	C_{Dp}	C_{Df}	C_D
Afterbody-40	116.9 N	1101.7 N	1218.6 N	0.00729	0.06863	0.07592
Afterbody-40 + Fan	183.4 N	1102.7 N	1286.1 N	0.01143	0.06870	0.08012

However, since the drag force increased with the addition of the fan boundary, thrust force should also be changed. In other words, multiplication of pressure drop with fan area must be equal to the thrust force at that time. Explicitly, the thrust force predicted was 1218.7 N so the pressure drop was calculated as 15153 Pa, but now the thrust force is 1286.2 and the thrust force is smaller than this value. Therefore, some iterative steps must be executed in order to find the solution when the pressure drop is matching the drag force calculated. This was done in the next section.

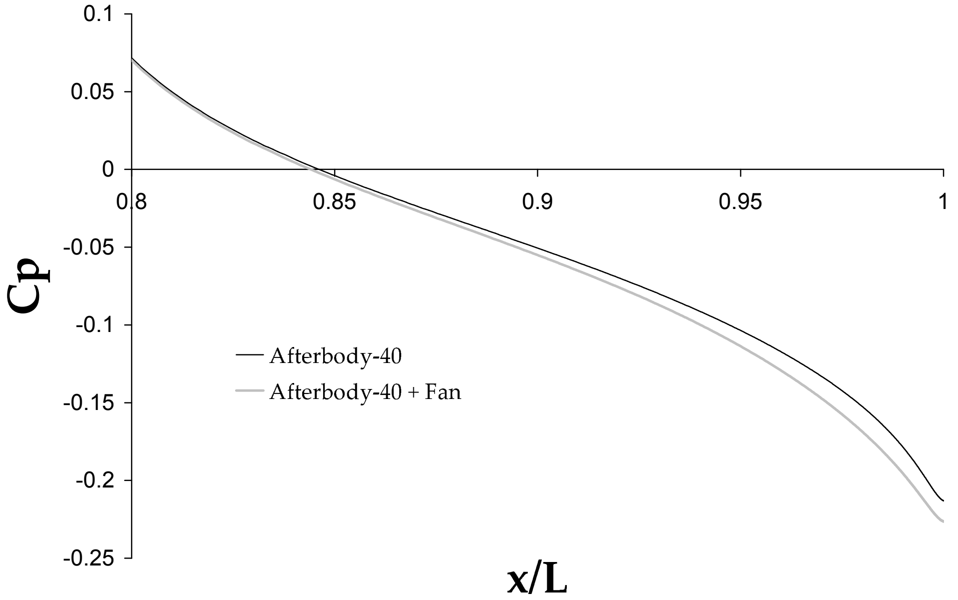

Figure 5.34. Distribution of pressure coefficient (negative values of C_p)

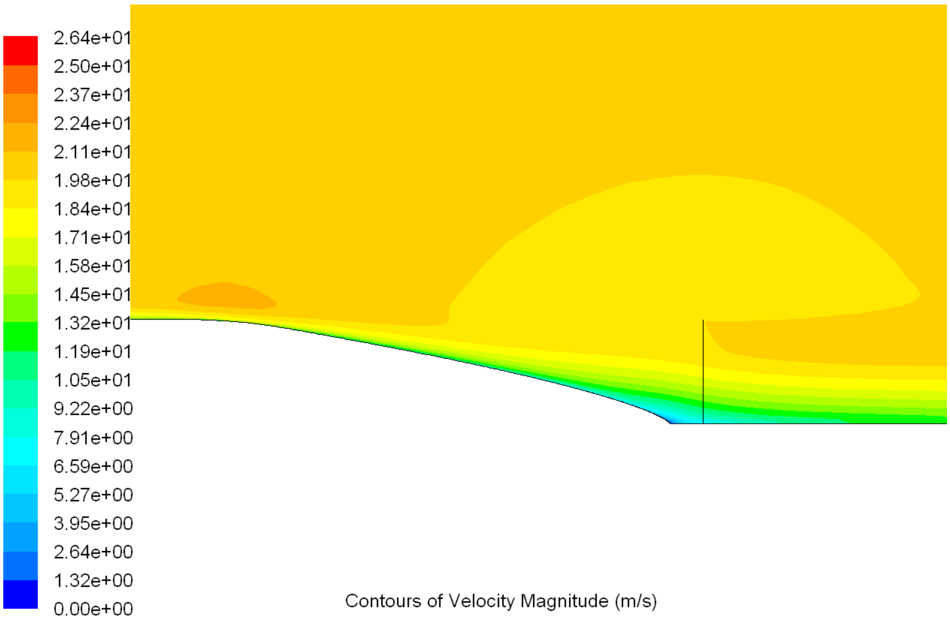

Figure 5.35. The contours of velocity magnitude for Afterbody-40 + fan boundary

5.4. Finishing the Design

In order to achieve the most realistic results in 2D environment a shaft was added to the geometry. This was the upper bound for the design. The rotation of the shaft was also provided with the moving wall condition. A rotational speed of 2000 rpm was assigned to the shaft which is in a reasonable range. The problem was solved with the axisymmetric equations with swirl velocities involved. The diameter of the shaft was chosen as 1 inch. The gravitation and buoyancy effects were also included although their contributions are lower.

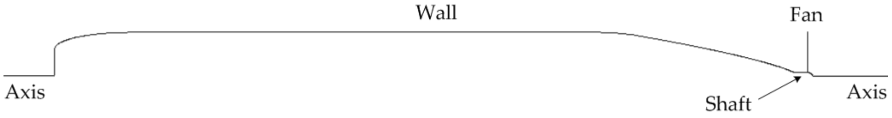

Figure 5.36. Final case of the design

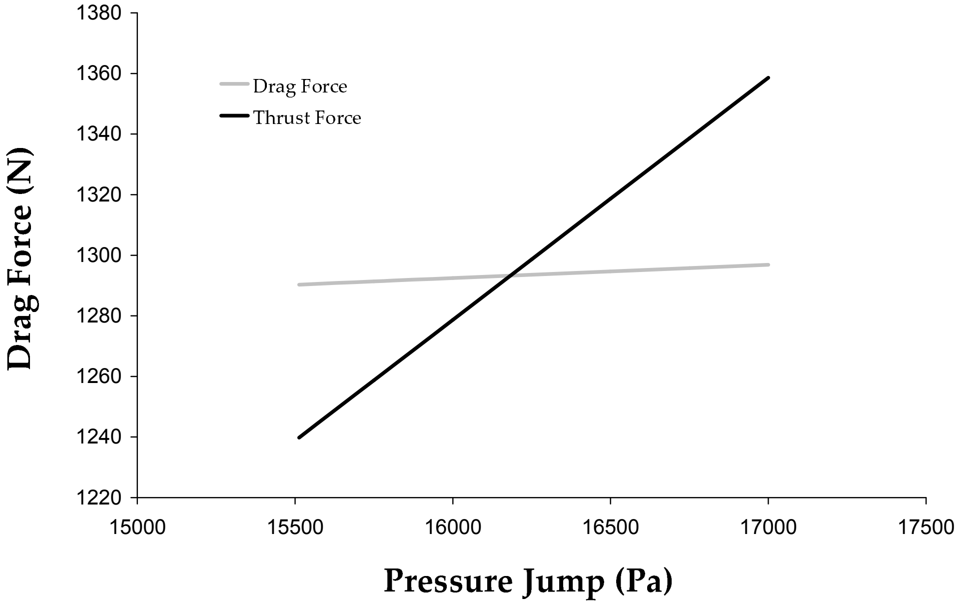

Figure 5.37. The drag and thrust values for pressure jump initial conditions

Matching of the appropriate pressure jump with the drag force was done in multiple steps. First, the pressure jump was set equal to the drag force for the projectile alone. Then, assigning incrementally new pressure jump initial conditions resulted the two curves in Figure 5.37. The equations of the curves were solved together and a new computation was performed with a value of 16184 Pa (estimated from the intersection point) for the pressure jump.

Initial condition for the fan boundary pressure jump was set to 16184 Pa and a drag force 1293.33 N was found which is equal to the thrust generated by the propeller. This is the complete model for the study and all the initial conditions are known. Flow field and boundary layer is determined. However, there should be some drag force due to propeller. This was not considered in the study.

Figure 5.38. Side view of the torpedo

Table 5.6. The forces on the body at different initial pressure jump conditions

	Pressure Force	Friction Force	Total Force
Pressure jump = 15513 Pa, Thrust = 1239.76 N			
Shaft	-15.790 N	0.875 N	-14.915 N
Wall	202.412 N	1102.801 N	1305.214 N
Net	186.622 N	1103.677 N	1290.299 N
Pressure jump = 15750 Pa, Thrust = 1258.71 N			
Shaft	-15.849825 N	0.877 N	-14.973 N
Wall	203.50103 N	1102.820 N	1306.321 N
Net	187.651 N	1103.696 N	1291.348 N
Pressure jump = 16000 Pa, Thrust = 1278.69 N			
Shaft	-15.913226 N	0.879 N	-15.034 N
Wall	204.64891 N	1102.839 N	1307.488 N
Net	188.736 N	1103.717 N	1292.453 N
Pressure jump = 16250 Pa, Thrust = 1298.67 N			
Shaft	-15.976633 N	0.881 N	-15.096 N
Wall	205.78877 N	1102.858 N	1308.646 N
Net	189.812 N	1103.738 N	1293.550 N
Pressure jump = 16500 Pa, Thrust = 1318.65 N			
Shaft	-16.040046 N	0.883 N	-15.158 N
Wall	206.92692 N	1102.876 N	1309.803 N
Net	190.887 N	1103.759 N	1294.646 N
Pressure jump = 16750 Pa, Thrust = 1338.63 N			
Shaft	-16.103464 N	0.884 N	-15.219 N
Wall	208.07773 N	1102.895 N	1310.973 N
Net	191.974 N	1103.779 N	1295.754 N
Pressure jump = 17000 Pa, Thrust = 1358.61 N			
Shaft	-16.166889 N	0.886 N	-15.281 N
Wall	209.22216 N	1102.914 N	1312.136 N
Net	193.055 N	1103.800 N	1296.856 N

5.4.1. The Results of Final Design

The estimated values for pressure, friction and total drag are given in Table 5.7. The boundary layer thickness in Figure 5.39 deviates and climbs up steeply after the deflection point at 2.4 m on afterbody. The forebody of the boundary layer resembles the flat plate boundary layer for which the flat plate solution will be used.

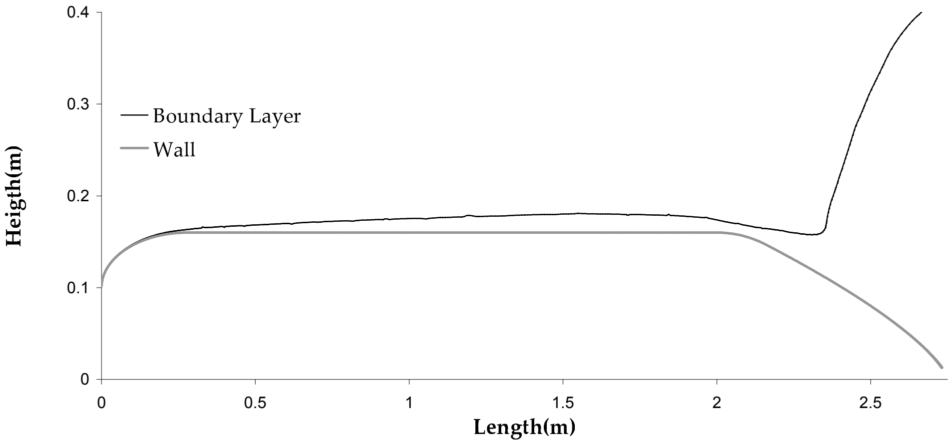

Figure 5.39. The boundary layer thickness for the torpedo

Table 5.7. The drag forces and coefficients on the final model

	Pressure	Friction	Total	C$_{Dp}$	C$_{Df}$	C$_{D}$
Shaft	-15.871	0.881	-14.990	-	-	-
Wall	205.472	1102.852	1308.324	-	-	-
Net	189.601	1103.733	1293.334	0.01181	0.06876	0.08057

There is a separation at the point 0.999 L seen in Figure 5.40. This is so the body is streamlined. However, that separation should be a result of the deficiency in attachment part between the wall and the shaft.

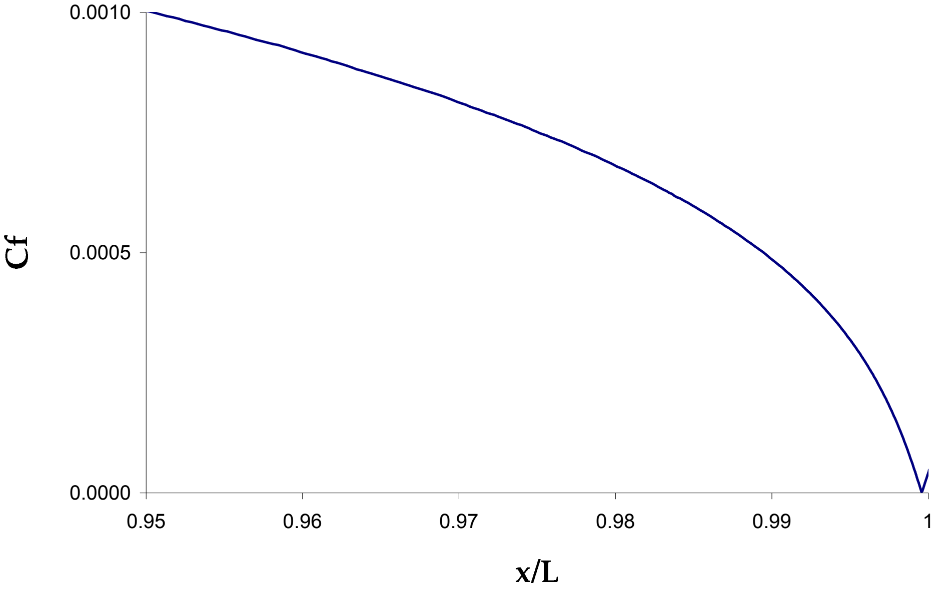

Figure 5.40. The distribution of surface friction coefficient at the tail

If the axial wall stress is examined (Figure 5.41) it is noticed that the axial shear stress is very high at the leading part of the wall. The boundary layer is very thin at that region and axial stress is relatively low closing to the afterbody because of the thickening of the boundary layer.

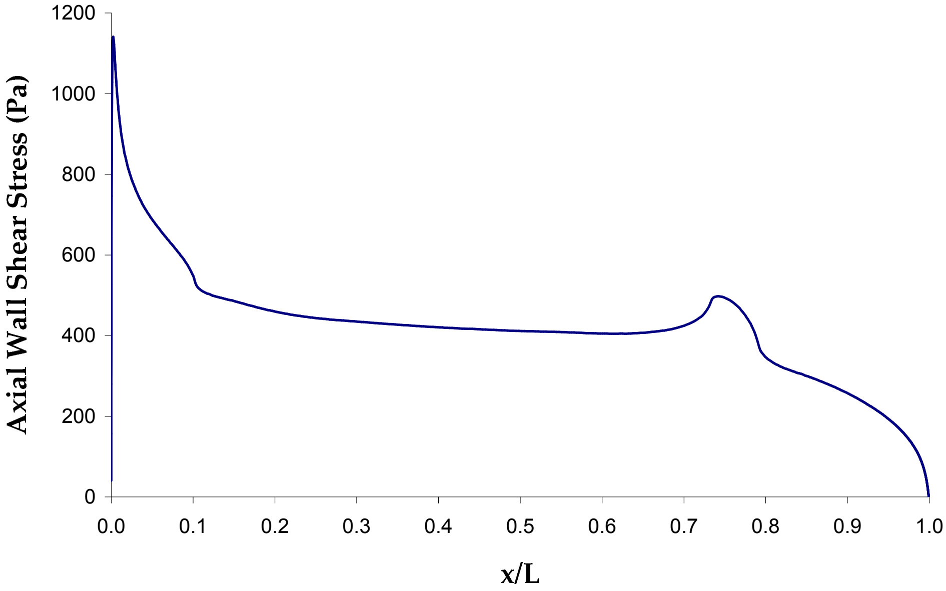

Figure 5.41. The distribution of the axial shear forces on the surface

Looking at the pressure distribution (Figure 5.42) the pressure fluctuation is noticed on the shaft that is possibly due to rotation and the effect of the propeller.

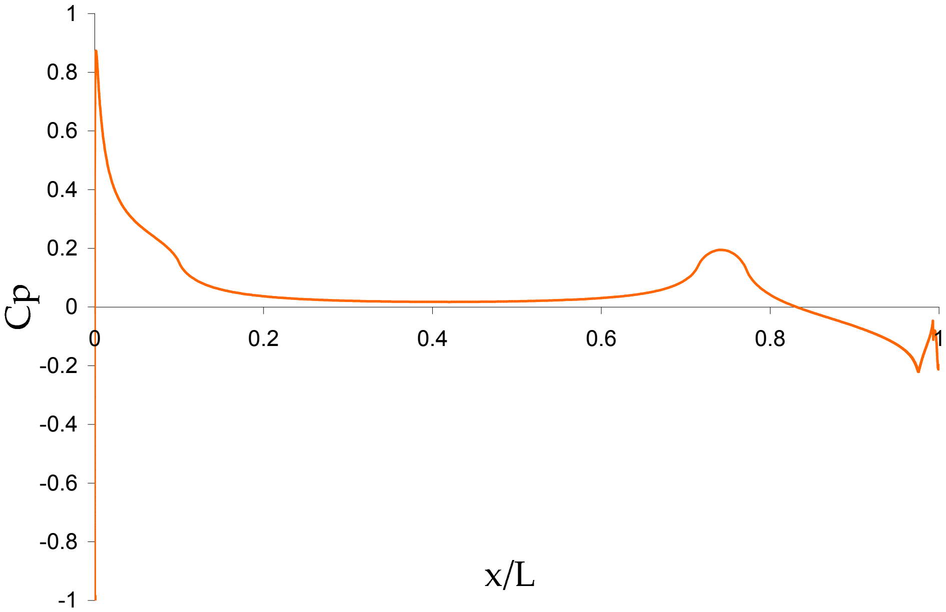

Figure 5.42. The distribution of pressure coefficient (- value) on the wall and the shaft

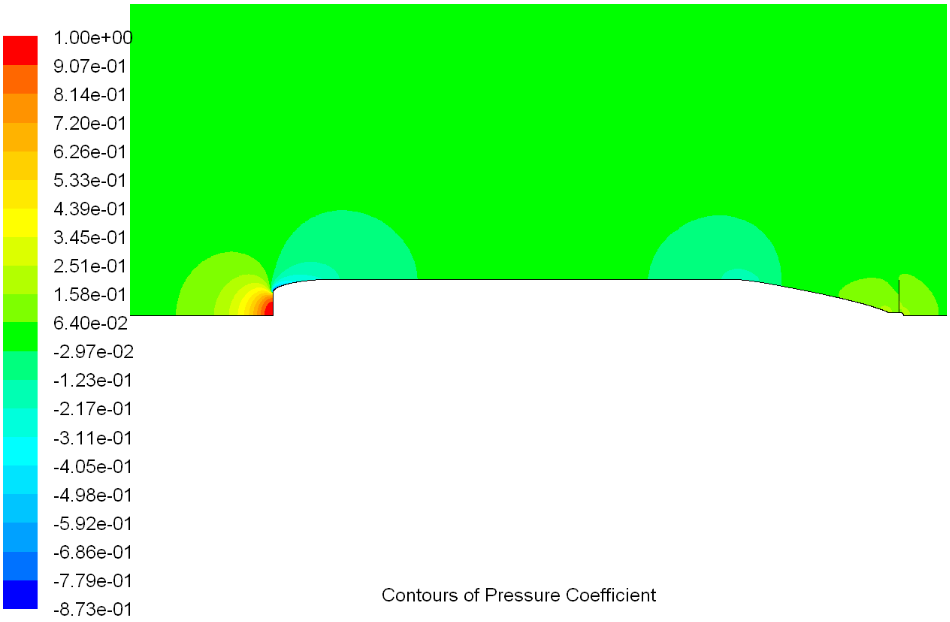

Figure 5.43. The contours of pressure coefficient on final model

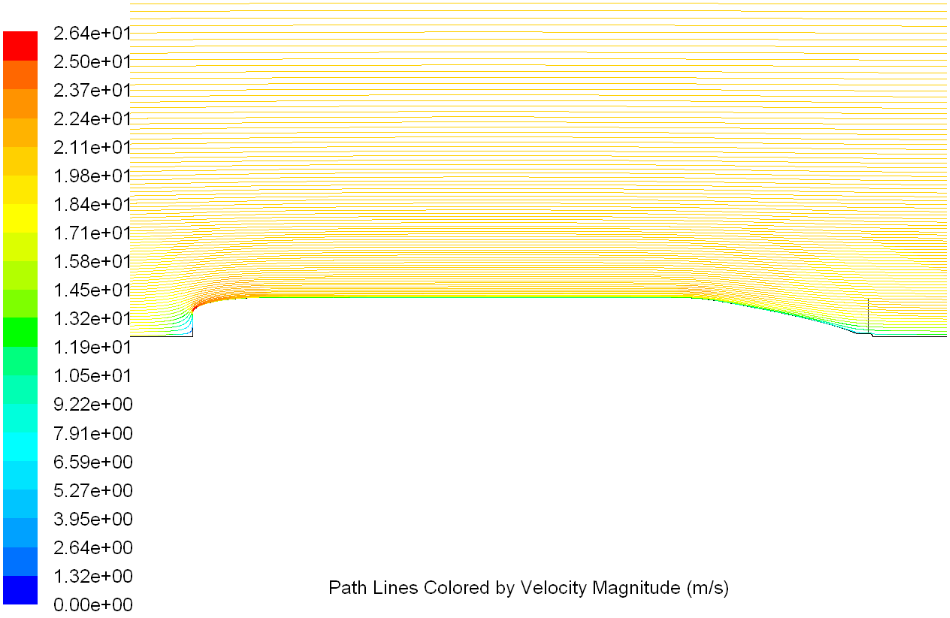

Figure 5.44. The pathlines colored with velocity magnitude on final model

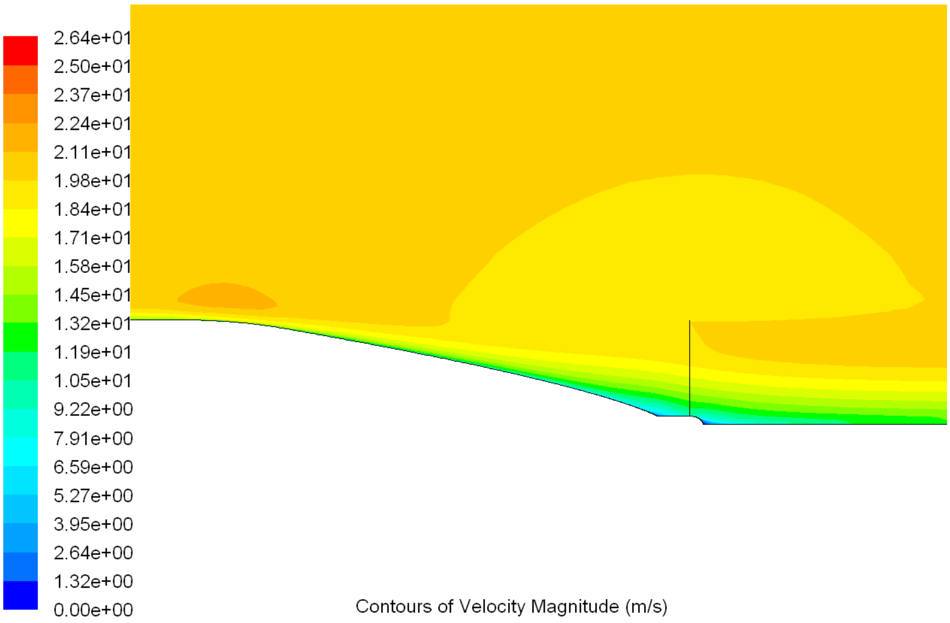

Figure 5.45. The contours of velocity magnitude at afterbody

5.5. The Effect of Friction Drag Reduction

The friction drag is overwhelmingly dominant on a torpedo. The share of friction drag in total drag was found to be 85.3%. Therefore, reduction of friction drag studies on torpedoes should attract more attention.

The contribution of the surface regions of the torpedo to the total friction drag can be seen in Table 5.8. The region close to the tip point of the torpedo is exposed to high friction. The friction first lowers and then continues approximately with same magnitude up to the afterbody. The thickening of the boundary layer changes the velocity gradient and so the surface friction on afterbody.

Table 5.8. The distribution of friction drag to surface regions

Region (x/L)	Friction Drag	Share in %
0.0 - 0.1	189.148 N	17.20%
0.1 - 0.2	134.484 N	12.20%
0.2 - 0.3	123.810 N	11.20%
0.3 - 0.4	117.914 N	10.70%
0.4 - 0.5	114.229 N	10.35%
0.5 - 0.6	110.330 N	10.00%
0.6 - 0.7	111.890 N	10.14%
0.7 - 0.8	120.842 N	10.95%
0.8 - 0.9	60.686 N	5.50%
0.9 - 1.0	19.520 N	1.76%
Total	1102.852 N	-

The distribution of the frictional forces on different regions of torpedo surface also shows the areas where the friction drag reduction should be applied. The drag reduction ratio between 0.8 L and 1.0 L is very low about 5% and this makes no sense as the top speed will increase by 0.5 m/s. Although it is a gain, it can not be named as efficient. Therefore, the drag reducer should be concentrated on regions where the drag is continuously high. This is the 0 - 0.8 L region of the torpedo.

In Figure 5.46 the result of reduction in friction drag can be seen. In order to obtain the top speeds for different ratios of friction drag reduction some computations were performed starting at 25 m/s and ending at 40 m/s. For an amount of reduction in friction drag, the top speed was determined where the total reduced drag force is equal to the thrust force at that speed. As an example, at 34 m/s the pressure drag is 383.76 N, friction drag is 2971.6 N and the total drag is 3355.36 N, which is greater than the thrust force. However, if you assume that the friction drag is reduced by a factor of 3.27, the total drag force is equal to the thrust force and then the torpedo can reach the speed of 34 m/s. Similarly, the top speeds for different drag reduction ratios were estimated.

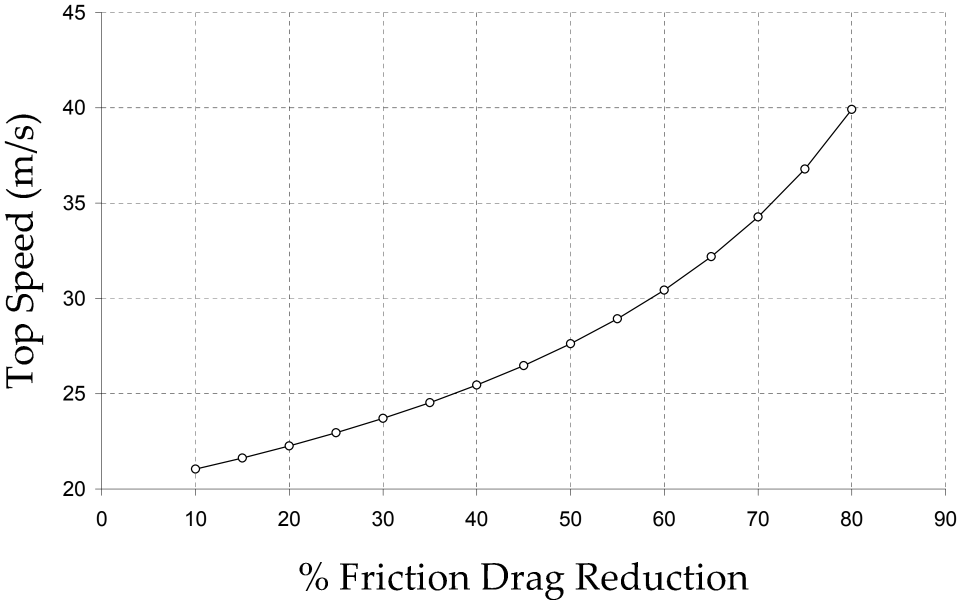

Figure 5.46. The effect of reduction of friction drag to the top speed of the torpedo

Table 5.9. The magnitudes of top speed for different reduction of surface friction ratios

% Reduction of Friction Drag	Top Speed
8%	20.82 m/s
10%	21.04 m/s
15%	21.63 m/s
20%	22.26 m/s
25%	22.95 m/s
30%	23.71 m/s
35%	24.53 m/s
40%	25.45 m/s
45%	26.47 m/s
50%	27.63 m/s
55%	28.93 m/s
60%	30.44 m/s
65%	32.19 m/s
70%	34.27 m/s
75%	36.79 m/s
80%	39.92 m/s

5.5.1. Flat Plate Approximation for MDR Case

The friction drag can be reduced up to 80% by polymer injection. However, the studies are generally experimental since the turbulent drag reduction phenomenon does not have an accepted mechanism and a mathematical model, besides, the numerical simulations can only be performed with DNS (Direct Numerical Simulation). There are some theories introduced into k-ϵ turbulence model that use the shear thinning viscosity models but they are restricted with Reynolds number. For high Reynolds numbers the models are deflecting from the reality. This must be since the mechanism of the turbulence is not understood well.

In order to find an approximate solution for polymer induced case, the boundary layer of the torpedo was assumed a flat plate boundary layer. However, it is clearly seen from Figure 5.39 that the boundary layer does not have steady fashion like a flat plate. At the inflection point it gets thinner than it becomes thicker and separates near the shaft.

Therefore, the approximation can be done in certain limits. In order to reach this aim, a flat plate boundary layer problem was solved for a comparison, using a 1500×100 structured mesh and a same length flat plate. The boundary layer was determined for the same initial conditions. In Figure 5.47 it is seen that for a certain interval starting with the edge of the plate and the torpedo, the boundary layers show similarities. At the point of deflection of the torpedo geometry the boundary layer is also deflecting, actually it deflects before but at the deflection point it descends steeply. Therefore, for a reference length to use in flat plate solution, 0.72 L is suitable.

Using Larson's work explained in theory section, an approximate value was found for the C_f value. In first situation the drag reduction for the MDR case was evaluated. The Reynolds number was found as $Re_x = 3.78 \times 10^7$.

Using the Reynolds number C_f values were found as 0.0025216 and 0.0005839 for Newtonian and MDR cases respectively. Larson claims that his derivations ap-

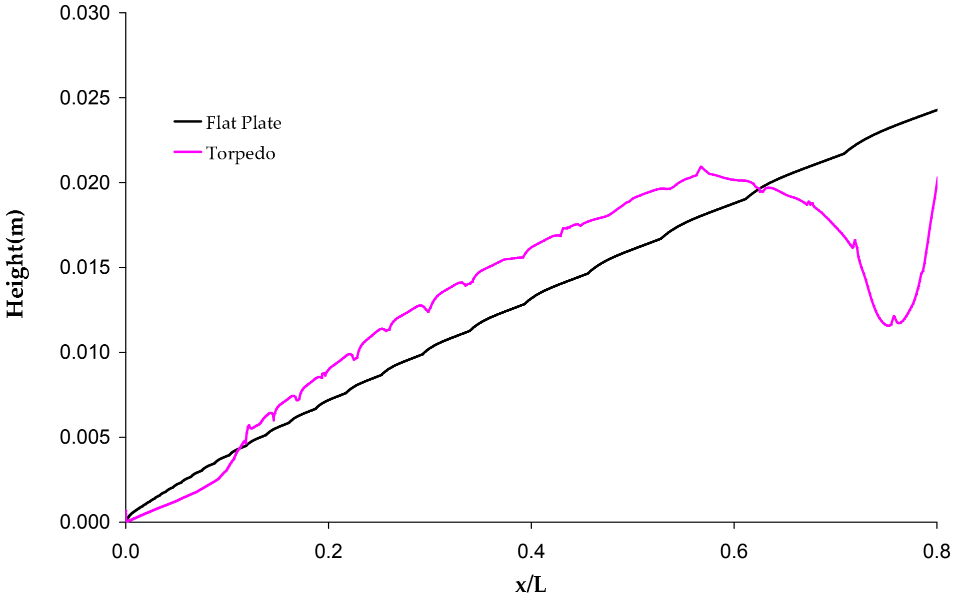

Figure 5.47. A comparison for the boundary layer thicknesses of a flat plate and the torpedo for the same initial conditions

proximate the Newtonian values with good agreement. The numerical result for C_f is 0.0023965 and there is only a 5.22% difference between the numerical and theoretical values so this makes reasonable that the interval chosen can be treated as a flat plate.

According to the MDR case the new drag force should be 4.085 times smaller. Therefore, the reduced friction drag in the polymer induced region can be assumed as 228.7 N, where the original friction drag was 934.03 N at that region.

In this situation, the total drag was decreased to a value of 588 N from 1293.334 N. However, the thrust force still remains the same Therefore, a new top speed was set to the model where the thrust force is equal to the reduced drag at that condition. In order to this an initial guess was performed using the definition of drag coefficient.

In new condition the C_D value is 0.03685. From the definition of the C_D the top speed was evaluated as 29.66 m/s. However, at that speed the reduction of friction is even less. So a few iterations of numerical computations are required. After some steps of computations the maximum velocity was found to be 31.98 m/s.

6. CONCLUSIONS

In this study, modeling of a torpedo was accomplished through the use of Fluent CFD software. The torpedo model was based on an existing model but only the dimensions and some other specifications were referenced. Briefly, the design built was an original geometry with the shaft and propeller effects included. Axisymmetric steady state equations were used since the torpedo is a body of revolution.

The design was performed to find a realistic model in order to evaluate the frictional forces and their share in the total drag on a torpedo body. It was realized that the pressure forces are lower compared to frictional forces. This is since the torpedo resembles a flat plate more than a cylinder. The body was so streamlined that separation existed at the 0.999 of the body length of the torpedo.

The frictional forces are overwhelmingly dominant on a torpedo body. Since the body shape is restricted with other design considerations the reduction of the friction drag is an alternative method. For percentages of friction drag reduction between 10% and 80%, maximum speed values were found and effect of reduction of friction drag was shown in a more explicit figure.

Finally, the speed of the torpedoes can be increased through different methods of drag reduction. However, for a sensible magnitude of maximum velocity, at least 40% - 50% of friction drag reduction should be provided. This thesis will be helpful to study drag reduction in torpedoes or other axisymmetric bodies. The design steps and criteria can be applied for most of the vehicles.

6.1. Suggestions for Further Study

The model created in the study can be a good source material for further studies. It can be used in both friction drag reduction and body shaping studies. Since it is a military application the design needs more qualified data. The initial steps of an original torpedo design can be reached with the cooperation of the navy. However, this study can be helpful only in hydrodynamic design of the torpedo.

Besides, in this design a 3D model lacks, since a 3D model with approximately same resolution with the 2D model will include more than 3 million cells. In addition, the 3D solver spends much more time even if there are equal numbers of elements in two meshes of 2D and 3D. Therefore, a 3D design could not be achieved because of the time restrictions but should be studied to see the effects of angle of attack. In 2D plane geometry angle of attack can be provided by assigning an inlet velocity composed of non-zero x and y components. However, in axisymmetric model this is not possible. The 3D model can be tested for only the final stage of the design since it requires much more time.

The application of friction drag reduction methods can be performed using this study since the distribution of the frictional forces and the expectations for a certain level of friction drag reduction was determined in the study. There is an also approximate theoretical solution of polymer induced drag reduction. It is at a significant level which can be achieved by using a very high molecular weight polymer dissolved in water with enough magnitudes of concentration. The polymer can be injected a little far from the nose at the surface of the cylinder of the torpedo where the pressure is lower. The polymer should also be non-ionic to prevent the degradation. Besides, there is no need to inject polymer to the afterbody part because it can not respond efficiently.

As a last remark, the model can be used to examine mixing properties of the drag reducers. This will also help the improvement of the injection of drag reducers and will provide a better design of friction drag reduction .

APPENDIX A: DISCRETIZATION IN FLUENT

Fluent uses a control-volume based solution technique to convert the governing equations to algebraic equations. This control volume technique consists of integrating the governing equations about each control volume, yielding discrete equations that conserve each quantity on a control-volume basis as explained in section CFD. Below, the discretization of the governing equations for the steady-state conservation equation for transport of a scalar quantity is shown. The Equation A.1 is written in integral form for an arbitrary control volume as follows:

$$\oint \rho\phi\vec{v}.d\vec{A} = \oint \Gamma_\phi \nabla_\phi .d\vec{A} + \int_V S_\phi dV \tag{A.1}$$

where ρ is density, $\vec{v}$ is velocity vector, $\vec{A}$ is surface area vector, Γ_ϕ is diffusion coefficient for ϕ, ∇_ϕ is gradient of ϕ and S_ϕ is source of ϕ per unit volume. Equation A.1 is applied to each cell in the computational domain. The two-dimensional triangular cell shown in Figure A.1 is an example of such a control volume. Discretization of Equation A.1 on that cell yields

$$\sum_f^{Nfaces} \rho_f v_f \phi_f .\vec{A}_f = \sum_f^{Nfaces} \Gamma_\phi (\nabla_\phi)_n .\vec{A}_f + S_\phi V \tag{A.2}$$

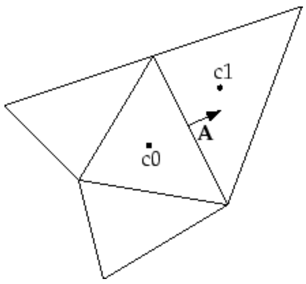

Figure A.1. Control volume used to illustrate discretization of a scalar transport equation [20]

Fluent stores discrete values of the scalar at the cell centers. However, face values are required for the convection terms in Equation A.1 and must be interpolated from the cell center values. This is accomplished using an upwind scheme [7] . When second-order accuracy is desired, second order upwind scheme is used where higher-order accuracy is achieved at cell faces through a Taylor series expansion of the cell-centered solution about the cell centroid. The face value ϕ_f is computed using the following expression

$$\phi_f = \phi + \nabla_\phi . \Delta\vec{s} \tag{A.3a}$$

$$\nabla_\phi = \frac{1}{V} \sum_{f}^{Nfaces} \tilde{\phi_f} \vec{A} \tag{A.3b}$$

where ϕ and ∇_ϕ are the cell-centered value and its gradient in the upstream cell respectively. $\Delta\vec{s}$ is the displacement vector from the upstream cell centroid to the face centroid. ∇_ϕ is calculated using the Equation A.3b with the face values $\tilde{\phi_f}$ estimated by averaging ϕ from the two cells adjacent to the face.

It is necessary to control the change of ϕ, because the equation set Fluent solves, is nonlinear. This is typically achieved by under-relaxation, which reduces the change of ϕ produced during each iteration. The new value of the variable ϕ within a cell depends on the old value, ϕ_{old}, the computed change in ϕ, $\Delta\phi$, and the under-relaxation factor, α [8] .

$$\phi = \phi_{old} + \alpha\Delta\phi \tag{A.4}$$

---

[7] Fluent allows you to choose from several upwind schemes: first-order upwind, second-order upwind, power law, central-differencing and quick. The second-order upwind scheme is explained since in this study only second-order upwind scheme was used.

[8] The under relaxation factors have default values in Fluent. These can be lowered, considering the instabilities that might occur, in order to decrease the computation time and to obtain faster convergence.

A.1. Pressure Velocity Coupling

The integration of the steady state continuity equation ($\oint \rho\vec{v}.d\vec{A} = 0$) over the control volume in Figure A.1, yields the following discrete equation

$$\sum_{f}^{Nfaces} J_f A_f = 0 \tag{A.5a}$$

$$J_f = \hat{J}_f + d_f(p_{c0} - p_{c1}) \tag{A.5b}$$

where J_f is the mass flux through face f (ρv_n). In addition p_{c0} and p_{c1} are the pressures within the two cells on either side of the face and $\hat{J}_f$ contains the influence of velocities in these cells.

For the segregated solver, the solver used in the study, the momentum and continuity equations are solved sequentially as mentioned. The continuity equation is used as an equation for pressure to do this. However, pressure is not seen explicitly in Equation A.5a for incompressible fluids, because density is not directly related to pressure. A coupling is done between pressure and velocity by using Equation A.5b to derive an equation for pressure from the discrete continuity equation (Equation A.5a). [9]

The SIMPLE (Semi-Implicit Method for Pressure-Linked Equations) family of algorithms [24] is used for introducing pressure into the continuity equation through the use of Equation A.5b. It relates pressure and velocity corrections to enforce mass conservation and to obtain the pressure field. Assuming a pressure field p^*, J_f^* is computed from Equation A.5b.

$$J_f^* = \hat{J}_f^* + d_f(p_{c0}^* - p_{c1}^*) \tag{A.6}$$

However, the Equation A.6 does not satisfy the continuity equation. $J_f^{'}$ is added as a

---

[9] Fluent provides the option to choose among three pressure-velocity coupling algorithms: SIMPLE, SIMPLEC, and PISO.

correction to the face flux J_f^* to yield the corrected face flux,J_f , which

$$J_f = J_f^* + J_f^{'} \tag{A.7}$$

satisfies the continuity equation. In SIMPLE algorithm $J_f^{'}$ can be written as

$$J_f^{'} = d_f(p_{c0}^{'} - p_{c1}^{'}) \tag{A.8}$$

where $p^{'}$ is the cell pressure correction.

The flux correction equations are substituted into the discrete continuity equation (Equation A.5a) to obtain a discrete equation for the pressure correction $p^{'}$ in the cell.

$$a_p p^{'} = \sum_{nb} a_{nb} p_{nb}^{'} + b \tag{A.9}$$

where b is the source term for the net flow rate into the cell.

$$b = \sum_{f}^{Nfaces} J_f^* A_f = 0 \tag{A.10}$$

The pressure-correction equation (Equation A.9) may be solved using the algebraic multigrid method. After finding a solution, the cell pressure and the face flux are corrected using

$$\begin{aligned} p =& p^* + \alpha_p p^{'} && \text{(A.11)} \\ J_f^* =& J_f^* + d_f(p_{c0}^* - p_{c1}^*) && \text{(A.12)} \end{aligned}$$

The α_p is the under-relaxation factor for pressure. It has a default value of 0.3 in Fluent. It can be lowered in order to decrease computation time.

APPENDIX B: TURBULENCE MODELING IN FLUENT

The most important characteristic of the turbulent flow is the fluctuating velocity fields. These fluctuations mix transported quantities such as momentum, energy, and species concentration and cause the transported quantities to fluctuate as well. Since these fluctuations can be of small scale and high frequency, they are computationally too expensive to simulate directly in practical engineering cases. Instead of this the governing equations can be time-averaged, ensemble-averaged or changed to remove the small scales so that the modified set of equations are computationally less expensive. These modified equations will contain additional unknown variables and they have to be determined in terms of known quantities [20].

In fluid mechanics no single turbulence model is accepted universally superior for all types of problems. The flow in a pipe, the flow through a turbine or an impeller, an external flow over an airfoil or a hydrofoil can not be simulated with one single model so there are different turbulence models to simulate different cases. [20].

Fluent provides the following turbulence models:

- Spalart-Allmaras model
- k-ϵ models
    - Standard k-ϵ model
    - Renormalization-group (RNG) model
    - Realizable k-ϵ model
- k-w models
    - Standard k-w model
    - Shear-stress Transport (SST) k-w model
- v^2-f model
- Reynolds stress model (RSM)
- Large eddy simulation (LES) model

The standard k-ϵ model requires more computational effort than the Spalart-Allmaras model since an additional transport equation is solved. The realizable k-ϵ model requires little more computational effort than the standard k-ϵ model. Because of the extra terms and functions in the governing equations and a greater degree of non-linearity, the RNG k-ϵ model takes 10-15% more CPU time than with the standard k-ϵ model. Like the k-ϵ models, the k-w models are also two-equation models, and require about the same computational effort.

The RSM requires additional memory and CPU time because of the increased number of the transport equations for Reynolds stresses. Usually the RSM in Fluent requires 50-60% more CPU time per iteration compared to the k-ϵ and k-w models. Moreover, 15-20% more memory is needed.

B.1. Reynolds (Ensemble) Averaging

In Reynolds averaging the variables of the Navier-Stokes equations are decomposed into a fluctuating and a mean part. The velocity is decomposed into a mean $\bar{u}_i$ and a fluctuating part u_i' (where i = 1,2,3) as follows:

$$u_i = \bar{u}_i + u_i' \tag{B.1}$$

For other scalar quantities the same procedure is applied, as in Equation B.2, where ϕ denotes a scalar such as pressure or energy

$$\phi = \bar{\phi} + \phi' \tag{B.2}$$

Converting the flow variables in instantaneous continuity and momentum equations into this form and taking a time average (yields the drop of overbar on the mean velocity, $\bar{u}_i$) gives the ensemble-averaged momentum equations. They are written in

Cartesian tensor form as

$$\frac{\partial \rho}{\partial t} + \frac{\partial}{\partial x_i}(\rho u_i) = 0 \tag{B.3}$$

$$\frac{\partial}{\partial t}(\rho u_i) + \frac{\partial}{\partial x_j}(\rho u_i u_j) = -\frac{\partial p}{\partial x_i} + \frac{\partial}{\partial x_j}\left[\mu\left(\frac{\partial u_i}{\partial x_j} + \frac{\partial u_j}{\partial x_i} - \frac{2}{3}\delta_{ij}\frac{\partial u_i}{\partial x_i}\right)\right] + \frac{\partial}{\partial x_j}(-\rho\overline{u'_i u'_j}) \tag{B.4}$$

The equations Equation B.3 and Equation B.4 are called Reynolds-averaged Navier-Stokes (RANS) equations. However, the additional terms appear in Equation B.4 which represent the effect of turbulence. The Reynolds stresses $-\rho\overline{u'_i u'_j}$ should be modeled in order to model turbulence. The Reynolds stresses are related to the mean velocity gradients using the Boussinesq hypothesis [25].

$$-\rho\overline{u'_i u'_j} = \mu_t\left(\frac{\partial u_i}{\partial x_j} + \frac{\partial u_j}{\partial x_i}\right) - \frac{2}{3}\left(\rho k + \mu\frac{\partial u_i}{\partial x_i}\right)\delta_{ij} \tag{B.5}$$

In Spalart-Allmaras model, $k-\epsilon$ models and the k-w models, the Boussinesq hypothesis is used. It needs low computational effort associated with the computation of the turbulent viscosity which makes it favorable. In the case of the $k-\epsilon$ and k-w models, two additional transport equations (for the turbulence kinetic energy, k, and either the turbulence dissipation rate, ϵ or the specific dissipation rate,w) are solved, and μ_t is computed as a function of k and ϵ. The Boussinesq hypothesis assumes μ_t as an isotropic scalar quantity which is not strictly true and a disadvantage for the hypothesis

.

B.2. The k-$\boldsymbol{\epsilon}$ Model

Since it was proposed by Launder and Spalding [26] k-ϵ is very popular in flow simulations especially the standard k-ϵ model with two separate transport equations. Its reasonable accuracy, robustness and economy makes it favorable in engineering community. Besides, it is used in a wide range of applications and it is a general and common model for almost all types of incompressible flows from turbomachinery to pipe flows, external flows and boundary layer flows.

B.2.1. The Standard k-$\boldsymbol{\epsilon}$ Model

The standard k-ϵ model is a semi-empirical model. It is based on model transport equations for the turbulence kinetic energy k and its dissipation rate ϵ. It was assumed in the derivation of the k-ϵ model that the flow is fully turbulent, and the effects of molecular viscosity were negligible. This makes the standard k-ϵ model valid for only fully turbulent flows. The turbulence kinetic energy, k, and its rate of dissipation, ϵ, are obtained from the following transport equations:

$$\frac{\partial}{\partial t}(\rho k) + \frac{\partial}{\partial x_i}(\rho k u_i) = \frac{\partial}{\partial x_j}\left[\left(\mu + \frac{\mu_t}{\sigma_k}\right)\frac{\partial k}{\partial x_j}\right] + G_k + G_b - \rho\epsilon - Y_M + S_k \tag{B.6}$$

$$\frac{\partial}{\partial t}(\rho \epsilon) + \frac{\partial}{\partial x_i}(\rho \epsilon u_i) = \frac{\partial}{\partial x_j}\left[\left(\mu + \frac{\mu_t}{\sigma_\epsilon}\right)\frac{\partial \epsilon}{\partial x_j}\right] + C_{1\epsilon}\frac{\epsilon}{k}(G_k + C_{3\epsilon}G_b) - C_{2\epsilon\rho}\frac{\epsilon^2}{k} + S_\epsilon \tag{B.7}$$

The term G_k is called the production of turbulence kinetic energy and is modeled for the standard, RNG, and realizable k-ϵmodels as seen in Equation B.8. Equation B.9 also defines G_k in a manner consistent with Boussinesq hypothesis where $S \equiv \sqrt{2S_{ij}S_{ij}}$. Y_M is the contribution of the fluctuating dilatation in compressible turbulence to the overall dissipation rate.

$$G_k = -\rho \overline{u_i' u_j'} \frac{\partial u_j}{\partial x_i} \tag{B.8}$$

$$G_k = \mu_t S^2 \tag{B.9}$$

The term G_b represents the generation of turbulence kinetic energy due to buoyancy. It exists when the gravity field and the temperature gradient are non-zero and is given by

$$G_b = \beta g_i \frac{\mu_t}{Pr_t} \frac{\partial T}{\partial x_i} \tag{B.10}$$

where Pr_t is the turbulent Prandtl number for energy with a default value of 0.85, g_i is the component of the gravitational vector in the **i**th direction and β is the coefficient of thermal expansion.

The turbulent viscosity or sometimes called eddy viscosity μ_t is computed by combining k and ϵ as follows:

$$\mu_t = \rho C_\mu \frac{k^2}{\epsilon} \tag{B.11}$$

The model constants in equations B.6 and B.7 have the default following values [26]: $C_{1\epsilon} = 1.44$, $C_{2\epsilon} = 1.92$, $C_\mu = 0.09$, $\sigma_k = 1.0$, $\sigma_\epsilon = 1.3$. These values have been determined from experiments with air and water. They work well for a wide range of wall-bounded and free shear flows [20].

B.2.2. The Realizable k-ϵ Model

Since the model satisfies certain mathematical constraints on the Reynolds stresses it is called realizable k-ϵ model. Neither the standard k-ϵ model nor the RNG k-ϵ model is realizable. It provides superior performance for flows involving rotation, boundary layers under strong adverse pressure gradients, separation, and recirculation. The Realizable k-ϵ model differs from the standard k-ϵ model in two points. First, it has a new formulation for the turbulent viscosity. Besides, a new transport equation for the dissipation rate, ϵ, has been derived from an exact equation for the transport of the mean-square vorticity fluctuation [20].

The combination of the Boussinesq relationship (Equation B.5) and the eddy viscosity definition (Equation B.11) gives the following expression for the normal Reynolds stress in an incompressible strained mean flow

$$\overline{u^2} = \frac{2}{3}k - 2\nu_t \frac{\partial U}{\partial x} \tag{B.12}$$

With the use of Equation B.11 for $\nu_t \equiv \mu_t/\rho$ it is seen that the normal stress, $\overline{u^2}$, becomes negative, which should be positive by definition and now non-realizable, when the strain is large enough to satisfy the relationship

$$\frac{k}{\epsilon}\frac{\partial U}{\partial x} > \frac{1}{3C_\mu} \approx 3.7 \tag{B.13}$$

The Schwarz inequality for shear stresses ($\overline{u_\alpha u_\beta}^2 \leq \overline{u_\alpha^2 u_\beta^2}$) can be violated when the mean strain rate is large. The best way to ensure the realizability (positivity of normal stresses and Schwarz inequality for shear stresses) is to make C_μ by sensitizing it to the mean flow and the turbulence. The notion of variable C_μ is suggested by many modelers including Reynolds [28], and is well supported with experimental results.

The realizable k-ϵ model proposed by Shih et al. [27] was intended to address these deficiencies of traditional k-ϵ models by adopting a new eddy-viscosity formula involving a variable C_μ originally proposed by Reynolds [28] and a new model equation for dissipation (ϵ) based on the dynamic equation of the mean-square vorticity fluctuation.

The modeled transport equations for k and ϵ in the realizable k-ϵmodel are:

$$\frac{\partial}{\partial t}(\rho k) + \frac{\partial}{\partial x_i}(\rho k u_j) = \frac{\partial}{\partial x_i}\left[\left(\mu + \frac{\mu_t}{\sigma_k}\right)\frac{\partial k}{\partial x_j}\right] + G_k + G_b - \rho\epsilon - Y_M + S_k \tag{B.14}$$

$$\frac{\partial}{\partial t}(\rho \epsilon) + \frac{\partial}{\partial x_j}(\rho \epsilon u_j) = \frac{\partial}{\partial x_j}\left[\left(\mu + \frac{\mu_t}{\sigma_\epsilon}\right)\frac{\partial \epsilon}{\partial x_j}\right] + \rho C_1 S_\epsilon - \rho C_2 \frac{\epsilon^2}{k + \sqrt{\nu\epsilon}} + C_{1\epsilon}\frac{\epsilon}{k}C_{3\epsilon}G_b + S_\epsilon \tag{B.15}$$

$$C_1 = max\left[0.43, \frac{\eta}{\eta + 5}\right], \quad \eta = S\frac{k}{\epsilon} \tag{B.16}$$

G_k, G_b, μ_t and Y_M are same with the k-ϵ standard model. S_k and S_ϵ are user defined source terms.

The difference between the realizable k-ϵmodel is that C_μ is not constant. It is computed from

$$C_\mu = \frac{1}{A_0 + A_s \frac{kU^*}{\epsilon}} \tag{B.17}$$

where

$$U^* \equiv \sqrt{S_{ij}S_{ij}} + \tilde{\Omega}_{ij}\tilde{\Omega}_{ij} \tag{B.18}$$

and

$$\begin{aligned}
\tilde{\Omega}_{ij} &= \Omega_{ij} - 2\epsilon_{ijk}\omega_k \\
\Omega_{ij} &= \overline{\Omega_{ij}} - \epsilon_{ijk}\omega_k
\end{aligned}$$

where $\overline{\Omega_{ij}}$ is the mean rate-of-rotation tensor viewed in a rotating reference frame with the angular velocity w_k. The model constants A_s and A_0 are given by;

$$A_0 = 4.04, A_s = \sqrt{6}\cos\phi \tag{B.19}$$

and

$$\phi = \frac{1}{3}\cos^{-1}(\sqrt{6}W,\ W = \frac{S_{ij}S_{jk}S_{ki}}{\tilde{S}},\ \tilde{S} = \sqrt{S_{ij}S_{ij}},\ S_{ij} = \frac{1}{2}\left(\frac{\partial u_j}{\partial x_i} + \frac{\partial u_i}{\partial x_j}\right)$$
$$C_{1\epsilon} = 1.44,\ C_2 = 1.9,\ \sigma_k = 1.0,\ \sigma_\epsilon = 1.2$$

B.3. Wall Treatment

B.3.1. Standard Wall Functions

One of the most widely used method of wall treatment for industrial flows is standard wall functions which are based on the proposal of Launder and Spalding. Standard wall functions work reasonably well for a wide range of wall bounded flows, but if the flow begins to diverge from ideal conditions (i.e. strong adverse pressure gradients) the accuracy of their predictions begin to degrade [20].

The law of the wall for mean velocity gives

$$U^* = \frac{1}{\kappa}\ln(Ey^*) \tag{B.20}$$

where

$$U^* \equiv \frac{U_p C_\mu^{0.25} k_p^{0.5}}{\tau_w/\rho} \tag{B.21}$$

$$y^* \equiv \frac{\rho C_\mu^{0.25} k_p^{0.5} y}{\mu} \tag{B.22}$$

B.3.2. Non-Equilibrium Wall Functions

The non-equilibrium wall function is two layer based and sensitized to the pressure gradient effects. In order to compute the budget of turbulence kinetic energy in wall neighboring cells the two layer based concept is adopted. Briefly, the non-equilibrium wall functions extend the applicability of the wall function approach by including the effects of pressure gradient and strong non-equilibrium.

The log-law for mean velocity sensitized to pressure gradients is

$$\frac{\tilde{U} C_\mu^{0.25} k^{0.5}}{\tau_w/\rho} = \frac{1}{\kappa} \ln\left(E \frac{\rho C_\mu^{0.25} k^{0.5} y}{\mu}\right) \tag{B.23}$$

where

$$\tilde{U} = U - \frac{1}{2}\frac{dp}{dx}\left[\frac{y_v}{\rho\kappa\sqrt{k}} \ln\left(\frac{y}{y_v}\right) + \frac{y - y_v}{\rho\kappa\sqrt{k}} + \frac{Y_v^2}{\mu}\right] \tag{B.24}$$

$$y_v \equiv \frac{\mu y_v^*}{\rho C_\mu^{0.25} k_p^{0.5}}$$

where y_v is the physical sublayer thickness and $y_v^* = 11.225$.

B.3.3. Enhanced Wall Treatment

As the third and last option of near-wall modeling methods in Fluent enhanced wall treatment combines a two-layer model with enhanced wall functions. When the near-wall mesh is fine enough to be able to resolve the laminar sublayer or in other words $y^+ = 1$, the enhanced wall treatment will be identical to the traditional two-layer zonal model. In order to apply the model the viscosity-affected near-wall region should be completely resolved all the way to the viscous sublayer.

The two-layer approach is an integral part of the enhanced wall treatment and is used to specify both and the turbulent viscosity in the near-wall cells. Achieving this is done by division of the whole domain into a viscosity-affected region and a fully-turbulent region. The borderline of the two regions is determined by a wall-distance-based Re number which is given as

$$Re_y \equiv \frac{\rho y \sqrt{k}}{\mu} \tag{B.25}$$

When the enhanced wall treatment method is used Fluent changes the way of estimation of turbulent viscosity and length scale according to the two layer model.Detailed explanation can be found in literature [20].

REFERENCES

1. Jin-jun, W., L. Shi-long, C. Guang, “Experimental Study on the Turbulent Boundary Layer Flow over Riblets Surface”, *Fluid Dynamics Research*, Vol. 27, pp. 217-229, 2000.

2. *Mathematics Encyclopedia and Lessons*, http://www.mathdaily.com, 2005.

3. *U.S. Navy Office of Information*, http://www.chinfo.navy.mil/navpalib/factfile/ weapons/wep-torp.html, 2005.

4. *The Freeper Foxhole Studies: The Early History of Torpedoes*, http://freerepublic.com/focus/f-vetscor/1044346/posts, 2005.

5. Alyanak, E., V. Venkayya, R. Grandhi and R. Penmetsa, “Structural Response and Optimization of a Supercavitating Torpedo”, *Finite Elements in Analysis and Design*, Vol. 41, pp. 563-582, 2005.

6. Osse, J., *Low Drag Technology Applied to Human Powered Vehicles*, Applied Physics Laboratory, University of Washington.

7. Kanikdale T. S., *Optimization of Airship Envelope Shape Using Computational Fluid Dynamics*, M.S. Thesis, Department of Aerospace Engineering, Indian Institute of Technology, 2004.

8. Toms, B. A., “On the Early Experiments on Drag Reduction by Polymers”, *Physics of Fluids*, Vol. 20, pp. 3-5, 1977.

9. Mysels, K. J., *Flow of Thickened Fluids*, U.S. Patent no. 2492173, 1949.

10. Sinnarwalla, A. M. and T. R. Sundaram, “Lift and Drag Effects Due to Polymer Injections on a Symmetric Hydrofoil”, *Journal of Hydronautics*, Vol. 12, pp. 71-77, 1978.

11. Truong, V. T., *Drag Reduction Technologies*, Maritime Platforms Division Aeronautical and Maritime Research Laboratory.

12. Martin, J. R., B. D. Shapella, “The Effect of Solvent Solubility Parameter on Turbulent Flow Drag Reduction in Polyisobutylene Solutions”, *Experiments in Fluids*, Vol. 34, pp. 535-539, 2003.

13. Bechert, D. W., M. Bruse, W. Hage, and R.Meyer, “Fluid Mechanics of Biological Surfaces and Their Technological Application”, *Naturwissenschaften*, Vol. 87, pp. 157-171, 2000.

14. Bertin, J. J., *Aerodynamics for Engineers 4th edt.*, Prentice-Hall, 2001.

15. Munson, B. R., D. F. Young, T. H. Okiishi, *Fundamentals of Fluid Mechanics 3rd edt.*, John Wiley, 1998.

16. Sumer, B. M., J. Fredsoe, *Hydrodynamics around Cylindrical Structures*, World Scientific Publishing, 1997.

17. Versteeg, H. K., W. Malalasekera, *An Introduction to Computational Fluid Dynamics: the Finite Volume Method* , Longman, 1995.

18. Virk, P. S., “Drag Reduction Fundamentals”, *AIChe Journal*, Vol. 21, pp. 625-655, 1975.

19. Larson, R. G., “Analysis of Polymer Turbulent Drag Reduction in Flow Past a Flat Plate”, *J.Non-Newtonian Fluid Mech.*, Vol. 111, pp. 229-250, 2003.

20. Documentation of Fluent 6.1.22 CFD Software, 2005.

21. Bourgoyne, D. A., C. Q. Judge, J. M. Hamel, S. L. Ceccio, D. R. Dowling, *Lifting Surface Flow, Pressure and Vibration at High Reynolds-Number*, Department of Mechanical Engineering, University of Michigan, 2004.

22. Mulvany, N. J., J. Y. Tu, L. Chen and B. Anderson, “Assessment of Two-Equation Turbulence Modeling for High Reynolds Number Hydrofoil Flows”, *International Journal for Numerical Methods in Fluids*, Vol. 45, pp. 275-299, 2004.

23. Patel, V. C., A. Nakayama and R.Damian, *An Experimental Study of the Thick Turbulent Boundary Layer Near the Tail of a Body of Revolution*, Iowa Institute of Hydraulic Research, The University of Iowa, 1973.

24. Patankar, S. V., *Numerical Heat Transfer and Fluid Flow*, Hemisphere, Washington D.C., 1980.

25. Hinze, J. O., *Turbulence*, McGraw-Hill Publishing Co., New York, 1975.

26. Launder, B. E. and D. B. Spalding, *Lectures in Mathematical Models of Turbulence*, Academic Press, London, 1972.

27. Shih T. H., W. W. Liou, A. Shabbir, Z. Yang, and J. Zhu. “A New Eddy-viscosity Model for High Reynolds Number Turbulent Flows Model Development and Validation”, *Computers and Fluids*, Vol. 24, pp. 227-238, 1995.

28. Reynolds, W. C., *Fundamentals of Turbulence for Turbulence Modeling and Simulation*, Lecture Notes for Von Karman Institute Agard, Report No. 755, 1987.